A Time-Dependent Spectral Point Spread Function for the OSIRIS Optical Spectrograph

A Thesis Submitted to the
College of Graduate Studies and Research
in Partial Fulfillment of the Requirements
for the degree of Master of Science
in the Department of Physics and Engineering Physics
University of Saskatchewan
Saskatoon

By
Thomas L. Thalheimer

Permission to Use

In presenting this thesis in partial fulfilment of the requirements for a Postgraduate degree from the University of Saskatchewan, I agree that the Libraries of this University may make it freely available for inspection. I further agree that permission for copying of this thesis in any manner, in whole or in part, for scholarly purposes may be granted by the professor or professors who supervised my thesis work or, in their absence, by the Head of the Department or the Dean of the College in which my thesis work was done. It is understood that any copying or publication or use of this thesis or parts thereof for financial gain shall not be allowed without my written permission. It is also understood that due recognition shall be given to me and to the University of Saskatchewan in any scholarly use which may be made of any material in my thesis.

Requests for permission to copy or to make other use of material in this thesis in whole or part should be addressed to:

Head of the Department of Physics and Engineering Physics
116 Science Place
University of Saskatchewan
Saskatoon, Saskatchewan
Canada
S7N 5E2

Abstract

The primary goal of the recently formed Absorption Cross Sections of Ozone (ACSO) Commission is to establish an international standard for the ozone cross section used in the retrieval of atmospheric ozone number density profiles. The Canadian instrument OSIRIS onboard the Swedish spacecraft Odin has produced high quality ozone profiles since 2002, and as such the OSIRIS research team has been asked to contribute to the ACSO Commission by evaluating the impact of implementing different ozone cross sections into SASKTRAN, the radiative transfer model used in the retrieval of OSIRIS ozone profiles. Preliminary analysis revealed that the current state of the OSIRIS spectral point spread function, an array of values describing the dispersion of light within OSIRIS, would make such an evaluation difficult. Specifically, the current spectral point spread function is time-independent and therefore unable to account for any changes in the optics introduced by changes in the operational environment of the instrument. Such a situation introduces systematic errors when modelling the atmosphere as seen by OSIRIS, errors that impact the quality of the ozone number density profiles retrieved from OSIRIS measurements and make it difficult to accurately evaluate the impact of using different ozone cross sections within the SASKTRAN model.

To eliminate these errors a method is developed to calculate, for the 310-350 nm wavelength range, a unique spectral point spread function for every scan in the OSIRIS mission history, the end result of which is a time-dependent spectral point spread function. The development of a modelling equation is then presented, which allows for any noise present in the time-dependent spectral point spread function to be reduced and relates the spectral point spread function to measured satellite parameters. Implementing this modelled time-dependent spectral point spread function into OSIRIS ozone retrieval algorithms is shown to improve all OSIRIS ozone profiles by 1-2% for tangent altitudes of 35–48 km. Analysis is also presented that reveals a previously unaccounted for temperature-dependent altitude shift in OSIRIS measurements. In conjunction with the use of the time-dependent spectral point spread function, accounting for this altitude shift is shown to result in an almost complete elimination of the temperature-induced systematic errors seen in OSIRIS ozone profiles. Such

improvements lead to improved ozone number density profiles for all times of the OSIRIS mission and make it possible to evaluate the use of different ozone cross sections as requested by the ACSO Commission.

Acknowledgements

This work was financially supported by the Canadian Space Agency and the National Sciences and Engineering Research Council, along with the University of Saskatchewan and Institute of Space and Atmospheric Studies. Personally, I would like to sincerely thank my supervisor Dr. Doug Degenstein. Throughout the entirety of this work he was a constant source of knowledge, inspiration, and encouragement, helping me to grow as both a professional and an individual. I would also like to express my gratitude to Drs. Adam Bourassa and Nick Lloyd, who were always more than willing to share their expertise. Finally, I would like to thank my family and friends, who always supported me in any way they could. Without them none of this would have been possible.

To Cherise

My light in dark places, when all other lights go out.

Contents

List of Tables

List of Figures

List of Abbreviations

ACE	Atmospheric Chemistry Experiment
ACSO	Absorption Cross Sections of Ozone
CCD	Charge-Coupled Device
DBM	Daumont, Brion, and Malicet
FOP	Field-flattener/Order sorter/Prism
FWHM	Full Width at Half Maximum
IRI	Infrared Imaging Component of OSIRIS
MART	Multiplicative Algebraic Reconstruction Technique
NP	North Pole
OS	Optical Spectrograph Component of OSIRIS
OSIRIS	Optical Spectrograph and Infrared Imaging System
PSF	Point Spread Function
SAGE	Stratospheric Aerosol and Gas Experiment
SaskMART	University of Saskatchewan Multiplicative Algebraic Reconstruction Technique
SASKTRAN	University of Saskatchewan Radiative Transfer Model
SBUV	Solar Backscatter Ultraviolet
SCIAMACHY	Scanning Imaging Absorption Spectrometer for Atmospheric Chartography
SMR	Sub-Millimetre Radiometer
SP	South Pole
TOA	Top-of-Atmosphere
WMO	World Meteorological Organization

Chapter 1

Introduction

The Optical Spectrograph and Infrared Imaging System (OSIRIS) is a Canadian designed and constructed instrument currently orbiting Earth onboard the Swedish satellite Odin. The focus of this thesis is on the development of a time-dependent spectral point spread function for the 310–350 nm wavelength range of the OSIRIS optical spectrograph in order to minimize systematic errors that have been identified in atmospheric ozone profiles retrieved from OSIRIS measurements. Such a development is accomplished by convolving a high resolution solar spectrum with Gaussian curves representative of the OSIRIS spectral point spread function and comparing the resulting convolved spectra against OSIRIS measurements for selected wavelength ranges. The Gaussian curve associated with the best-fitting convolved solar spectrum in each wavelength range is taken as the point spread function for that range and time. A modelled version of this calculated time-dependent spectral point spread function is then created in order to reduce noise and relate the spectral point spread function to measured satellite parameters. Finally, analysis is undertaken which verifies that the use of this modelled spectral point spread function reduces the systematic errors present in OSIRIS ozone profiles to negligible levels.

Chapter 2 discusses OSIRIS and its optical spectrograph in great detail, and also introduces the calculations needed to retrieve vertical number density profiles of atmospheric ozone from its measurements. Specifically, an overview of the SASKTRAN radiative transfer model, which is used to create a fully spherical model of the atmosphere, is given, along with a discussion of how SASKTRAN is used alongside OSIRIS measurements within the SaskMART iterative retrieval technique to produce ozone number density profiles. Also introduced in Chapter 2 is the ozone cross section, which describes the probability of an incident photon being absorbed by an ozone molecule as a function of wavelength. Recently,

an international group of ozone experts established the Absorption Cross Sections of Ozone (ACSO) Commission in an effort to standardize the ozone cross section used by atmospheric researchers around the world. As part of this Commission, the OSIRIS team must evaluate the impact of using different ozone cross sections within the SASKTRAN model.

The focus of Chapter 3 is on the OSIRIS spectral point spread function, a set of values which describe the final dispersion of light observed by the OSIRIS spectrograph as a function of wavelength. The current version of the spectral point spread function used when modelling the atmosphere as seen by OSIRIS is time-independent, a situation that may introduce systematic errors into the modelled spectrum when the final dispersion pattern of light recorded by OSIRIS is altered due to temperature changes within the instrument. These systematic errors reduce the quality of the modelled OSIRIS spectrum and also make it difficult to evaluate the impact of using different cross sections within the SASKTRAN model. In order to eliminate these systematic errors a method for calculating a time-dependent spectral point spread function is developed as part of this thesis work. The final method only calculates a time-dependent spectral point spread function for the 310–350 nm wavelength range, but this wavelength range is shown to be sufficient to eliminate nearly all systematic errors introduced when retrieving vertical profiles of ozone.

Chapter 4 thoroughly presents the process of modelling the time-dependent spectral point spread function with an equation that uses measured satellite parameters as variables. The reason for this work is two-fold. Firstly, relating the time-dependent spectral point spread function to measured satellite parameters provides an excellent verification that the values of the spectral point spread function are valid. Secondly, there is a noticeable level of noise in the calculated time-dependent spectral point spread function. A model effectively acts as a smoothing tool to reduce this noise. The Chapter concludes with the presentation of a model which successfully relates the time-dependent spectral point spread function to the OSIRIS optics temperature and satellite track angle.

The results of implementing this modelled time-dependent spectral point spread function into the algorithms used to model the atmosphere as seen by OSIRIS are discussed in Chapter 5. It is shown that such an addition improves OSIRIS ozone profile quality for all times in the OSIRIS mission. The systematic errors introduced by the time-independent spectral point

spread function are minimized, making it possible to compare the impact of using different ozone cross sections within SASKTRAN as desired by the ACSO Commission. Chapter 6 provides the conclusions to be made from these results and discusses possible future paths of work.

Chapter 2

Background

Ozone is only a trace gas within the atmosphere, but it plays a vital role in atmospheric dynamics and is also critical for the well being of life on Earth. Such characteristics make the study of atmospheric ozone a priority for researchers worldwide. The OSIRIS instrument onboard the Odin spacecraft is a precision-engineered device capable of taking continuous measurements of solar radiation scattered by the atmospheric limb into the OSIRIS line of sight. Together with the SASKTRAN radiative transfer model and SaskMART iterative retrieval technique, OSIRIS measurements are used to produce detailed vertical number density profiles of ozone and other atmospheric constituents. Recent analysis by *Adams et al.* (2013) has revealed systematic errors in the retrieved ozone profiles, errors believed to be caused by OSIRIS temperature fluctuations altering the path of light through the instrument, a situation that is unaccounted for in the algorithms used to model the atmosphere as observed by the OSIRIS optical spectrograph. It is possible to eliminate these systematic errors via the development of a time-dependent spectral point spread function for use within these modelling algorithms. Further analysis has shown that a time-dependent spectral point spread function may also be necessary before the OSIRIS team can make a contribution to the Absorption Cross Sections of Ozone (ACSO) Commission, which has a goal of standardizing the ozone cross section used by atmospheric researchers worldwide.

2.1 Atmospheric Ozone

It has been speculated by *Berkner and Marshall* (1965) that the development of ozone in the Earth's atmosphere was a precursor for the development of life on Earth. As the amount of atmospheric ozone increased from negligible levels and absorbed incoming ultraviolet ra-

diation, it became possible for life to exist near the surface of oceans. Further increases in atmospheric ozone provided enough protection from ultraviolet light that life could be sustained on land, beginning the chain of events that led to the evolution of humanity. Currently, ozone constitutes less than one millionth of the mass of the atmosphere (*Cunnold et al.*, 1975), yet it creates a sufficient shield to protect the entire biosphere (*Ballaré et al.*, 2001).

Ozone also plays a fundamental role in the dynamics of the atmosphere. The lowest region of the atmosphere, called the troposphere, ranges from the ground to 10–15 km altitude and contains minimal levels of ozone. In this region the temperature of the atmosphere decreases with increasing altitude, creating an unstable turbulent environment where the air mixes relatively quickly and leads to events that are commonly described as "weather" such as thunderstorms, blizzards and tornadoes. Above the troposphere is the stratosphere, a region that extends from 10–15 km to approximately 50 km altitude and contains the vast majority of atmospheric ozone. The stratospheric ozone readily absorbs incident ultraviolet light, a process which converts the energy of the incident photon into thermal energy and raises the temperature of the atmosphere. The rate of energy deposition per unit mass increases with altitude until a maximum is reached at the top of the stratosphere (*Whitten and Prasad*, 1985), creating a situation where atmospheric temperature increases with altitude (*Dessler*, 2000). The air in the stratosphere is therefore said to be "stratified", creating a stable environment that undergoes very little vertical mixing and a situation where particles that enter the stratosphere tend to remain there for relatively long periods of time. The impact of stratospheric particle longevity can be seen when large volumes of particles are injected into the stratosphere, an event that frequently occurs with large volcanic eruptions (*Bourassa et al.*, 2012). Particles that would be removed from the turbulent troposphere in a matter of days can linger in the stratosphere for months or even years, impacting the radiative balance of the Earth and causing global changes in surface temperatures.

2.1.1 Atmospheric Ozone Chemistry

The first successful attempt to describe the chemical reactions of atmospheric ozone was made by *Chapman* in 1930. He suggested that atmospheric ozone is created by a photodissociation

of O_2 to form O atoms, which then reacted with O_2 molecules to create ozone. As chemical equations, these reactions are given as

$$O_2 + \frac{hc}{\lambda} \rightarrow 2O, \tag{2.1}$$

$$O + O_2 + M \rightarrow O_3 + M, \tag{2.2}$$

where $\frac{hc}{\lambda}$ defines a photon of wavelength λ to be absorbed. Planck's constant is represented by h while c is the speed of light. The variable M represents another atmospheric particle used to carry away the excess energy. Atmospheric ozone molecules are then destroyed in one of two reactions, the first of which is another photodissociation,

$$O_3 + \frac{hc}{\lambda} \rightarrow O_2 + O, \tag{2.3}$$

while the second is a combination of an O_3 molecule and an O atom to form two O_2 molecules,

$$O_3 + O \rightarrow 2O_2. \tag{2.4}$$

To describe the balance of O, O_2 and O_3 within the atmosphere it is helpful to define a new constituent called odd oxygen, O_x, as the sum of O and O_3. Atmospheric odd oxygen is created in reaction 2.1 and destroyed in reaction 2.4. Reactions 2.2 and 2.3 simply allow the different forms of odd oxygen, O and O_3, to transition to the other form when the opportunity allows and result in no net change in the amount of O_x. It turns out that the time scale for the creation and destruction of stratospheric odd oxygen is on the time scale of days to months (*Dessler*, 2000), meaning that on shorter time scales the amount of odd oxygen is constant. This does not, however, mean that reactions 2.2 and 2.3 are not occurring. In actuality the time scale for reactions 2.2 and 2.3 is on the order of tens of minutes (*Dessler*, 2000), meaning that O and O_3 are constantly interchanging amongst themselves while the total amount of O_x remains constant. An important consequence of the constant interchange between O and O_3 is that the incident radiation in reaction 2.3 is not re-emitted into the atmosphere; instead, the energy gained from its absorption is converted to thermal energy in reaction 2.2, increasing atmospheric temperature and leading to the formation of the stratosphere.

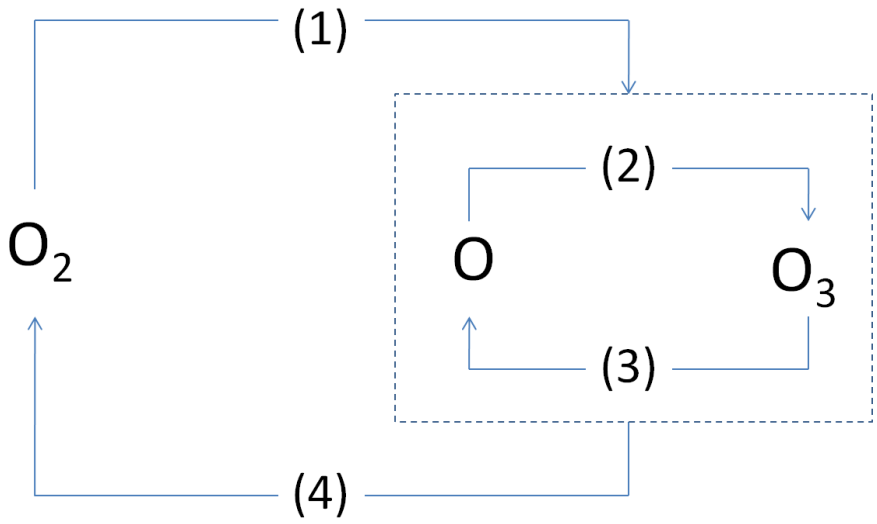

Figure 2.1: The odd-oxygen cycle of Earth's atmosphere. The numbers represent reactions 2.1-2.4.

Together, these four reactions form what is known as the odd-oxygen cycle which is visually shown in Figure 2.1.

2.2 The OSIRIS Instrument on the Odin Spacecraft

Satellite technology provides a wealth of opportunity for researchers to study Earth's atmosphere on a global scale. The OSIRIS instrument on the Odin satellite has been active since 2001, and its combination of high quality measurements and long operational lifetime has made it highly regarded among the atmospheric research community.

2.2.1 Satellite Measurements Using Limb Scattered Light

Satellite instruments have been an essential tool for observing and understanding the atmosphere since the early days of the space age in the 1960s. The first atmospheric observing satellites recorded their measurements from one of two configurations. If atmospheric profiles with excellent vertical resolution were desired then the occultation configuration was chosen, wherein the instrument looks directly at the sun and takes measurements of the solar spectrum every time the sun rises or sets through Earth's atmosphere. By comparing the solar

spectra recorded at various tangent altitudes against the raw solar spectrum, absorption and scattering features can be easily distinguished and a high resolution vertical profile of the atmosphere can be determined. The disadvantage to the occultation configuration is that the instrument can only take measurements at two points in each orbit, resulting in relatively poor global coverage.

If excellent global coverage was required then the nadir configuration was selected. A satellite observing the atmosphere in the nadir configuration always looks directly downward at the Earth and constantly gathers information about the atmosphere below it when orbiting over sunlit atmosphere. The major drawback of looking directly downward is the inability to observe individual altitudes within the atmosphere, meaning that nadir instruments produce poor vertical profiles relative to those produced by occultation instruments.

Recently, a new method of atmospheric remote sensing called limb scatter has been implemented into the design of a number of satellite-based instruments. Rather than looking directly downward or at the sun, instruments using limb scatter observe the limb of the atmosphere through a "side-view" method displayed in Figure 2.2. Limb scatter instruments measure solar radiation whose final interaction with the atmosphere was a scattering event that directed the radiation into the line of sight of the instrument. As a result of the atmospheric interactions the solar spectrum recorded by limb scatter instruments is imprinted with the signatures of scattering and absorption by atmospheric particles present in the volume near the instrument line of sight. Limb scatter instruments are designed to have a narrow line of sight and the ability to quickly point the line of sight at different tangent altitudes in the atmosphere, giving researchers the ability to construct detailed vertical profiles of the atmosphere. Also, because limb scatter instruments can continuously take measurements they are able to provide excellent global coverage. In this way the limb scatter technique provides the benefits of both the occultation and nadir configurations, greatly increasing both the amount and quality of data available to researchers.

The geometry of a limb scatter measurement can be fully defined using the coordinates shown in Figure 2.2. The tangent point of the line of sight is defined as the closest point between the line of sight and the Earth's surface; this location is generally used to define the measurement. The location on the Earth's surface directly beneath the tangent point defines

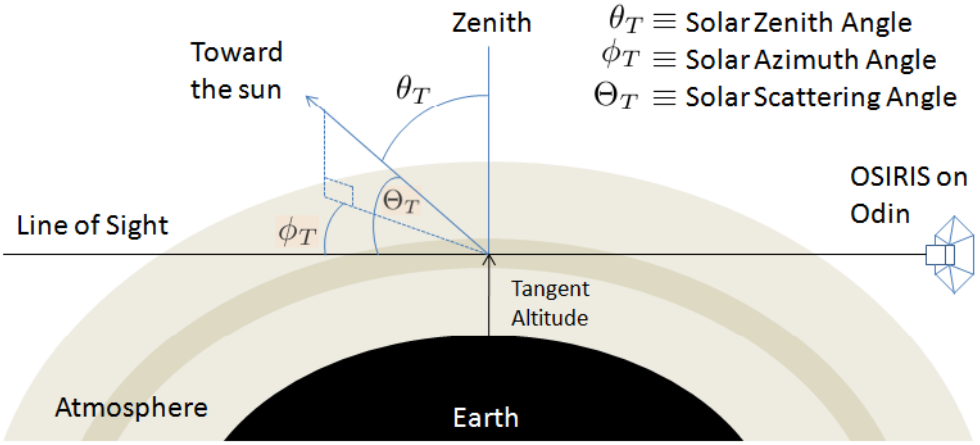

Figure 2.2: Limb Scatter Geometry.

the latitude and longitude of the measurement. The solar coordinates of the measurement are defined by the three angles displayed in Figure 2.2. The solar zenith angle, θ_T, is taken as the angle from zenith at the tangent point to the solar direction. The solar azimuth angle, ϕ_T, is measured from the horizontal projection of the solar direction to the line of sight. The solar scattering angle, Θ_T, is the angle measured directly from the solar direction to the line of sight. These three angles combined with the latitude and longitude of the tangent point define a fully three dimensional geometry associated with the measurement (*Bourassa et al.*, 2007).

2.2.2 The OSIRIS Instrument

The Optical Spectrograph and Infrared Imaging System (OSIRIS) is a Canadian designed and built instrument developed to measure the atmospheric limb radiance of scattered sunlight (*Llewellyn et al.*, 2004). The instrument has been in full operation onboard the Swedish satellite Odin since shortly after being launched into orbit on February 20th, 2001 (*Murtagh et al.*, 2002). Odin follows a circular, sun-synchronous dusk/dawn orbit at an altitude near 600 km with a period of approximately 96 minutes. OSIRIS observes the atmosphere by looking within Odin's orbital plane which is inclined at 97.8° from the equator, allowing for measurements to be taken within a latitude range of 82°S to 82°N as the line of sight is pointed within the orbit plane. The local time of the ascending node of the orbit (the northward

equatorial crossing) is 1800h, while the local time of the descending node (the southward equatorial crossing) is 0600h. The satellite remains near the terminator throughout the duration of its orbit, remaining close to local dusk along the entire ascending track and close to local dawn along the descending track. It quickly sweeps through noon at high northern latitudes and midnight at high southern latitudes.

The work of this thesis focuses exclusively on the optical spectrograph component of OSIRIS which records data over two wavelength ranges, the first being 280–485 nm and the second being 535–810 nm. The entire satellite nods up and down so that OSIRIS can observe tangent altitudes from 10 km to 70 km. A single OSIRIS spectrograph exposure lasts between 0.1–10 seconds depending on the tangent altitude under observation. All of the exposures taken during a single nod up or down constitute a scan of the atmosphere. An example of data collected during a typical OSIRIS scan is shown in Figure 2.3, which makes it clear that the radiance observed by OSIRIS is both tangent altitude and wavelength dependent. The tangent altitude dependence is a result of the exponential decrease in atmospheric particle concentration with increasing altitude; smaller concentrations of particles create fewer scattering events, thus the signal observed by OSIRIS decreases with altitude. The wavelength dependence is a result of both the incident solar signal and the interactions of this signal with the atmosphere, the latter of which is essential in determining atmospheric chemical composition. Measurements are not taken in the 485–535 nm wavelength range due to an instrumental effect discussed in more detail in Section 2.3.5. A single scan takes approximately 90 seconds to complete, yielding approximately 60 scans of Earth's atmosphere per orbit.

2.3 The OSIRIS Optical Spectrograph

Solar radiation scattered by Earth's atmosphere is collected by the optical spectrograph component of OSIRIS and subsequently analyzed to reveal information regarding the composition of the atmosphere. For this thesis work an understanding of the internal workings of the spectrograph is essential. The spectrograph is made up of a series of baffles and vanes, multiple mirrors, a field-of-view limiting slit, a diffraction grating, an element that is a combination field-flattener/order sorter/prism, and a CCD detector. In order to familiarize the reader

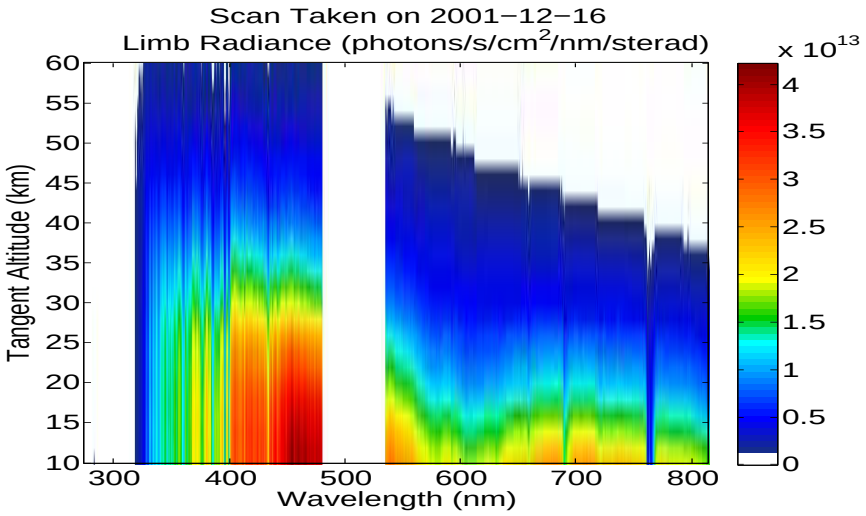

Figure 2.3: The limb radiance of a typical OSIRIS scan.

with the physical design and basic optical configuration of OSIRIS a schematic of the entire instrument (both the optical spectrograph and infrared imager) and a diagram showing the simplified paths of light through the instrument, both first published in *Llewellyn et al.* (2004), are shown in Figures 2.4 and 2.5 respectively.

2.3.1 Design Requirements

To collect the necessary data and further the scientific community's understanding of Earth's atmosphere the OSIRIS spectrograph had to meet several design requirements. While the complete list of requirements can be found in *Warshaw et al.* (1996), the most important are:

- Cover a wavelength range of 280–810 nm. A large number of important atmospheric constituents are efficient absorbers at different wavelengths in this range, including O_3, NO_2, BrO, and O_2.

- Provide spatial resolution capable of delivering detailed vertical radiance profiles of the atmosphere from which profiles of atmospheric constituents can be retrieved.

- Have a dynamic range that is capable of detecting all possible signals that could potentially be observed. Signals from the highest altitudes of a typical OSIRIS scan (70 km)

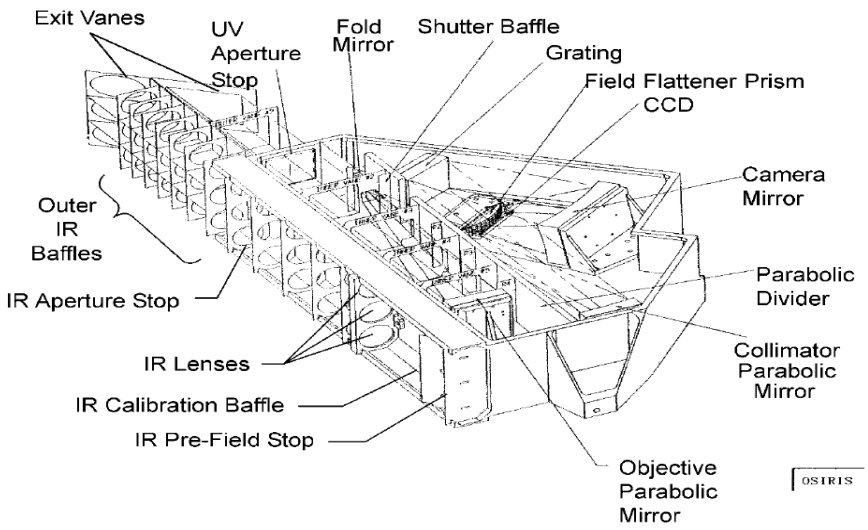

Figure 2.4: The OSIRIS Instrument (*Llewellyn et al.*, 2004).

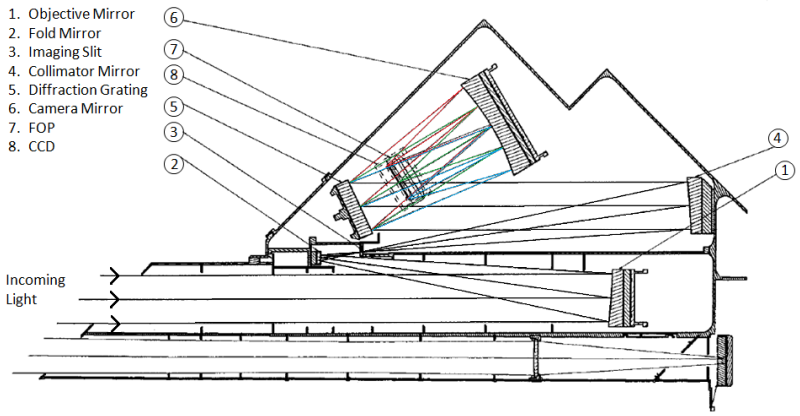

Figure 2.5: Path of light rays through the optical spectrograph (*Llewellyn et al.*, 2004).

are orders of magnitude weaker than the signals at the lowest OSIRIS scan altitudes (10 km). Also, at low OSIRIS scan altitudes certain wavelengths will have a signal orders of magnitude lower than other wavelengths due to the wavelength dependence of phenomena such as Rayleigh scattering and ozone absorption.

2.3.2 Incoming Radiation

Radiation entering the OSIRIS optical spectrograph first passes through a square entrance aperture with dimensions of 36mm x 36mm. A series of baffles and vanes placed directly behind the entrance aperture are used to reduce external stray light occurring due to the bright nature of the atmospheric limb. Any external stray light can cause significant off-axis signals and therefore must be eliminated to prevent contamination of the on-axis signal. *Llewellyn et al.* (2004) found that despite the presence of the baffles and vanes the amount of stray light can become significant at certain wavelengths and tangent altitudes, but were able to develop methods to computationally remove this stray light when it becomes an issue.

2.3.3 Mirrors & Limiting Slit

Once the incoming light has passed through the series of baffles and vanes, it falls upon the first of two twin off-axis parabolic mirrors, the objective mirror (Item 1 in Figure 2.5). The purpose of the objective mirror is to transform the incident collimated light into light that converges at the mirror's focus. The use of off-axis mirrors provides two major advantages over lenses. Firstly, mirrors are immune to chromatic aberration, an issue that is difficult to correct in lenses. Secondly, off-axis parabolic mirrors allow the reflected light to be focused at a location that is not in the path of the incident light as shown in Figure 2.6. The path of the light can therefore be folded, allowing the light to interact with all optical elements in a minimal amount of physical space (*Warshaw et al.*, 1996).

After the light has reflected off the first parabolic mirror it travels to the fold mirror (Item 2 in Figure 2.5), a flat mirror whose sole purpose is to keep the physical size of the spectrograph to a minimum. The fold mirror directs the light to the second of the twin off-axis parabolic mirrors, the collimator mirror (Item 4 in Figure 2.5). While travelling from

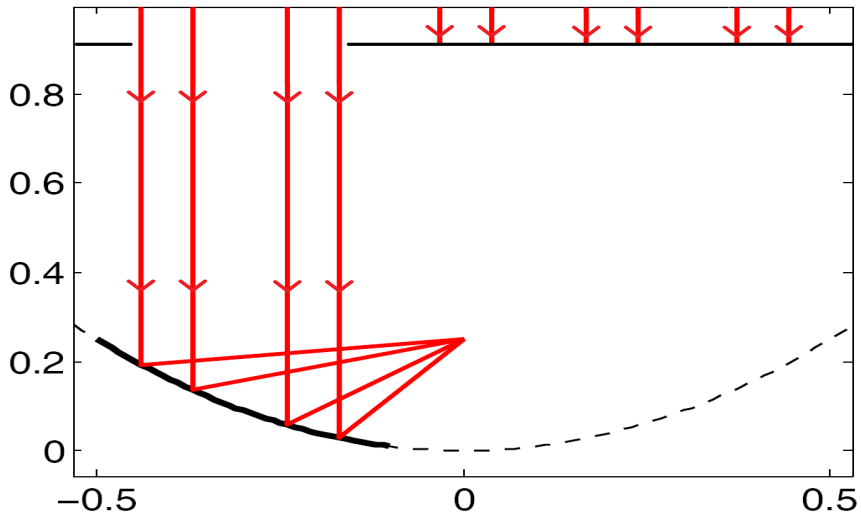

Figure 2.6: The focal point of off-axis parabolic mirrors is not in the path of the incident light.

the fold mirror to the collimator mirror the light reaches the focal point of the objective mirror and forms a real image. Located at this focal point is Item 3 in Figure 2.5, the 90 μm wide field-of-view limiting slit, which is orientated horizontally and perpendicular to the plane of the spacecraft's orbit as shown in Figure 2.7. The purpose of this slit is to only allow light from a 1 km vertical by 40 km horizontal field of view of the tangent point to pass through to the rest of the spectrograph.

The orientation of the slit and the field-of-view that it passes were chosen for a number of reasons. As discussed in *Warshaw et al.* (1996), initial spectrograph designs called for a vertical slit to allow for multiple tangent altitudes to be measured at the same time. However, this design encountered two major problems. The dynamic range required for a single exposure across all tangent altitudes increased beyond an acceptable limit due to the exponential decrease of scattered light with altitude, and Odin's downlink data rate was insufficient to transmit data that varied with both wavelength and altitude (*Warshaw et al.*, 1996). For these reasons a horizontal slit with a 1 km vertical resolution was chosen and the satellite itself would nod to scan the various tangent altitudes of interest. A 1 km vertical resolution was chosen as it provides sufficient data over the altitude range of a typical OSIRIS scan to generate detailed vertical profiles of atmospheric constituents while still gathering

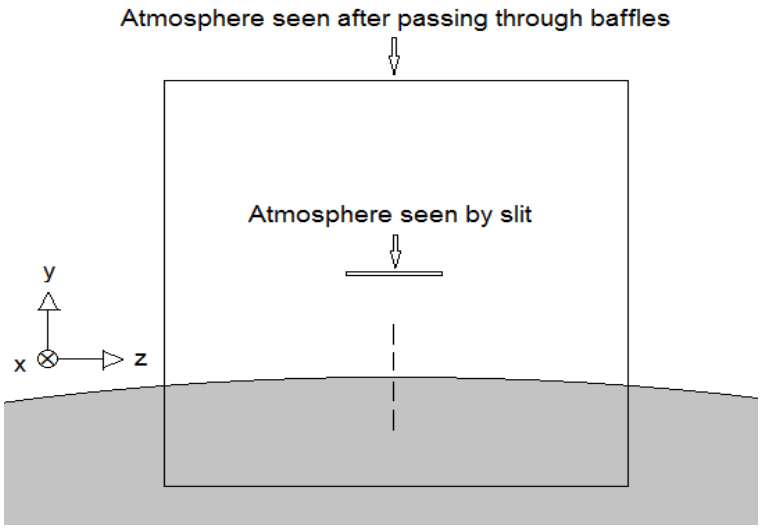

Figure 2.7: The atmosphere as seen by the OSIRIS spectrograph. The satellite orbit is in the XY plane.

enough information to maintain a high signal-to-noise ratio.

The light that passes through the slit can be treated as light whose source is the focal point of the objective mirror. The OSIRIS instrument is designed such that the focal point of the collimator mirror is located at the same location as the focal point of the objective mirror. As a result of this configuration the light incident on the collimator mirror will be transformed into collimated light upon reflection (see Figure 2.6). The collimated light is identical to the light that was originally incident on the OSIRIS instrument except that it consists of only the 40 km horizontal by 1 km vertical section of the atmosphere observed by the slit. This image of the slit then propagates to Item 5 in Figure 2.5, the diffraction grating.

2.3.4 The Diffraction Grating

Diffraction gratings are used to separate a polychromatic beam of light into its components so that each wavelength of light included in the incident beam can be individually studied. The grating equation, which gives the outgoing angles of the intensity maxima, θ_m, for light of a certain wavelength incident normal to the grating, is given as

$$\theta_m = \sin^{-1}\left(\frac{m\lambda}{d}\right), \tag{2.5}$$

where d is the separation between grating lines, λ is the wavelength of light and m is an integer indicating the order of diffracted light. The diffraction grating of the OSIRIS spectrograph is a reflective grating with a density of 600 lines/mm and sorts first order light with a wavelength range of 280 to 810 nm (*Warshaw et al.*, 1996). The image of the slit is diffracted only in the vertical direction, revealing the spectrum of the atmosphere at that altitude. Once diffracted, the light travels to a spherical camera mirror (Item 6 in Figure 2.5) which redirects the light out of the plane of the rest of the optical elements and towards an element that serves multiple roles, the field-flattener/order sorter/prism (FOP).

2.3.5 The FOP

The combination field-flattener/order sorter/prism (FOP), shown as Item 7 in Figure 2.5, prepares the light to interact with the CCD detector (Item 8 in Figure 2.5) and is the only refractive element in the entire spectrograph system. The field-flattener is necessary as it is not physically possible to engineer an optical system with a perfectly flat focal plane, a problem visually shown in Figure 2.8. The CCD detector of the OSIRIS spectrograph has a flat detecting surface, meaning that because of the curved focal plane only a small fraction of the diffracted slit image would be properly focused. The field flattener corrects this problem by refracting the incoming light and creating a focal plane that is sufficiently flat for the purposes of the OSIRIS mission.

The second element of the FOP, the order sorter, is necessary because the diffraction grating of the spectrograph naturally produces many orders of diffracted light of which only the first order is desired for measurements. Second order light with a maximum wavelength of 405 nm overlaps the first order light up to 810 nm and if not blocked would be observed by the CCD detector. The order sorter consists of two adjacent pieces of glass, the first of which is clear and allows the first order light through while the second blocks light with wavelengths shorter than 455 nm, eliminating all significant second order light. A consequence of this order sorter is that first order light in the 485–535 nm wavelength range interacts with the

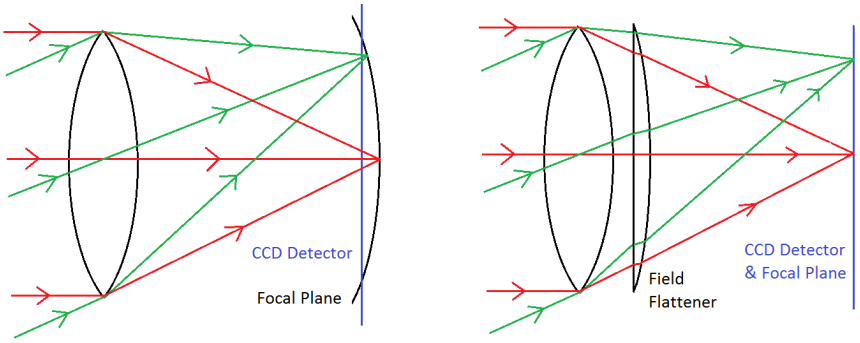

Figure 2.8: Field flatteners accommodate for the curved focal plane inherit to all optical systems.

connection point of the two glass pieces, causing complex interactions that yields light in this range unusable. Measurements are therefore not kept from 485–535 nm, creating the gap in data observed in Figure 2.3.

The final element of the FOP, the prism, serves the purpose of minimizing spectral cross-talk (*Llewellyn et al.*, 2004). It is not possible to build an optical element that behaves perfectly as described in theory; there will always be imperfections due to optical phenomena and the limitations of engineering such elements. As a result, all optical elements in the OSIRIS spectrograph have the potential to create a small but noticeable amount of internal stray light. To minimize the stray light observed by the CCD detector, a 45° total internal reflection prism is included as the final element of the FOP. The diffracted image of the slit that has successfully passed through all optical elements thus far enters the prism and undergoes total internal reflection, after which it is observable by the CCD detector. The spectrograph is designed such that any internal stray light reaches the prism with a large angle of incidence and as such is reflected away from the CCD detector, ensuring that only the image of the slit advances to the final element of the spectrograph.

2.3.6 The CCD Detector

Charge-Coupled Devices (CCDs) are integrated circuits composed of an array of light-sensitive pixels, each of which is capable of converting incident light into a measurable electric charge that is directly proportional to the intensity of the light. A more detailed discussion on the

underlying physics of these devices is given in *Kasap* (2001). CCDs operate by having a focused image projected onto the array of pixels, each of which converts the incident light to electric charge for a set exposure time. Once exposure has ended, the collected charges are then clocked out by passing them along a row or column of the array to a final readout register, which dumps the charge into a charge amplifier after which it is converted to a recordable voltage.

The OSIRIS spectrograph uses a frame transfer CCD, a specialized type of CCD that consists of two areas with the same amount of pixels: an active imaging area that is exposed to light and a permanently shielded readout area (*Murtagh et al.*, 2002). For every exposure an image of the diffracted slit is formed on the active imaging area where the pixels convert the image into a measurable charge. After a pre-determined length of time the charges are quickly passed to the readout area. It is vital that the charges be passed quickly between the two regions as the pixels are still exposed to light and a slow transfer may result in vertical smearing of the data. Once in the shielded readout area, the charges can be passed pixel-by-pixel to the readout register at a rate slow enough to ensure a correct measurement of each cell's charge.

Both the active imaging area and readout area of the CCD detector in the OSIRIS spectrograph are made up of an array of 1353 by 143 pixels. Each pixel is 20 x 27 μm in size with the 20 μm side in the 1353 pixel direction. To get a sense of the final diffracted slit image formed on the CCD detector, consider Figure 2.9 which displays the final projected image for a hypothetical scenario where the atmosphere observed by the OSIRIS spectrograph produces a signal consisting of only three wavelengths of light. The vertical portion of slit image, which covers 1 vertical km of the atmosphere, is dispersed by the diffraction grating, creating three monochromatic slit images which are projected onto separate regions of the CCD. In reality the vertical portions of all wavelengths in the 280–810 nm range are dispersed, creating a continuum of monochromatic slit images which are projected over 1353 pixel columns. The horizontal portion of each monochromatic slit image, which covers approximately 40 km of horizontal atmospheric limb, is spread over 32 of the 143 pixel rows. As the observed atmosphere in these 40 km is essentially homogeneous, the measured signals of the 32 pixels are binned together to improve the signal-to-noise ratio. The 1353 binned

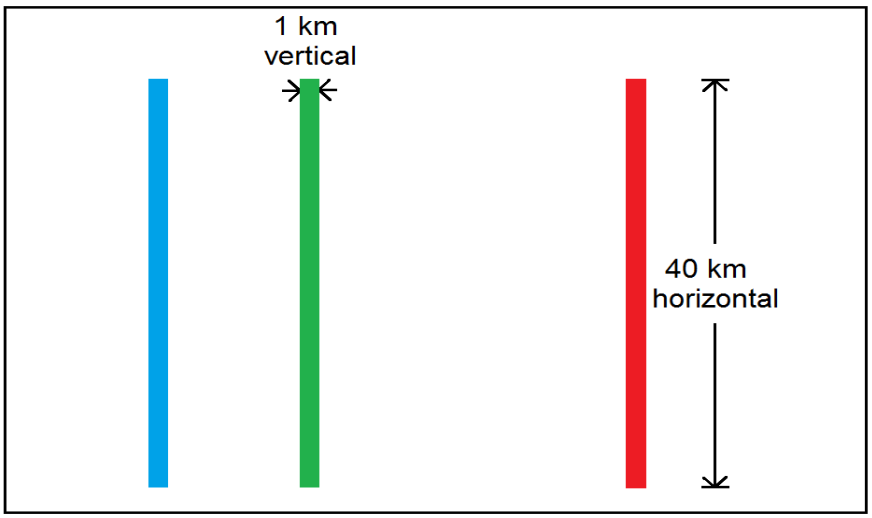

Figure 2.9: The diffracted slit image seen by the CCD detector for a hypothetical incident signal composed of monochromatic blue, green and red light.

signals constitute the final measurement that is recorded, transmitted to Earth, and made available to researchers around the world.

2.4 The SASKTRAN Radiative Transfer Model

The OSIRIS instrument is truly a remarkable feat of science and engineering. The difficulty of designing, building, and launching a satellite capable of consistently high quality measurements over such a long time frame cannot be overstated. And while these measurements are certainly valuable on their own, it is only possible to unlock their true potential by coupling them with a state-of-the-art radiative transfer model.

2.4.1 Radiative Transfer Models

Satellite instruments that passively observe Earth's atmosphere typically measure light that has interacted with the atmosphere and been directed into the satellite's line of sight. Radiative transfer models are the tools researchers use to extract important atmospheric information from the raw satellite data. The objective of all radiative transfer models is to accurately model the propagation of light through a planetary atmosphere. Models that successfully

replicate the passage of light through an atmosphere as seen by a satellite instrument can be used alongside the satellite data in inversion algorithms to retrieve information about atmospheric composition.

The configuration of the satellite instrument defines the criteria necessary to create a successful model of the atmosphere. For example, nadir viewing instruments such as the Solar Backscatter Ultraviolet (SBUV) experiment on the Nimbus 7 satellite (*Heath et al.*, 1975) can successfully retrieve atmospheric information using radiative transfer models that employ a plane-parallel atmosphere (*Bhartia et al.*, 1996). The view of the atmosphere as seen by limb scatter instruments such as OSIRIS prevents the use of a plane-parallel geometry in modelling (*Collins et al.*, 1972), requiring the models of limb scatter instruments to be designed in a wholly different way than nadir viewing instruments.

OSIRIS measurements are analyzed using the SASKTRAN radiative transfer model, a model developed specifically for OSIRIS at the University of Saskatchewan (*Bourassa et al.*, 2007). As first discussed in *Bourassa et al.* (2007), the defining criteria of the SASKTRAN model are:

- A spherical shell atmosphere of homogeneous cells with variable thickness.
- Scattering by molecules and aerosols with an altitude dependent cross section and phase function.
- Absorption by an extensible list of temperature dependent species.
- Estimation of n-order scattering by the method of successive orders along rays traced within the spherical geometry.
- Specialized numerical integration over the unit sphere that exploits the characteristics of the intensity field in order to optimize the ray tracing.

With the criteria defined, it is now a matter of successfully modelling how light propagates through the SASKTRAN atmosphere. However, before any modelling can be undertaken the background and fundamentals of the theory of radiative transfer must be established.

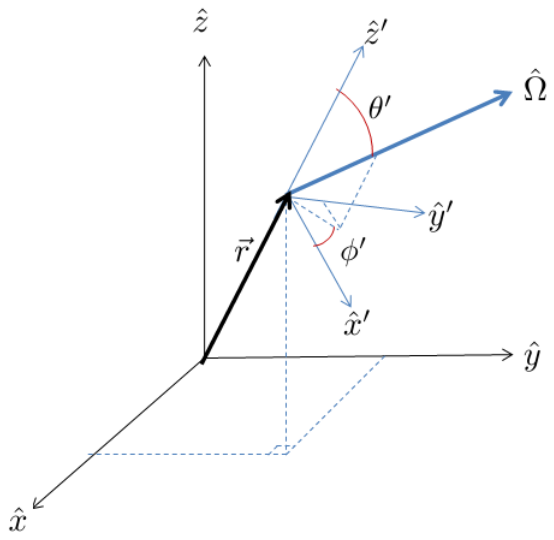

Figure 2.10: The radiation field coordinate system.

2.4.2 Radiative Transfer Theory

The Radiation Field

All radiative transfer models have their base in the five dimensional equation of transfer first presented by *Chandrasekhar* (1960). Figure 2.10 shows the necessary configuration for this equation. Cartesian coordinates $\hat{x}$, $\hat{y}$, and $\hat{z}$ are used to define the position vector $\vec{r}$. A second set of Cartesian coordinates, $\hat{x}'$, $\hat{y}'$, and $\hat{z}'$ are defined such that the $\hat{z}'$ vector is in the same direction as $\vec{r}$. This second set of coordinates is used to define angular coordinates θ' and ϕ' which in turn define the unit direction of propagation $\hat{\Omega}$. Together, the coordinates $\hat{x}$, $\hat{y}$, $\hat{z}$, θ' and ϕ' fully describe a randomly polarized, monochromatic radiance, $I(\vec{r}, \hat{\Omega})$, of any magnitude.

As shown in Figure 2.11, the radiance $I(\vec{r}, \hat{\Omega})$ is defined as the amount of radiant energy, dE, in a specified wavelength interval $(\lambda, \lambda + d\lambda)$ that crosses an element of area dA in a direction limited to a solid angle $d\Omega$ during time dt (*Chandrasekhar*, 1960). As an equation this relationship is written as

$$I(\vec{r}, \hat{\Omega}) = \frac{dE}{d\lambda \, dA \, d\Omega \, dt}. \tag{2.6}$$

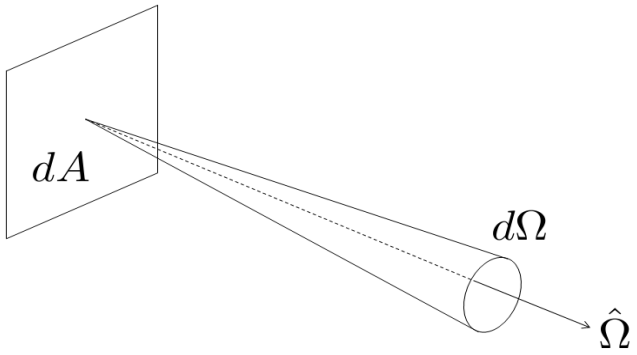

Figure 2.11: The defining configuration for radiance $I(\vec{r}, \hat{\Omega})$.

If the radiant energy is defined in terms of photons, the resulting units of Equation 2.6 are

$$[I(\vec{r}, \hat{\Omega})] = \left[\frac{\text{photons}}{\text{s cm}^2 \text{ nm sterad}}\right]. \tag{2.7}$$

Often it is desirable to define the radiation field in terms of the transport of radiation from one point to another. To accomplish this the path coordinate s is introduced and used to define a point in the atmosphere $\vec{r}$ as a function of an observation point $\vec{r_0}$ and distance along the propagation direction $\hat{\Omega}$, or

$$\vec{r} = \vec{r_0} + s\hat{\Omega}. \tag{2.8}$$

Important features of Equation 2.8 are that the radiation travelling in the direction of $\hat{\Omega}$ reaches the observation point when s equals zero and that s increases in the direction of $\hat{\Omega}$ as shown in Figure 2.12. Using this configuration the position vector $\vec{r}$ and propagation direction $\hat{\Omega}$ first introduced in Equation 2.6 are implied by the path coordinate s. Therefore, for the remainder of this work the following definition will be used,

$$I(\vec{r}, \hat{\Omega}) \equiv I(\vec{r_0}, \hat{\Omega}, s) \equiv I(s). \tag{2.9}$$

The Beer-Lambert Law & The Extinction Term

The attenuation of light as it passes through a non-vacuum medium is defined by the Beer-Lambert Law. Consider light incident on a section of atmosphere with infinitesimal thickness

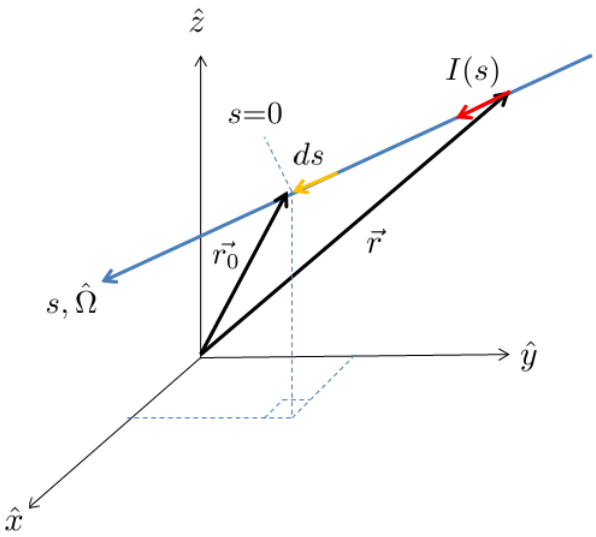

Figure 2.12: The Path Length Coordinate, s.

ds. The volume number density of each atmospheric species present is given by $n(s)$ and the probability of the light interacting with each species is given in units of area by the species cross section $\sigma(s)$. The Beer-Lambert law states that the change in intensity of light after it has passed through the section is given by

$$dI(s) = -I(s)ds \sum_i n_i(s)\sigma_i(s), \tag{2.10}$$

where i represents each atmospheric species present. The summation in Equation 2.10 is also known as the extinction of the incident beam, $k(s)$, which occurs from a combination of scattering and absorption of light by atmospheric particles and has units of inverse length,

$$k(s) = \sum_i n_i(s)\sigma_i(s). \tag{2.11}$$

Inserting the result of Equation 2.11 into Equation 2.10 and rearranging the terms leads to the differential equation

$$\frac{dI(s)}{I(s)} = -k(s)ds \tag{2.12}$$

from which the radiance observed at a point along the path s_0 can be determined by integrating from the source of the radiance, s_1, to s_0 as seen in

$$\int_{I(s_1)}^{I(s_0)} \frac{dI(s)}{I(s)} = -\int_{s_1}^{s_0} k(s)ds. \tag{2.13}$$

At this time it is beneficial to define the optical depth, τ, as the fraction of light attenuated after passing through a length of atmosphere l, or

$$\tau = kl. \tag{2.14}$$

With this definition it is possible to define the optical depth between path points s and $s+ds$ as

$$d\tau(s) = -k(s)ds. \tag{2.15}$$

The negative sign is a consequence of the path coordinate s and is necessary to ensure that if one begins at the observation point and moves outward along the path towards the source of the radiance the total optical depth will be positive and increase with distance. Equation 2.15 can be substituted into Equation 2.13 and solved such that the radiance at point s_0 can be defined as a function of the radiance at any point on the path, s, and the optical depth from s to s_0, $\tau(s, s_0)$. In equation form, this process is shown as

$$\begin{aligned} \int_{I(s)}^{I(s_0)} \frac{dI(s)}{I(s)} &= \int_{\tau(s)}^{\tau(s_0)} d\tau(s), \\ \ln\left(\frac{I(s_0)}{I(s)}\right) &= \tau(s_0) - \tau(s), \\ \text{and} \quad I(s_0) &= I(s)e^{-\tau(s,s_0)}. \end{aligned} \tag{2.16}$$

In the case where s_0 is at the observation point ($s_0 = 0$), $\tau(s_0) = 0$ and the solution simplifies to

$$I(0) = I(s)e^{-\tau(s)} \tag{2.17}$$

which is the common form of the Beer-Lambert law, and also the extinction term of what will become the radiative transfer equation.

The Ground Term

Any spherical surface that emits or reflects radiation produces an outgoing radiant flux density $F_{up}(\vec{r}, \hat{n})$, where $\hat{n}$ is a unit vector perpendicular to the surface. The outgoing radiant flux density can be defined in terms of the outgoing radiance $\tilde{I}(\vec{r}, \hat{\Omega})$ by integrating the projection of the radiance along $\hat{n}$ over the solid angle of the outgoing hemisphere. As an equation, this is given as

$$F_{up}(\vec{r}, \hat{n}) = \int_{2\pi} \tilde{I}(\vec{r}, \hat{\Omega}) \cos(\theta) d\Omega, \tag{2.18}$$

where θ is the angle between the vectors $\hat{\Omega}$ and $\hat{n}$. To simplify this integral, it is common practice to make the assumption that the emitting or reflecting surface is a *Lambertian* surface; the emitted or reflected energy from a surface area element varies with the cosine of the surface normal. Under this assumption, the radiance of a surface area element is the same for all viewing directions. The use of a Lambertian surface allows the radiance in Equation 2.18 to be defined solely as a function of $\vec{r}$, as seen in

$$\begin{aligned} F_{up}(\vec{r}, \hat{n}) &= \tilde{I}(\vec{r}) \int_{2\pi} \cos(\theta) d\Omega, \\ &= \tilde{I}(\vec{r}) \int_0^{2\pi} \int_0^{\frac{\pi}{2}} \cos(\theta) \sin(\theta) d\theta d\phi, \\ \text{and} \quad &= \pi \tilde{I}(\vec{r}). \end{aligned} \tag{2.19}$$

Surfaces in nature that reflect radiant flux are rarely perfect reflectors; the amount of upward reflected flux $F_{up}(\vec{r}, \hat{n})$ is normally less than the amount of downward incoming flux $F_{down}(\vec{r}, \hat{n})$, a term that will be discussed in greater detail shortly. The ratio of these two values is defined as the *albedo*, a, which is given by

$$a = \frac{F_{up}(\vec{r}, \hat{n})}{F_{down}(\vec{r}, \hat{n})}. \tag{2.20}$$

Combining Equations 2.19 and 2.20 indicates that for a downwelling flux on a Lambertian surface with an albedo, a, the observed reflected radiance will be

$$\tilde{I}(\vec{r}) = \frac{a}{\pi} F_{down}(\vec{r}, \hat{n}). \tag{2.21}$$

In the SASKTRAN model, light described by Equation 2.21 only occurs due to reflection off the Earth. Equation 2.21 will therefore be referred to as the ground term for the remainder of this work.

The Source Term

The attenuation of radiation in the atmosphere primarily occurs due to one of two phenomena. Atmospheric particles can elastically scatter radiation out of its initial path or they can absorb the radiation and remove it from the atmosphere completely. To represent this, the extinction term $k(s)$ can be broken down into two unique extinction values representing atmospheric scattering and absorption,

$$k(s) = k_{scatt}(s) + k_{abs}(s). \tag{2.22}$$

It is common practice to define the ratio of scattering extinction and total extinction as the single scatter albedo, $\tilde{\omega}_0$, where

$$\tilde{\omega}_0 = \frac{k_{scatt}(s)}{k(s)}. \tag{2.23}$$

The scattering of radiation is one of three sources that can significantly increase the observed radiance, the other two being thermal emission of blackbody radiation and photochemical emission (*Bourassa et al.*, 2007). In atmospheric radiative transfer these sources are accounted for via a source term $J(s)$. When this source term is included in the Beer-Lambert law of Equation 2.12, the resulting equation is

$$dI(s) = \left(-I(s)k(s) + J(s)k(s)\right) ds. \tag{2.24}$$

In the range of OSIRIS wavelengths the magnitude of scattered radiation greatly outweighs that of thermal emission (*Bourassa et al.*, 2007) allowing thermal emissions to be neglected. In regions where there is no photochemical emission $J(s)$ is defined as

$$J(s) = \frac{k_{scatt}(s)}{k(s)} \int_{4\pi} I(\vec{r}, \hat{\Omega}') p(s, \Theta) d\Omega', \tag{2.25}$$

where Ω' is the direction of the incident radiation to be scattered and Θ is called the scattering angle, defined as the angle between the incident and final propagation directions, or

$$\Theta = \cos^{-1}(\hat{\Omega}' \cdot \hat{\Omega}). \tag{2.26}$$

The effective phase function $p(s, \Theta)$ has units of inverse steradians and defines the probability of incoming radiation being scattered into the propagation direction. It is formulated by taking a weighted average of the phase functions of all scattering particles present at the scattering point. Equation 2.24 is an integro-differential equation and as such it is desirable to find another form of the equation that is easier with which to work. It is convenient at this point to express the source term in terms of the optical depth τ rather than the path coordinate s. The progression of a such a transition is given as

$$\begin{aligned}
J(s)ds &= \frac{k_{scatt}(s)}{k(s)} \int_{4\pi} I(\vec{r}, \hat{\Omega}') p(s, \Theta) d\Omega' ds; \\
J(s)k(s)ds &= \frac{-d\tau_{scatt}}{ds} \int_{4\pi} I(\vec{r}, \hat{\Omega}') p(s, \Theta) d\Omega' ds; \\
J(s)k(s)ds &= \frac{-d\tau_{scatt}}{d\tau} \int_{4\pi} I(\vec{r}, \hat{\Omega}') p(\tau, \Theta) d\Omega' d\tau; \\
J(s)k(s)ds &= -\tilde{\omega}_0 \int_{4\pi} I(\vec{r}, \hat{\Omega}') p(\tau, \Theta) d\Omega' d\tau; \\
\text{and} \quad J(s)k(s)ds &= -J(\tau) d\tau
\end{aligned} \tag{2.27}$$

which when applied to Equation 2.24 leads to

$$dI(\tau) = I(\tau)d\tau - J(\tau)d\tau. \tag{2.28}$$

The solution of Equation 2.28 can be found by recalling that the solution to the non-source term Beer-Lambert law was an exponential decay of transferred radiation with a linear increase in the distance the radiation travelled through the medium (Equation 2.16). Therefore, beginning with $I(\tau)e^{-\tau}$, taking the derivative,

$$\frac{d}{d\tau}(I(\tau)e^{-\tau}) = \left(\frac{dI(\tau)}{d\tau} - I(\tau)\right)e^{-\tau}, \tag{2.29}$$

and rearranging the result to isolate $\frac{dI(\tau)}{d\tau}$ results in an equation that can be substituted into Equation 2.28 as follows:

$$\begin{aligned} dI(\tau) &= I(\tau)d\tau - J(\tau)d\tau; \\ e^{\tau}\frac{d}{d\tau}(I(\tau)e^{-\tau}) + I(\tau) &= I(\tau) - J(\tau); \\ \text{and} \quad \frac{d}{d\tau}(I(\tau)e^{-\tau}) &= -J(\tau)e^{-\tau}. \end{aligned} \tag{2.30}$$

If a reference point is chosen such that the optical depth at that point is 0, then the radiance at any point in the atmosphere with optical depth τ as seen at the reference point is given by

$$\begin{aligned} \int_0^{\tau} d(I(\tau')e^{-\tau'}) &= -\int_0^{\tau} J(\tau')e^{-\tau'}d\tau'; \\ I(\tau)e^{-\tau} - I(0) &= -\int_0^{\tau} J(\tau')e^{-\tau'}d\tau'; \\ I(0) &= I(\tau)e^{-\tau} + \int_0^{\tau} J(\tau')e^{-\tau'}d\tau'. \end{aligned} \tag{2.31}$$

Converting back from τ to the regular path coordinates, one arrives at the commonly stated form of the radiative transfer equation,

$$I(0) = I(s)e^{-\tau(s)} + \int_s^0 J(s')k(s')e^{-\tau(s')}ds'. \tag{2.32}$$

Solving this equation is the essence of radiative transfer modelling. With the fundamentals of radiative transfer theory established, it is now appropriate to discuss how the SASKTRAN model solves Equation 2.32 to model the atmosphere as viewed by the OSIRIS instrument.

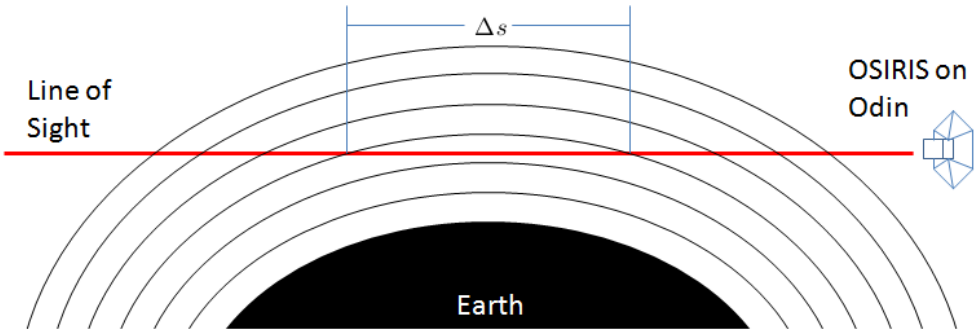

Figure 2.13: SASKTRAN models the atmosphere as a set of concentric spherical shells.

2.4.3 Solving the Radiative Transfer Equation with SASKTRAN

The equation of radiative transfer, displayed in its common form in Equation 2.32, allows the calculation of the radiance observed along path direction $\hat{\Omega}$ from a point s to the observation point. For the SASKTRAN radiative transfer model, the observation point is the OSIRIS instrument, and the radiance observed is the total light scattered by the atmosphere into the OSIRIS line of sight.

The SASKTRAN Atmosphere

In order to successfully model this configuration, the equation of radiative transfer must be solved for each point in the atmosphere along the OSIRIS line of sight. SASKTRAN models the atmosphere as a series of concentric spherical shells as shown in Figure 2.13. The shell radius is variable, but typically each shell has a radius 1000m greater than the shell below it, creating an atmosphere made up of spherical cells each with a thickness of 1000m. The first cell has its lower boundary directly on the ground (0 km altitude) while the last cell, which defines the edge of the SASKTRAN atmosphere, has its upper boundary at 100km altitude. The atmospheric properties of each spherical cell are considered to be homogeneous.

Path Length Approximation

When equations call for a line integral along a line of sight, the SASKTRAN model uses a numerical approximation that requires a finite step size, $ds \approx \Delta s$. The value of Δs for each

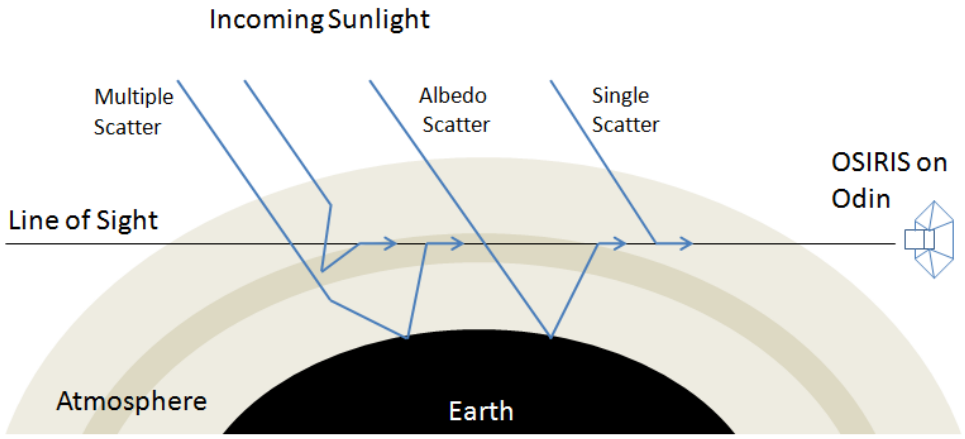

Figure 2.14: The different scattering events modelled by SASKTRAN.

atmospheric cell is the distance along the line of sight between the two boundaries of the cell as shown in Figure 2.13. Any integral between two points along a line of sight therefore reduces to a summation over all cells through which the line of sight passes. The equation for optical depth provides a convenient example,

$$\tau(s_2, s_1) = \int_{s1}^{s2} k(s)ds \approx \sum_{i=0}^{n} k_i \Delta s_i, \tag{2.33}$$

where n is the number of cell transitions that occur between points s_1 and s_2. For each cell the calculations are performed at a point whose altitude is halfway between the altitudes of the inner and outer shells.

Calculation of Radiance

When calculating the scattered radiance the SASKTRAN model examines three separate scattering situations: light that is scattered once, light that is scattered twice, and light that is scattered three or more times (*Bourassa et al.*, 2007), as shown in Figure 2.14. Each of these situations contains a unique atmospheric source term $J(s)$ and ground term $\tilde{I}(s)$. For this model, the observation point is defined as the location where $s = 0$ (which can be any point inside or outside of the SASKTRAN atmosphere), the direction of the line of sight is given by $\hat{\Omega}$ and points along the line of sight are denoted by s.

Single Scatter At OSIRIS wavelengths, nearly all light entering the atmosphere is solar radiation. For the purpose of this work solar radiation can be assumed to be collimated and unattenuated until it reaches the edge of Earth's atmosphere. When examining single scatter events, the assumption of collimated solar radiation simplifies the equation of the source term (Equation 2.25) as the integration over the entire solid angle is reduced to a delta function in the direction of the solar radiation. The assumption of solar radiation being unattenuated until interaction with the atmosphere allows for the attenuation from the sun to the point of interest s to be calculated as the attenuation from the top of the atmosphere to s. The result is that the single scatter source term $J_1(s, \hat{\Omega})$ at each point along the line of sight is found by attenuating the collimated solar radiation, $F(\hat{\Omega}')$, to the point of interest and scattering that attenuated light into the line of sight, or

$$J_1(s, \hat{\Omega}) = F(\hat{\Omega}')e^{-\tau(\text{sun},s)}\frac{k_{scatt}(s)}{k(s)}p(s, \Theta), \tag{2.34}$$

where Θ is the scattering angle between the propagation vectors of the incident and scattered rays.

The ground term $\tilde{I}_1(s_1)$ calculates the attenuation of radiation from a source at the end of the line of sight, s_1, to the point of observation. In the SASKTRAN geometry, the line of sight ends at either the top of the atmosphere or at the ground. When the line of sight ends at the top of the atmosphere there is no source to be found and the value of $\tilde{I}_1(s_1)$ is zero (SASKTRAN does not evaluate the case where the sun is at the end of the line of sight due to calculation complications discussed in *Bourassa et al.* (2007)). When the line of sight ends on the ground the component of solar radiation normal to the ground can be considered the F_{down} term of Equation 2.21 and the reflected radiance can be calculated by assuming a Lambertian scattering,

$$\tilde{I}_1(s_1) = \frac{a}{\pi}F(\hat{\Omega}')\cos(\theta')e^{-\tau(\text{sun},s_1)}, \tag{2.35}$$

where a is the albedo and θ' is the angle between the solar incident ray and ground normal, also known as the solar zenith angle. Equations 2.34 and 2.35 allow the total contribution of single scattered light (either atmospheric scattering or reflected off the Earth) to be calculated

for any line of sight originating at any observation point in, or outside of, the atmosphere. Written together, they form the single scatter term of the radiative transfer equation,

$$I_1(s) = \int_{s_1}^{0} J_1(s, \hat{\Omega}) k(s) e^{-\tau(s)} ds + \tilde{I}_1(s_1) e^{-\tau(s_1)}. \tag{2.36}$$

Light That is Scattered Twice Examining the second scattering of radiation naturally implies that the radiation has already been scattered once. Therefore, the source term for the second scattering event, $J_2(s)$, receives all of its incoming light from single scattered light described by Equation 2.36, incident on a point s in the atmosphere from all possible solid angles $\hat{\Omega}'$,

$$J_2(s, \hat{\Omega}) = \frac{k_{scatt}(s)}{k(s)} \int_{4\pi} I_1(s, \hat{\Omega}') p(s, \Theta) d\hat{\Omega}'. \tag{2.37}$$

The second scatter ground term is found in a similar manner, where the light incident on ground point s_1 is comprised of single scattered light coming from all upward directions. Integrating over the entire hemisphere of possible incoming solid angles yields the total radiance from ground reflection, or

$$\tilde{I}_2(s_1) = \frac{a}{\pi} \int_{2\pi} I_1(s_1, \hat{\Omega}') \cos(\theta') d\hat{\Omega}'. \tag{2.38}$$

The equation of radiative transfer for second scattering incident is then given by

$$I_2(s) = \int_{s_1}^{0} J_2(s, \hat{\Omega}) k(s) e^{-\tau(s)} ds + \tilde{I}_2(s_1) e^{-\tau(s_1)}. \tag{2.39}$$

Light Scattered Three or More Times Conceptually, light undergoing three or more scattering events is very similar to the case when light is scattered twice. As in the second order case, the source term for ith order scattered light, $J_i(s, \hat{\Omega})$, obtains all of its incoming light from light scattered $i-1$ times integrated over all possible incoming solid angles Ω'. As an equation this is given by

$$J_i(s, \hat{\Omega}) = \frac{k_{scatt}(s)}{k(s)} \int_{4\pi} I_{i-1}(s, \hat{\Omega}') p(s, \Theta) d\Omega'. \tag{2.40}$$

The ith order ground term is also similar, found by integrating over the entire hemisphere of possible incoming solid angles for light that has been scattered $i-1$ times, as seen in

$$\tilde{I}_i(s_1) = \frac{a}{\pi} \int_{2\pi} I_{i-1}(s_1, \hat{\Omega}') \cos(\theta') d\Omega'. \tag{2.41}$$

The total radiance is the sum of light scattered any number of times and is given by

$$\begin{aligned} I(s) = & \int_{s_1}^{0} \left(J_1(s, \hat{\Omega}) + J_2(s, \hat{\Omega}) + \sum_{i=3}^{\infty} J_i(s, \hat{\Omega}) \right) k(s) e^{-\tau(s)} ds \\ & + \left(\tilde{I}_1(s_1) + \tilde{I}_2(s_1) + \sum_{i=3}^{\infty} \tilde{I}_i(s_1) \right) e^{-\tau(s_1)}. \end{aligned} \tag{2.42}$$

When the position of OSIRIS in space is selected as the observation point, the result of solving this equation is a model of the atmosphere as seen by OSIRIS that compares extremely well with the actual OSIRIS measurements, as shown in Figure 2.15. Such a successful model can be used in tandem with OSIRIS measurements to retrieve vertical number density profiles of atmospheric constituents such as ozone.

2.5 Ozone Profile Retrieval Using SaskMART

The ability to model the atmosphere as seen from OSIRIS with the SASKTRAN radiative transfer model makes it possible for information about atmospheric constituents to be retrieved from OSIRIS data. Retrievals of trace gases are completed using SaskMART, a unique Multiplicative Algebraic Reconstruction Technique (MART) developed at the University of Saskatchewan and designed specifically for OSIRIS measurements. The goal of SaskMART is the same as all retrieval schemes, which is to infer a state vector x from a measurement vector $y(x)$. SaskMART has its roots in the Chahine non-linear relaxation retrieval technique (*Chahine*, 1972) which presents an equation,

$$x_i^{(n+1)} = x_i^{(n)} \frac{y_i^{obs}}{y_i^{mod}}, \tag{2.43}$$

for iteratively determining the value of state vector x at an altitude i. Within Equation 2.43, n represents the value of the current iteration. The values y_i^{obs} and y_i^{mod} are measurement

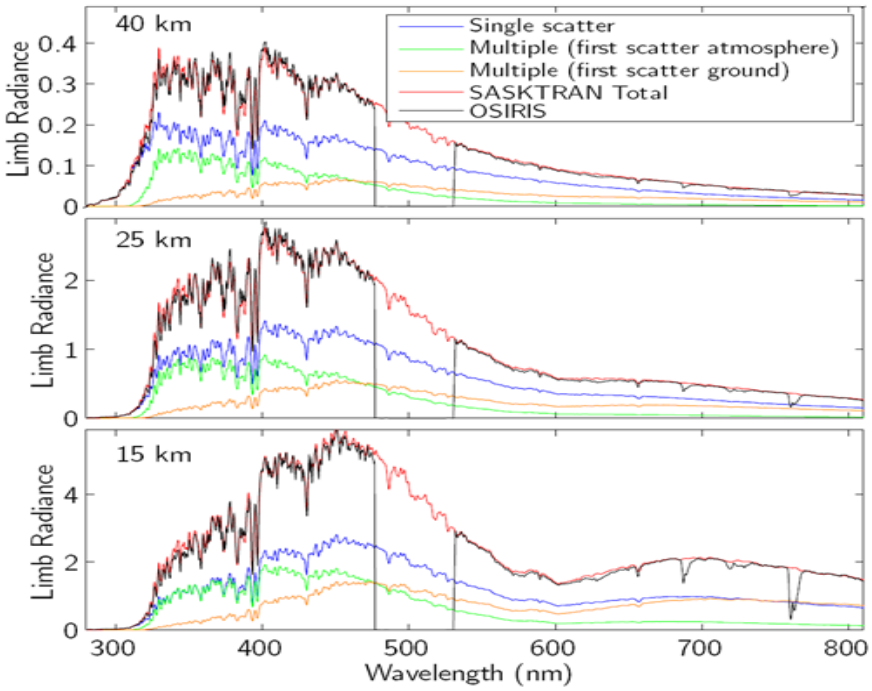

Figure 2.15: Sample result of the SASKTRAN radiative transfer model alongside OSIRIS measurements (*Bourassa et al.*, 2007).

vectors; y_i^{obs} is derived directly from OSIRIS measurements while y_i^{mod} is derived from the results of the nth iteration of the SASKTRAN radiative transfer model. The formation of these measurement vectors is essential to the proper retrieval of ozone profiles from OSIRIS measurements and as such deserves to be discussed in greater detail.

2.5.1 Ozone Measurement Vector Formation

In a method similar to that of *Flittner et al.* (2000), measurement vectors for the retrieval of ozone are formed using limb radiance profiles of wavelengths efficiently absorbed by ozone, examples of which are shown in Figure 2.16. Ozone is typically present in the atmosphere at altitudes ranging the lower limit of OSIRIS observations up to approximately 70 km and as such measurement vectors must be determined for all altitudes within this range. The probability of an incoming photon being absorbed by an ozone molecule is defined by the ozone cross section, shown in Figure 2.17 with three key wavelength bands of ozone absorption, the Hartley, Huggins, and Chappuis bands, labelled for reference.

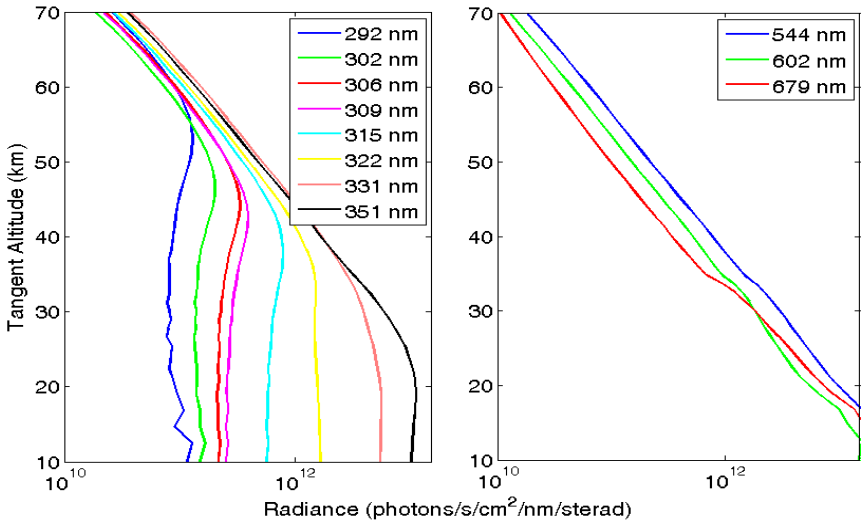

Figure 2.16: Limb radiance profiles from the Hartley and Huggins bands (left) and Chappuis band (right).

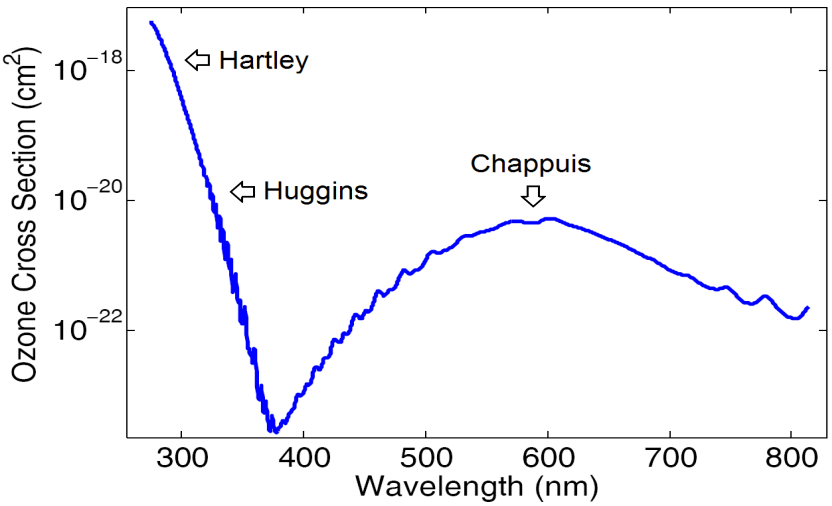

Figure 2.17: The ozone cross section in the OSIRIS wavelength range. The cross section displayed here was produced by *Bogumil et al.* (2003).

In the Hartley and Huggins bands absorption by ozone is so efficient that the atmosphere becomes optically thick in the stratosphere, with the knee (the altitude in the limb radiance profiles of Figure 2.16 where the radiance stops increasing with decreasing altitude) ranging from approximately 50 km for 310 nm to 20 km for 330 nm. As information cannot be retrieved from tangent altitudes below the knee Hartley and Huggins band wavelengths can only be used to generate measurement vectors for the middle to upper stratosphere. As first discussed in *Degenstein et al.* (2009), each middle or upper stratospheric measurement vector is formed from a pair of radiance profiles and is defined as the difference between the logarithm of a normalized profile element from a non-absorbing reference wavelength, $\tilde{I}(j, \lambda_{ref})$, and a normalized profile element from a wavelength where ozone absorption is significant, $\tilde{I}(j, \lambda_{abs})$. As an equation the measurement vector is given as,

$$y_{jk} = \ln\left(\frac{\tilde{I}(j, \lambda_{ref})}{\tilde{I}(j, \lambda_{abs})}\right), \tag{2.44}$$

where $\tilde{I}$ represents a normalized radiance profile, j denotes the measured tangent altitude, and k is an index term which identifies the measurement vector. For example, the left panel of Figure 2.16 shows radiance profiles of the seven ozone absorbing wavelengths that are typically used in stratospheric ozone retrievals along with the profile of the standard non-absorbing reference wavelength, 351 nm. One unique measurement vector can be formed from each absorbing wavelength profile, with each measurement vector being identified by a value of k that will range from 0 to 6.

Ozone does not absorb as efficiently in the Chappuis band and as such the atmosphere does not become optically thick at these wavelengths even at the lowest viewing altitude of OSIRIS. Radiance profiles from the Chappuis band are therefore used to form measurement vectors for lower stratospheric and tropospheric ozone. The equation for Chappuis band measurement vectors is given as

$$y_{jk} = \ln\left(\frac{\sqrt{\tilde{I}(j, \lambda_{ref_1})\tilde{I}(j, \lambda_{ref_2})}}{\tilde{I}(j, \lambda_{abs})}\right), \tag{2.45}$$

where the absorbing wavelength is typically around 600 nm, and the two non-absorbing reference wavelengths are taken from opposite ends of the Chappuis band where ozone ab-

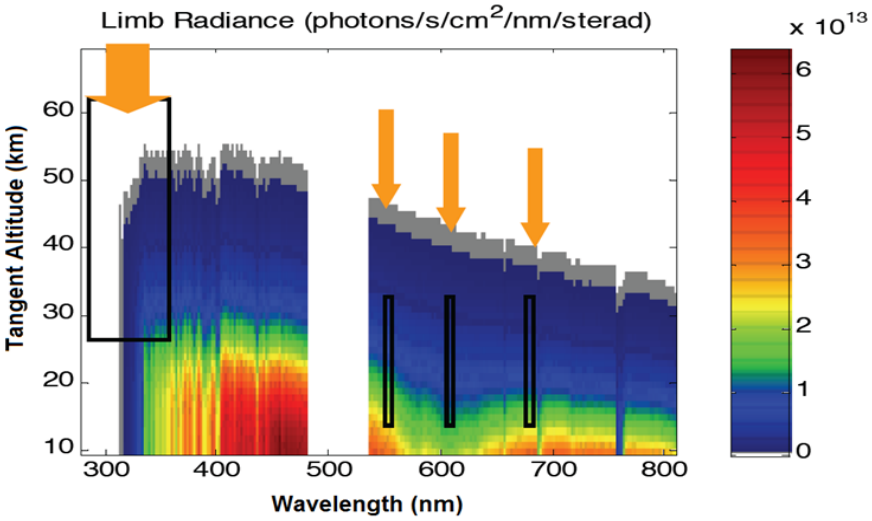

Figure 2.18: Limb radiance observed by OSIRIS. Boxed areas are used for ozone profile retrieval.

sorption is insignificant (*Degenstein et al.*, 2009). As Equation 2.45 requires three separate wavelength measurements, the resultant measurement vectors are often called triplet measurement vectors. A visual summary of which wavelengths and altitudes are used to form these measurement vectors is given in Figure 2.18.

Equations 2.44 and 2.45 require that both the absorbing and reference wavelength measurements be normalized to a reference tangent altitude. The normalization altitude must be chosen such that the signal is large enough to maintain an acceptable signal-to-noise ratio, yet chosen at a high enough altitude to avoid significant ozone absorption. In the Chappuis band these conditions are met at 33 km, thus all Chappuis band radiance profiles are normalized at that altitude (*Degenstein et al.*, 2009). In the Hartley and Huggins bands, the wide range of ozone absorption efficiency necessitates determining the normalization altitude separately for each absorbing wavelength. *Degenstein et al.* (2009) developed a method of normalizing each pair of radiance profiles such that the maximum value of the resultant measurement vector, which occurs at the minimum altitude, is approximately unity as shown in Figure 2.19. As a result of this method, normalization altitudes in the Hartley and Huggins bands typically range from 40 to 65 km tangent altitude.

With the measurement vectors defined it is now appropriate to introduce the SaskMART

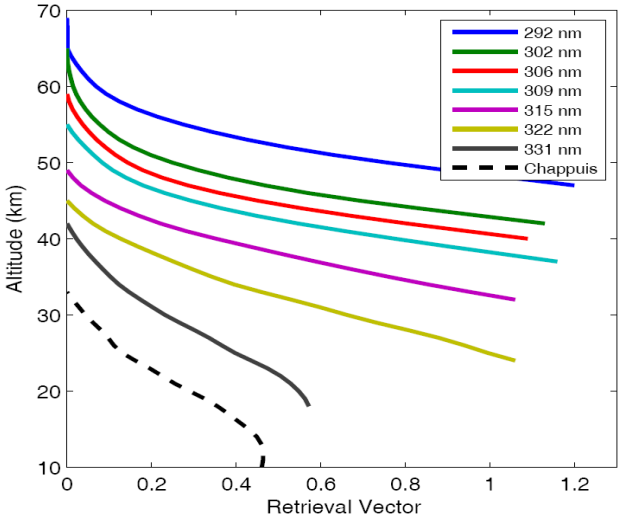

Figure 2.19: OSIRIS measurement vectors used in ozone retrieval (*Degenstein et al.*, 2009).

.

equation, seen in various previous works (*Degenstein et al.*, 2003, 2004; *Bourassa et al.*, 2007; *Roth et al.*, 2007; *Degenstein et al.*, 2009) and given as,

$$x_i^{(n+1)} = x_i^{(n)} \sum_k \left(\sum_j \left(\frac{y_{kj}^{obs}}{y_{kj}^{mod}} W_{kji} \right) \right), \tag{2.46}$$

where $x_i^{(n)}$ is the atmospheric constituent whose vertical profile is to be retrieved which for this thesis shall be limited to ozone. Once again, the altitudes of the retrieved profile are represented by i, while j represents a tangent altitude element of the kth pair/triplet measurement vector. As the different measurement vectors have varying levels of importance for different profile elements, the term W_{kji} is included as a weighting factor to ensure that only measurement vectors applicable to the profile element in question have non-zero values. The sum over all the weighting factors at each altitude i is unity.

The importance of a measurement vector to a certain profile element and the corresponding value of the weighting factor, W_{kji}, is determined by two factors: the tangent altitude of the element and the wavelengths of the radiance pair/triplet used to create the measurement vector. Following the method discussed in *Roth et al.* (2007), the tangent altitude and pair/triplet weighting factors can be discussed independently, with the SaskMART equation

taking on the following form,

$$x_i^{(n+1)} = x_i^{(n)} \sum_k \left(W_{ki} \sum_j \left(\frac{y_{kj}^{obs}}{y_{kj}^{mod}} W_{ji} \right) \right). \tag{2.47}$$

The W_{ki} term signifies the importance of a particular pair/triplet combination, k, to the retrieved profile element at altitude i, while the W_{ji} term relates the importance of the tangent altitude j for all measurement vectors to the retrieved profile at altitude i. Once again, summations over k of W_{ki} and over j of W_{ji} both result in unity. Discussing the two weighting terms independently allows for a better understanding of how the SaskMART equation combines multiple lines of sight and pair/triplet combinations to arrive at a single retrieved profile element.

2.5.2 Line of Sight Combination & Weighting

As discussed in previous works regarding the SaskMART equation (*Roth et al.*, 2007; *Degenstein et al.*, 2009), the developers of the SaskMART equation found that retrievals at any altitude can be accomplished using three successively lower tangent altitude lines of sight. Their approach, which is followed in this thesis, stipulates that all elements of W_{ji} in Equation 2.47 are zero unless the line of sight j occurs at tangent altitude i or the next two successively lower tangent altitudes. As first shown in *Roth et al.* (2007), the weights of the non-zero elements are assigned as: $W_{j,j} = 0.6$, $W_{j-1,j} = 0.3$, and $W_{j-2,j} = 0.1$.

2.5.3 Pair/Triplet Combination & Weighting

Following the convention of *Degenstein et al.* (2009), for each measurement vector formed from a Hartley or Huggins band pair the minimum non-zero altitude of W_{ki} in Equation 2.47 is taken as the altitude of the knee in the absorbing wavelength's radiance profile. Due to the lack of a knee above 10 km in Chappuis band measurements, the minimum non-zero altitude of triplets is set to be 10 km, the typical lower retrieval boundary of OSIRIS.

The maximum non-zero altitude of W_{ki} for each pair/triplet is conventionally chosen to be 5 km below the normalization altitude. Avoiding the use of pair/triplet elements near the normalization altitude is vital as Equations 2.44 and 2.45 approach zero at the normalization

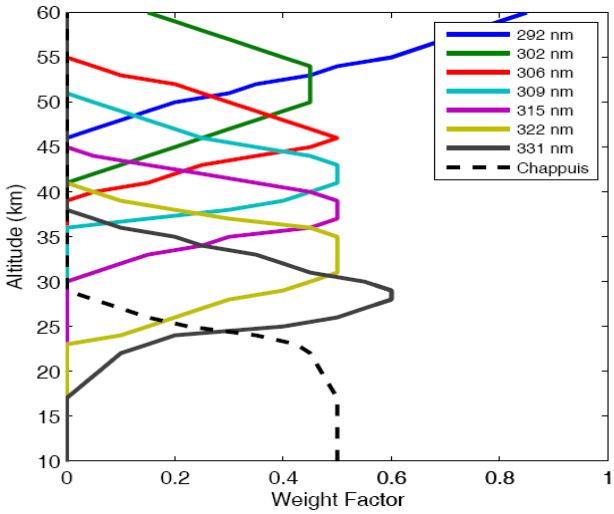

Figure 2.20: Sample W_{ki} weighting factors as a function of altitude for each of the measurement vectors (*Degenstein et al.*, 2009).

altitude. Remaining below the normalization altitude also eliminates the concern of dividing by two small numbers, a situation which can result in the measurement noise becoming more prominent (*Degenstein et al.*, 2009).

Degenstein et al. (2009) found that for successful ozone retrieval at each altitude i, the sum of the weighting factors, W_{ki} over all k elements must equal unity. They also found that the contribution of each pair/triplet as a function of altitude must be increased and decreased slowly to avoid oscillatory structure in the retrieved profile. With these constraints they developed a method, which is followed in this thesis, where the weighting factor for each pair/triplet begins at zero for the minimum altitude, gradually increases until the altitude where it has the most significance for the retrieval is reached, and then gradually returns to zero at the maximum altitude. Samples of weighting factors that fit these constraints are shown in Figure 2.20.

2.5.4 Implementation

To retrieve the ozone profile, a SASKTRAN model of the atmosphere is generated with an initial estimate of the ozone profile, x_i^0, as one of the inputs. The modelled measurement vectors, y_{kj}^{mod} of Equation 2.46, are then calculated from this model. These modelled

measurement vectors are then used with the measurement vectors created from the OSIRIS measurement, y_{kj}^{obs}, and summed over all altitudes and measurement vectors to produce an updating vector α_i, as shown in Equation 2.48,

$$\alpha_i = \sum_k \left(\sum_j \left(\frac{y_{kj}^{obs}}{y_{kj}^{mod}} W_{kji} \right) \right) = \sum_k \left(W_{ki} \sum_j \left(\frac{y_{kj}^{obs}}{y_{kj}^{mod}} W_{ji} \right) \right), \tag{2.48}$$

where i once again represents the altitude of each element. The ozone profile used in creating the SASKTRAN model is then multiplied by this updating vector,

$$x_i^{(n+1)} = x_i^{(n)} \alpha_i, \tag{2.49}$$

to produce an updated ozone profile. A new SASKTRAN model is then calculated with the updated ozone profile, and the process repeats itself until the value of α_i converges to a value close to unity at all altitudes or the maximum number of iterations is reached.

2.5.5 Verification of OSIRIS Ozone Retrievals

The OSIRIS instrument is far from the only satellite instrument capable of retrieving vertical profiles of atmospheric ozone. Instruments such as the Atmospheric Chemistry Experiment (ACE) (*Bernath et al.*, 2005), the Scanning Imaging Absorption Spectrometer for Atmospheric Chartography (SCIAMACHY) (*Bovensmann et al.*, 1999), and the Stratospheric Aerosol and Gas Experiment (SAGE) series (*McCormick*, 1987; *Thomason and Taha*, 2003) have all been in operation during the lifetime of OSIRIS and are capable of measuring atmospheric ozone profiles with spatial resolution similar to those of OSIRIS. The ozone profiles produced by SAGE II, an occultation instrument active from 1984–2006 (*McCormick et al.*, 1979), are considered the standard against which all other ozone profiles are compared.

To evaluate whether the SaskMART inversion method produced acceptable results, OSIRIS ozone profiles retrieved with SaskMART were compared against profiles retrieved from SAGE II measurements. The four year overlap between the OSIRIS and SAGE II missions provided 1591 instances where measurements from both satellites were within 1000 km, one degree latitude, and 24 hours of each other. Four examples of the compared profiles are given in Figure 2.21, which show that the OSIRIS ozone profiles compare favourably with the SAGE

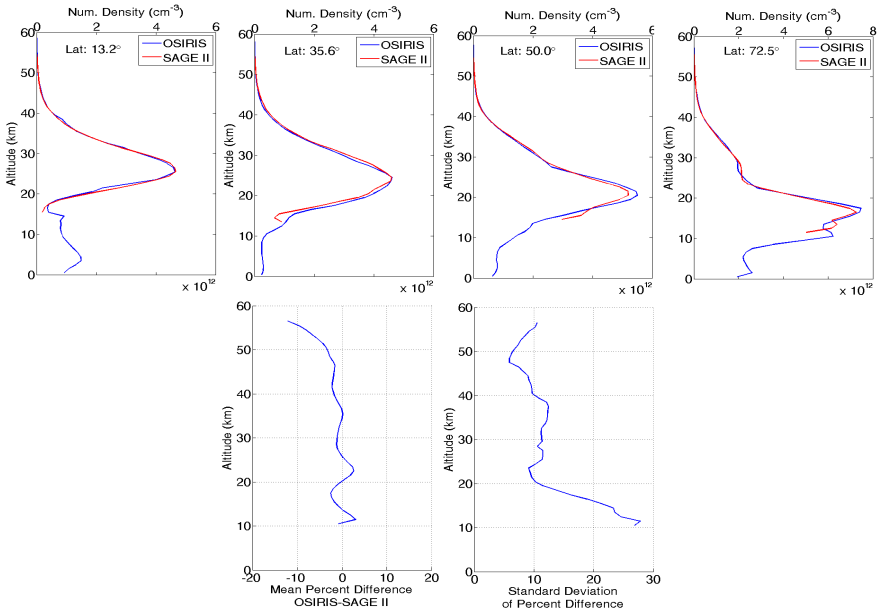

Figure 2.21: OSIRIS and SAGE II comparisons. The top four plots show typical ozone retrievals over various latitudes. The bottom two plots were formed using all 1591 coinciding measurements.

II profiles. An evaluation of all comparable ozone profiles revealed a mean percent difference of less than 3% from 18–50 km with a standard deviation of approximately 10% from 20–50 km as shown in the bottom plots of Figure 2.21. The low values of the mean percent difference profile indicate minimal systematic differences between the two datasets, while the low standard deviation values show that random variation between the datasets is also nominal. It should be noted that *Degenstein et al.* (2009) performed a similar comparison of retrieved ozone profiles where OSIRIS and SAGE II measurements were only considered coincident if within 200 km and two hours of each other. 196 coincident measurements were found using their narrower criteria, resulting in a mean percent difference of less than 2% with a standard deviation of approximately 5% from 18–50 km (*Degenstein et al.*, 2009).

The use of a broader coincidence criteria than *Degenstein et al.* (2009) naturally increases the discrepancy between OSIRIS and SAGE II ozone profiles, but the larger sample size allows for profile comparisons of unique subsets of the measurements. For example, it becomes possible to compare only tropical latitude ozone profiles, or compare only the profiles from a certain time period, and still have enough data to make reasonable conclusions. The ability

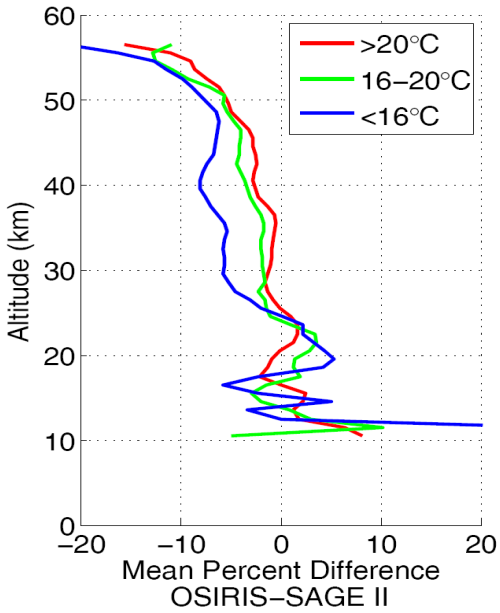

Figure 2.22: Mean percent difference between OSIRIS and SAGE II ozone profiles. Three different OSIRIS optics temperature ranges are represented.

to examine these different subsets makes it possible to determine if the discrepancies between OSIRIS and SAGE II ozone profiles are constant over time or if certain OSIRIS measurement conditions impact the retrieved profiles and negatively affect the comparisons.

It was found that one subset of measurements did show an increase in the mean percent difference between OSIRIS and SAGE II ozone profiles. Figure 2.22 shows that when the OSIRIS instrument undergoes a decrease in optics temperature the mean percent difference between OSIRIS and SAGE II profiles increases. The mean percent difference between 25 and 48 km remains below 2% when the OSIRIS optics temperature is above 20°C, but when the optics temperature falls below 16°C (a situation that occurred for 15.7% of coincident measurements) the absolute mean percent difference rises above 5% for altitudes greater than 27 km. Such a change in value is large enough to suggest that decreases in OSIRIS optics temperature introduce a change in the OSIRIS measurements that is not compensated for when modelling the atmosphere as observed by OSIRIS, leading to systematic errors in the retrieved ozone profiles.

The simplest and most likely cause of the change in OSIRIS measurements is thermal expansions and contractions altering the orientation of components within the spectrograph

which in turn alters the final dispersion pattern of light recorded by the CCD. As will be discussed in great detail later, the dispersion of light on the OSIRIS CCD is represented by the OSIRIS spectral point spread function, an array of values that describes the dispersion observed at every OSIRIS wavelength; it is essentially the impulse response of the spectrograph. Currently, the spectral point spread function used in calibration is time-independent, making it impossible for changes in light dispersion within OSIRIS to be accounted for when calculating the radiance seen by OSIRIS from the results of the SASKTRAN radiative transfer model. The majority of work in this thesis focuses on developing a time-dependent spectral point spread function in order to eliminate the suspected systematic errors and improve upon the ozone profiles retrieved from OSIRIS measurements. However, the impact of a time-dependent OSIRIS spectral point spread function may go beyond improvements to ozone profile retrieval. Currently, published ozone cross sections are being evaluated by atmospheric experts worldwide with the hope of defining a standard. The OSIRIS team is part of this evaluation, but initial analysis has revealed that a time-dependent OSIRIS spectral point spread function may be necessary before any results can be produced.

2.6 Ozone Cross Sections

Many of the calculations that occur in the SASKTRAN model call for a constituent cross section that describes the probability of interaction between two particles as a function of several variables including wavelength, temperature, and pressure. The cross section of interest to this thesis is the ozone absorption cross section, which gives the probability of an ozone molecule absorbing an incident photon as a function of wavelength. Recently, the international standards of the ozone cross section have been called into question, prompting a Commission that has the potential to impact the ozone cross section used within SASKTRAN and by extension the profiles of ozone retrieved from OSIRIS measurements.

2.6.1 The ACSO Commission

The ozone cross sections published by *Bass and Paur* (1985) are currently considered the standard ozone absorption cross sections by the World Meteorological Organization (WMO).

These cross sections cover a wavelength range of 245–340 nm (the Hartley and Huggins bands) for temperatures of 203, 218, 243, 273, and 298 K. The data is presented in wavelength steps of 0.05 nm with a spectral resolution of less than 0.025 nm Full Width at Half Maximum (FWHM) (*Bass and Paur*, 1985). However, the Bass and Paur cross sections have been surpassed in both wavelength range and resolution by multiple more recently published cross sections. Many researchers around the world therefore employ different cross sections in their retrieval algorithms, a situation that can lead to systematic errors when comparing ozone profiles retrieved from different instruments. In response, the WMO has recently launched the Absorption Cross Sections of Ozone (ACSO) Commission to evaluate all available ozone cross sections. The specific goals of the Commission are listed on the website http://igaco-o3.fmi.fi/ACSO/index.html and provided here for convenience:

- Review the presently available ozone absorption cross sections. Priority on Huggins band.

- Determine the impact of changing the reference ozone absorption cross section for all of the commonly used (both ground-based and satellite) atmospheric ozone monitoring instruments.

- Recommend whether a change needs to be made to the presently used World Meteorological Organization standard ozone absorption cross section data published by *Bass and Paur* (1985).

OSIRIS ozone profiles are in good agreement with other ozone monitoring instruments and provide over a decade of global ozone data, making them highly esteemed within the atmospheric community. The OSIRIS team has therefore been tasked with evaluating the three goals of the ACSO Commission with regards to the OSIRIS instrument, in particular to determine the impact that changing the ozone absorption cross section used in the retrieval process has on the retrieved ozone profiles.

2.6.2 ACSO Cross Sections

The ACSO Commission provided six cross sections for researchers to evaluate, but two have emerged as frontrunners to become the new standard. To simplify the work of this thesis, only these two cross sections, along with the current OSIRIS cross section, will be evaluated.

SCIAMACHY

The ozone cross section currently used within the SASKTRAN model is an old version of the cross section produced from measurements made with the SCIAMACHY instrument (*Bogumil et al.*, 2003). These cross sections cover a wavelength range of 230–1070 nm at temperatures of 203, 223, 243, 273, and 293 K. Both the data format and spectral resolution vary with wavelength, with the data being presented in wavelength steps of 0.14–0.20 nm, while the resolution varies between 0.24 and 0.48 nm at FWHM (*Bogumil et al.*, 2003). The uncertainty in the cross section is listed as 3.1% (*Orphal*, 2003). The history of the cross section currently used by OSIRIS is uncertain, but it has proven to produce successful retrievals of ozone from OSIRIS measurements and as such it remains the default cross section used within the SASKTRAN model.

Daumont, Brion & Malicet

Multiple papers have been published by the researchers Daumont, Brion, and Malicet regarding various wavelength regions of the ozone absorption cross section and its dependence on temperature (*Daumont et al.*, 1992; *Brion et al.*, 1993; *Malicet et al.*, 1995; *Brion et al.*, 1998). The result of this work is a set of ozone absorption cross sections, collectively called the DBM cross section, that range from 195–830 nm (which covers the entire OSIRIS spectrum) for temperatures of 218, 228, 243, 273, and 295 K. Wavelength steps of 0.01 nm are used to present the data, which has a spectral resolution of 0.01 nm at FWHM for wavelengths of 195–345 nm and 0.02 nm at FWHM for wavelengths of 345–830 nm (*Orphal*, 2003). The uncertainty in cross section measurements varies between 1.3–2.5% (*Orphal*, 2003).

Serdyuchenko

The cross sections produced by a group of researchers led by Anna Serdyuchenko are the most recently produced ACSO cross sections, having been successfully measured and presented but not yet published at the time of this writing. These cross sections cover a wavelength range of 213–1100 nm in 0.01 nm increments at a spectral resolution of 0.02 nm for temperatures ranging from 193 K to 293 K in 10 K steps. The eleven temperature measurements are a substantial increase over all other ACSO cross sections and provide a substantial advantage as the ozone cross section varies significantly with temperature (*Bass and Paur*, 1985). The total relative systematic uncertainty has been given as less than 3%.

2.6.3 Cross Section Impact on OSIRIS Ozone Retrievals

A requirement of the SASKTRAN model is that any constituent cross section being implemented into the model must be at the resolution of the OSIRIS spectrograph. The ozone cross sections of the ACSO Commission were all calculated from measurements made with unique instruments, and thus are presented at their own unique resolutions. The process of bringing these cross sections to OSIRIS resolution involves two steps, the first being a convolution to smooth the high resolution features of the cross section not discernible at OSIRIS resolution while the second is an interpolation of the convolved cross section to OSIRIS wavelengths. For cross sections of extremely high resolution, the smoothing step is completed via convolution with the OSIRIS spectral point spread function.

In order to evaluate the impact that the DBM and Serdyuchenko ozone cross sections have on retrieved OSIRIS ozone profiles, it is necessary to implement each of them into the SASKTRAN model in place of the default SCIAMACHY cross section. Within the model the cross sections are convolved with the OSIRIS spectral point spread function, which is currently time-independent and unable to account for changes in light dispersion within the OSIRIS spectrograph. Plots (a) and (b) of Figure 2.23 highlight the potential problem. Plot (a) shows the DBM cross section after convolution with different Gaussian curves representative of the OSIRIS spectral point spread function, making it clear that convolving the cross section with different Gaussian curves produces different results in the

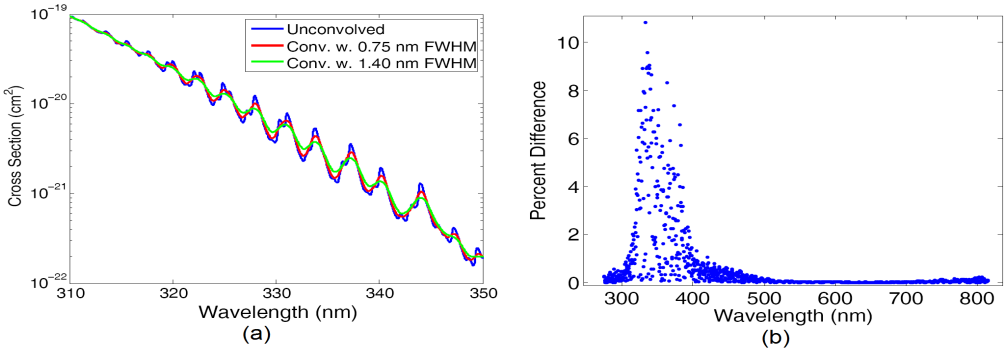

Figure 2.23: a) The Huggins band of the DBM cross section before and after convolution with Gaussian curves of various widths, showing the effects of convolving the cross section with different point spread functions. b) The percent difference between DBM cross sections convolved with 0.75 and 1.40 nm FWHM Gaussian curves.

Hartley and Huggins bands wavelengths. Plot (b) displays the percent difference between the two convolved cross sections of Plot (a) as a function of wavelength, indicating that the ozone cross section is only sensitive to convolution with different point spread functions for wavelengths of 300–400 nm. It can therefore be concluded that convolving the ozone cross section with an incorrect spectral point spread function will introduce systematic errors in the convolved cross section from 300 to 400 nm. Recall from Section 2.5 that almost all wavelengths necessary for stratospheric ozone retrieval are contained within 300–350 nm. Thus as long as the time-independent spectral point spread function is employed it will be impossible to evaluate the impact of the different cross sections as any changes in retrieved OSIRIS ozone profiles could be attributed to one of two situations. Either the changes are the result of the unwanted systematic errors introduced by the convolution of the ozone cross section with the time-independent spectral point spread function, or the changes are actually being introduced by the use of a different ozone cross section.

As an example of this predicament, consider Figure 2.24, which displays the mean and standard deviation of the percent difference for 196 coincident OSIRIS and SAGE II ozone profiles as a function of tangent altitude. The OSIRIS profiles were retrieved using the time-independent spectral point spread function and either the DBM, Serdyuchenko, or default SCIAMACHY cross sections. There is a clear discrepancy between 25 and 40 km, with profiles retrieved using the DBM or Serdyuchenko cross sections showing an absolute mean

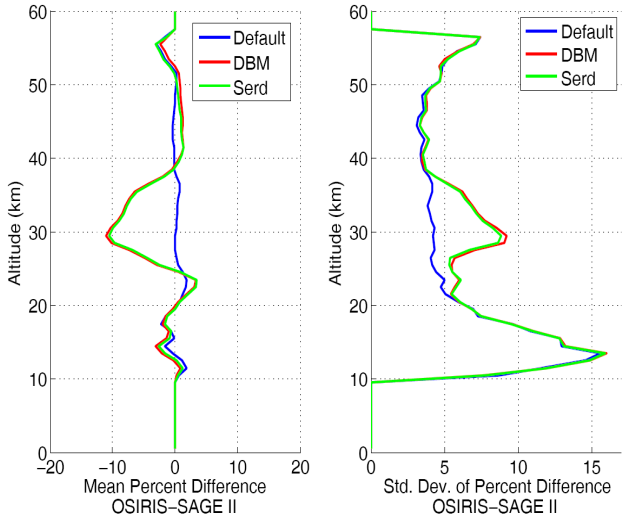

Figure 2.24: Mean and standard deviation of the percent difference between 196 OSIRIS and SAGE II ozone profiles. OSIRIS profiles retrieved with time-independent spectral point spread function and ozone cross section specified.

percent difference that peaks at 10%. Given the quality of all cross sections involved, it seems unlikely that the choice of cross section alone should impact the retrieved profiles by such a large amount. The altitudes of the discrepancy also suggest the presence of systematic errors caused by an incorrect spectral point spread function. Recall from Section 2.5 that the retrieval of ozone number densities from 25–40 km is heavily impacted by limb radiance profiles with wavelengths of 320–330 nm. Within the ozone cross section this wavelength range is comparatively more sensitive to convolution with an incorrect point spread function than the wavelength ranges used for upper stratospheric or tropospheric ozone retrievals (see Figure 2.23), suggesting an incorrect spectral point spread function is at least partly to blame. Thus in order to evaluate the impact of different ozone cross sections on OSIRIS ozone retrievals as requested by the ACSO Commission, it will first be necessary to develop a time-dependent spectral point spread function to eliminate systematic errors that prevent the required analysis.

A Note on the Application of the OSIRIS Spectral Point Spread Function Within SASKTRAN

The SASKTRAN radiative transfer model is, at its core, a tool used to model the path of light through Earth's atmosphere. In order to model the atmosphere as seen by OSIRIS in a reasonable amount of time SASKTRAN makes several assumptions regarding the atmosphere, its constituents, and how they interact with radiation. An assumption critical to this thesis is where the OSIRIS spectral point spread function is implemented within the SASKTRAN model. Ideally, radiative transfer models should be completed at high resolution, modelling as many wavelengths as possible to ensure the most detailed model achievable. Once all modelling has been completed the high resolution results should then be convolved with the instrument spectral point spread function and interpolated to the instrument resolution in order to model the atmosphere as seen by the instrument. SASKTRAN makes the assumption that this sequence can be reversed without significant impact. All constituent cross sections, including ozone, are first brought to OSIRIS resolution via convolution after which SASKTRAN models the atmosphere only at the 1353 wavelengths of OSIRIS. The reason for this assumption is computational time management. It is simply not feasible with today's technology to complete a fully spherical multiple scatter radiative transfer model for more than a few thousand wavelengths in a reasonable amount of time. The success of the SASKTRAN model, discussed in detail in *Bourassa et al.* (2007), provides justification for this computational time saving assumption.

Implementing the OSIRIS spectral point spread function before the modelling occurs, while acceptable in the SASKTRAN model, introduces a subtle issue that must be addressed. The cross sections used in the model must be brought to the resolution of the OSIRIS instrument, a task which is normally completed via convolution with the OSIRIS spectral point spread function. However, the resulting convolved cross sections will only be at OSIRIS resolution if the initial cross sections are at infinitely narrow resolution, an impossible situation given that all cross sections are calculated from measurements made by instruments of finite resolution. At every wavelength the actual resolution of the convolved cross section, σ_f, will be a convolution of the OSIRIS and measuring instrument point spread functions, shown

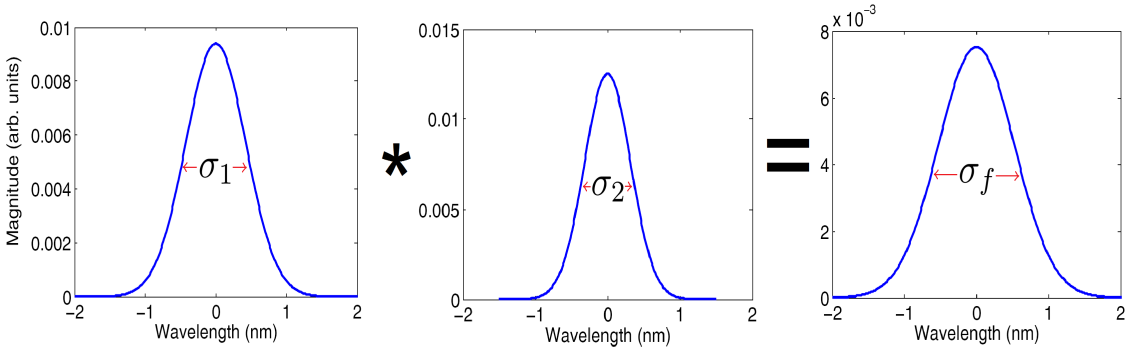

Figure 2.25: Convolving two Gaussian point spread functions of resolutions σ_1 and σ_2 yields a Gaussian curve of resolution σ_f.

as σ_1 and σ_2 in Figure 2.25. Assuming that the measuring instrument and OSIRIS point spread functions are Gaussian curves, the resulting resolution σ_f for a single wavelength will be given by,

$$\sigma_f = \sqrt{\sigma_1^2 + \sigma_2^2}. \tag{2.50}$$

Thus convolving a cross section with the OSIRIS spectral point function will never result in a convolved cross section at the resolution of OSIRIS. However, it is possible to make use of Equation 2.50 and treat the OSIRIS spectral point spread function as the desired final resolution σ_f. If the point spread function of the cross section measurement device is known, it becomes possible to calculate σ_{conv}, the width of the curve necessary to bring the cross section to OSIRIS resolution by means of the equation

$$\sigma_{conv} = \sqrt{\sigma_{osi}^2 - \sigma_{meas}^2}, \tag{2.51}$$

where σ_{osi} and σ_{meas} are the point spread functions of OSIRIS and ozone measurement instrument respectively.

The fact that the cross sections used in the SASKTRAN model must be convolved with something other than the OSIRIS spectral point spread function is subtle, but it is also essential to the success of the SASKTRAN model. Certain wavelengths in the Hartley and Huggins bands of the ozone cross section exhibit significant structure and are extremely sensitive to the width of the Gaussian curve used in the convolution. Failing to account

for the point spread function of the cross section measurement device and convolving the cross section with the OSIRIS spectral point function would create incorrect convolved cross sections in these bands, introducing significant errors into the SASKTRAN model and the atmospheric ozone profiles retrieved from it. Fortunately, the SASKTRAN model accounts for this subtle issue, ensuring that it is successfully able to model the OSIRIS view of the atmosphere. Any convolutions performed in this thesis will account for this issue when necessary, but for the sake of simplicity it will not be mentioned unless it is deemed prudent to do so.

2.7 Summary

The OSIRIS optical spectrograph onboard the Odin spacecraft takes continual measurements of the atmospheric limb. When used alongside the SASKTRAN radiative transfer model and SaskMART iterative retrieval algorithm these measurements can be used to generate vertical number density profiles of atmospheric ozone. There is reasonable cause to suspect that temperature fluctuations within the OSIRIS instrument are altering the path of light through the instrument and impacting its measurements. These alterations are not accounted for when modelling the atmosphere as seen by OSIRIS and lead to systematic errors in the retrieved OSIRIS ozone profiles. The development of a time-dependent spectral point spread function should eliminate these systematic errors and improve the quality of the retrieved profiles. A time-dependent spectral point spread function will also make it possible to evaluate the impact of different ozone cross section used within the SASKTRAN model, an analysis that has been requested by the ACSO Commission in the hopes of standardizing the ozone cross section used for atmospheric ozone retrievals.

Chapter 3

The OSIRIS Spectral Point Spread Function

The spectral point spread function of an optical instrument provides a wavelength-dependent representation of the final dispersion pattern observed after light has passed through the instrument. The OSIRIS spectral point spread function currently used to bring datasets to OSIRIS resolution does not vary with time, a situation that introduces systematic errors into OSIRIS ozone retrievals. In order to eliminate these errors it is necessary to develop a method for calculating a time-dependent OSIRIS spectral point spread function in the 310–350 nm wavelength range.

3.1 The Current State of the OSIRIS Spectrograph Spectral Point Spread Function

No imaging system is capable of forming a perfect image. The limitations of human ability make it impossible to design and craft a system that perfectly delivers the results predicted by theories and equations; there will always be a small but finite amount of image blurring in even the best instruments. Understanding what blurring to expect from a system is therefore imperative for the analysis of the images it produces. It is common practice to quantify the blurring produced by an optical system by passing a point source of light through the system. The measured response of the system to a point source reveals what image blurring the system causes and is known as the system's point spread function. As different wavelengths of light often interact with optical systems in different ways, instruments that measure spectrally dispersed light have unique point spread functions for every measurable wavelength. The set of unique-wavelength point spread functions are collectively known as the spectral point

spread function of the instrument. The OSIRIS optical spectrograph disperses light in the 280–810 nm wavelength band across 1353 pixels of its CCD detector, yielding 1353 nearly monochromatic measurements and an equal number of unique point spread functions which make up its spectral point spread function.

3.1.1 Assumption of a One Dimensional Spectral Point Spread Function

The point spread function of nearly all imaging systems is two dimensional due to the fact that the created image is projected onto a two dimensional recording surface. In the case of the OSIRIS optical spectrograph it is justifiable to reduce the point spread function to one dimension by assuming the blurring of light in one direction of the recording surface is negligible. The reasoning behind this assumption stems from the fact that the 1 km vertical by 40 km horizontal portion of the atmosphere seen by the imaging slit can be considered homogeneous. The 1 km vertical component of what is seen by the imaging slit is dispersed by the diffraction grating while the 40 km horizontal component remains unaltered. Thus when the final image of the diffracted imaging slit is projected onto the CCD the pixels used to record the 40 km horizontal component of each wavelength receive nearly uniform, nearly monochromatic light, a situation that effectively eliminates any signatures of horizontal blurring. Moreover, the measurements from these individual pixels are binned together to increase the signal-to-noise ratio of OSIRIS measurements so any horizontal spreading of light is effectively averaged out. For these reasons it is reasonable to state that there will only be significant spreading of light in the diffracted direction of the OSIRIS measurement, and therefore the reduction of the OSIRIS spectral point spread function to one dimension is justified.

3.1.2 Sources of Light Spreading

In order to work with the OSIRIS spectral point spread function it is vital to understand exactly what causes the light to spread within the spectrograph. It is simplest to discuss four main sources: The imaging slit, the diffraction grating, the cumulative effect of the central

limit theorem, and pixelation.

The Imaging Slit

The purpose of the imaging slit, discussed in detail in Section 2.3.3, is to limit the field of view of the OSIRIS spectrograph so that only a 1 km vertical by 40 km horizontal portion of the atmospheric limb passes through the spectrograph. Only the vertical component of the signal is dispersed by the diffraction grating, making the final product of the optical spectrograph a spectrally dispersed image of the slit projected onto the CCD detector. As an example of this, consider Figure 2.9 which displays the final spectrally dispersed image of the slit for a hypothetical atmosphere consisting of only three wavelengths of light, one each from the blue, green, and red portions of the spectrum. In this hypothetical situation the image projected onto the CCD is three distinct, monochromatic one km vertical by 40 km horizontal images of the atmosphere.

Llewellyn et al. (2004) states that the horizontal portion of each of these projected images covers 32 pixels on the CCD, pixels which are 20 x 27 μm in size with the 27 μm in the horizontal direction (*Warshaw et al.*, 1996). It can be shown from this data that each projected monochromatic image illuminates an area that is 21.6 μm vertically by 864 μm horizontally. The 21.6 μm spatial spread in the vertical direction means that the vertical portion of each monochromatic image is slightly wider than the width of one pixel, resulting in the light being detected by multiple pixels once it has passed through the spectrograph. The 21.6 μm spatial spreading is equivalent to a spectral spreading of 0.42 nm, meaning that the imaging slit creates a point spread function of 0.42 nm for every wavelength that passes through the OSIRIS spectrograph (Plot (a) in Figure 3.5).

The Diffraction Grating

Diffraction gratings are used to disperse polychromatic light in such a way that the monochromatic components of the light can be individually examined. Each wavelength of light that interacts with the grating produces a unique irradiance pattern governed by the grating equation, first stated as Equation 2.5 and restated here for convenience,

$$\theta_m = \sin^{-1}\left(\frac{m\lambda}{d}\right), \tag{2.5}$$

where θ_m is the outgoing angle of the maximum irradiance for light of order m, d is the separation between grating lines and λ is the wavelength of light. Of course, Equation 2.5 only provides the angle of maximum irradiance. To determine the actual profile the grating produces for wavelength λ it is helpful to study the equation for the irradiance produced by a configuration of N slits of width b separated by a distance d, as given by

$$I(\theta) = \frac{I(0)}{N^2}\left(\frac{\sin(\beta)}{\beta}\right)^2\left(\frac{\sin(N\alpha)}{\sin(\alpha)}\right)^2, \tag{3.1}$$

where β is given by $(\pi b/\lambda)\sin\theta$ and α is defined as,

$$\alpha = \left(\frac{\pi d}{\lambda}\right)\sin\theta. \tag{3.2}$$

In the limit where b goes to zero the multiple slit configuration becomes a diffraction grating, the term $\left(\frac{\sin(\beta)}{\beta}\right)^2$ goes to unity and Equation 3.1 reduces to

$$I(\theta) = \frac{I(0)}{N^2}\left(\frac{\sin(N\alpha)}{\sin(\alpha)}\right)^2, \tag{3.3}$$

which defines the irradiance profile produced by a diffraction grating as a function of outgoing angle θ, where N is now the total number of lines in the grating. Inserting the values of the OSIRIS spectrograph ($N = 24000$, $d = 1.67$ μm (*Warshaw et al.*, 1996)) into Equation 3.3 and the wavelengths of the sodium doublet results in the irradiance profiles shown in Figure 3.1, which are displayed both as a function of outgoing angle and as a function of wavelength detected by the OSIRIS CCD.

It is clear from Figure 3.1 that the diffraction grating spreads monochromatic light over a notably wide range on the OSIRIS detector. A quick and simple way to quantify the amount of spreading is to find the angular width from the irradiance profile peak to its first minimum. Referring to Equation 3.3, the minima of the profile occur whenever $N\alpha$ is equal to an integer multiple of π, meaning that the change in α, defined as $\delta\alpha$, from the peak to the first minimum is π/N. Differentiating Equation 3.2 with respect to θ yields,

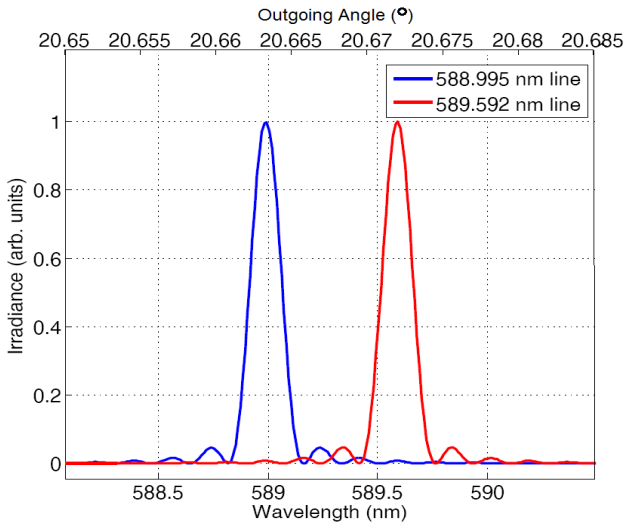

Figure 3.1: The theoretical irradiance profiles of the sodium doublet produced by the OSIRIS diffraction grating.

$$\delta\alpha = \left(\frac{\pi d}{\lambda}\right)\cos\theta\delta\theta = \frac{\pi}{N}, \tag{3.4}$$

which can be rearranged to give the angular distance from the peak to the first minimum, the double of which is considered the angular width of a monochromatic line due to instrumental spreading, or

$$\delta\theta = \frac{2\lambda}{Nd\cos\theta_m}. \tag{3.5}$$

Once the angular width has been determined one need only know the distance from grating to detector in order to calculate the spatial spreading of monochromatic light. In the OSIRIS instrument the path length from diffraction grating to CCD detector is approximately 250 mm, yielding spatial spreading values on the order of 10 μm which is equivalent to a few tenths of a nm spectral spreading. The calculated values of spatial and spectral spreading, also known as the point spread functions of the diffraction grating, are summarized in Figure 3.2 for every OSIRIS wavelength.

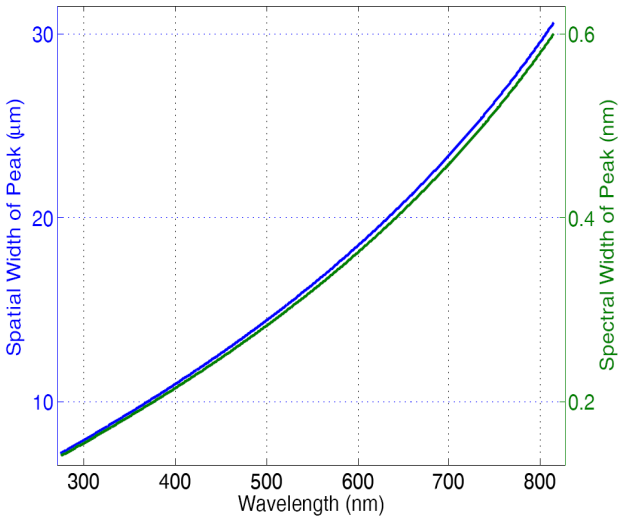

Figure 3.2: OSIRIS spatial and spectral spreading of monochromatic light due to the diffraction grating.

Central Limit Theorem

In addition to OSIRIS imaging slit and diffraction grating, the inherent imperfections in every optical element of the OSIRIS imaging system cause them to disperse light by some finite amount. The spectral point spread functions of the individual components of the OSIRIS spectrograph were not measured prior to launch, making it impossible to quantify their individual contributions. Fortunately it is possible to estimate the shape of their combined effect by means of the central limit theorem, a statistical theory with numerous properties and applications. The central limit theorem property of greatest importance to this thesis is that the mean of a large number of independent variables, each with its own mean and standard deviation, will show a distribution that is approximately normally distributed. As an example of this property, consider a number of individual random variables $X_1, X_2, ..., X_n$, measurable over a range $(-\infty < x < \infty)$ with unique probability distributions $p_1(x), p_2(x), ..., p_n(x)$. The total distribution $p_{tot}(x)$ of all variables $X_1 ... X_n$ is given by the convolution of their probability distributions,

$$p_{tot}(x) = p_1(x) * p_2(x) * ... * p_n(x). \tag{3.6}$$

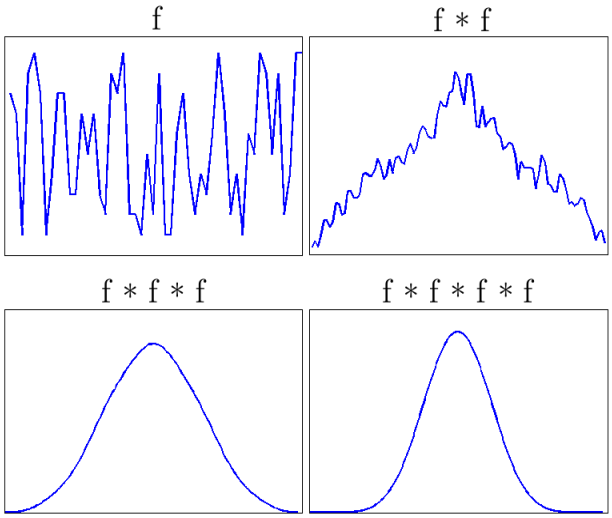

Figure 3.3: Convolving functions together results in a Gaussian curve.

The central limit theorem states that as the number of individual random variables tends towards infinity the total distribution will take on the form of a Gaussian curve. As an example of this theorem consider the data shown in Figure 3.3 wherein a set of random numbers is convolved with itself multiple times. After only three convolutions the result bears a striking resemblance to a Gaussian curve, despite the initial set of numbers having no structure whatsoever. The individual components of the OSIRIS spectrograph are precisely engineered items and as such the distribution of light they produce should be highly structured. It is therefore reasonable to expect that the total distribution of light, or point spread function, from all of the spectrograph components aside from the grating and slit will be in the form of a Gaussian curve. The central limit theorem does not provide a method for determining the width of this curve, but it is possible to make a reasonable estimate of its value from other sources which will be discussed shortly.

Pixelation

The OSIRIS spectrograph is designed to measure 280-810 nm spectrally dispersed light using 1353 columns of pixels, with the signals from each column being binned to produce a 1353 element measurement vector. Each element of this vector has a unique point spread function that describes the spreading of the measured wavelength of light. Of course, the light incident

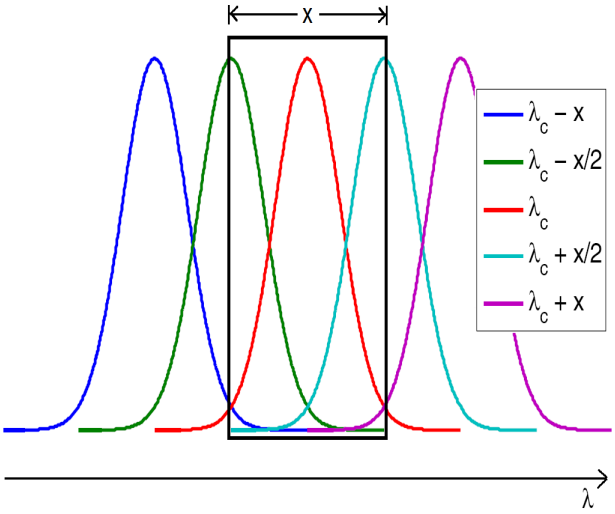

Figure 3.4: Dispersed wavelengths other than the central wavelength λ_c are measured by each pixel of width x, resulting in pixelation which broadens the point spread function.

on OSIRIS is not 1353 monochromatic beams but a continuum of all possible wavelengths, a situation that creates a broadening of each element's point spread function due to an effect known as pixelation.

Consider a single OSIRIS CCD pixel of width x that measures light of a central wavelength λ_c. When light of wavelength λ_c reaches the pixel it will already have been dispersed by the imaging slit, grating, and all other optical elements, resulting in a Gaussian point spread function as predicted by the central limit theorem. The distribution of this light on the pixel is shown in Figure 3.4. While λ_c may be the central wavelength measured by the pixel, light from other nearby wavelengths that have also been dispersed by the spectrograph optics will be measured by the pixel, an effect called pixelation. Figure 3.4 shows four examples of how these non-central wavelengths can be detected by the pixel. As the incident light is a continuum, the impact of pixelation is equivalent to a convolution of the initial central wavelength point spread function with a boxcar function the width of the pixel. Given the information provided in *Llewellyn et al.* (2004), it can be shown that the width of each pixel is equivalent to a spectral range of approximately 0.39 nm.

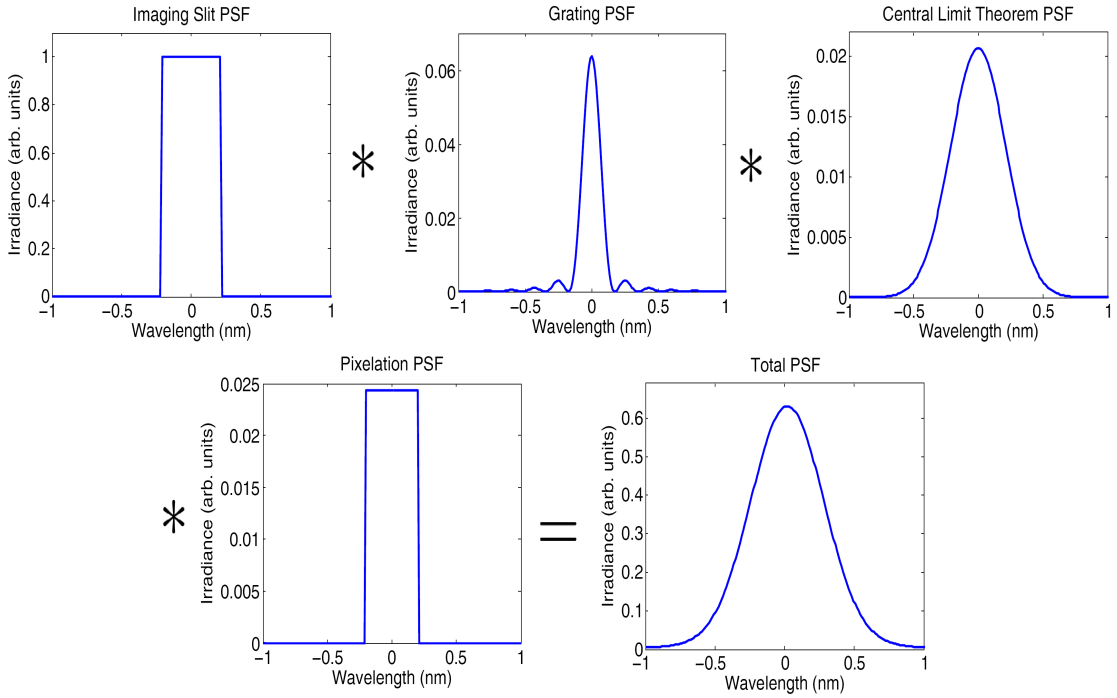

Figure 3.5: The total point spread function for a single OSIRIS wavelength.

3.1.3 The Total Spectral Point Spread Function

With the four major sources of light dispersion in the OSIRIS spectrograph defined it is possible to estimate the total size and shape of the spectral point spread function. The imaging slit, diffraction grating, cumulative effect of the central limit theorem, and pixelation are all independent sources of spreading with correspondingly independent point spread functions. As point spread functions are essentially probability distributions of where a single photon passing through the system will eventually be located, it is possible to take advantage of Equation 3.6 to calculate a total point spread function for every wavelength of the OSIRIS spectrograph.

Figure 3.5 displays the independent normalized point spread functions for 589.592 nm light as a function of spectral spreading and the result of their convolution. Of important note is the irradiance of each of the plots in Figure 3.5. The normalized irradiance of the slit point spread function is a boxcar function with a value of unity as the atmosphere seen by the slit is essentially homogeneous. The normalized point spread functions due to

the diffraction grating, central limit theorem, and pixelation each have a sum of unity due to the fact that each are probability distributions for single photons interacting with the respective instruments. As only the shape of the central limit theorem point spread function is known a Gaussian curve of 0.50 nm full width at half maximum (FWHM) was used in order to get a sense of which individual point spread functions are most important to the total. The magnitude and structure of the total point spread function provides reasonable evidence to suggest that the shape of the total point spread function can be approximated as a Gaussian. It is also important to remember that the diffraction grating point spread function is wavelength dependent (see Equation 3.5) which introduces a wavelength dependence into the total point spread function. It is therefore reasonable to assume that each wavelength of the spectral point spread function should have a Gaussian shape with a unique FWHM value.

3.1.4 Verification of the Gaussian Curve Approximation

In order to verify the assumption that the point spread function of each OSIRIS wavelength can be modelled as a Gaussian curve it is necessary to view a source of monochromatic light with the OSIRIS spectrograph. Fortunately such a source exists in Earth's atmosphere, as auroral emissions that occur at wavelengths of 557.7 and 630.0 nm are for all intents and purposes monochromatic. These emissions occur high in the atmosphere, with the minimum altitude for 557.7 nm light being approximately 110 km while for 630.0 nm light the minimum altitude is approximately 200 km (*Babcock*, 1923). It therefore becomes possible, whenever the tangent altitude of an OSIRIS measurement is greater than 70 km, to observe these auroral emissions without significant contamination from limb scattered light. An example of this type of measurement is shown in Figure 3.6, where the two auroral emission lines are clearly visible in the OSIRIS spectrum. There has clearly been spreading of the monochromatic light by the spectrograph and the shape of the spreading is very nearly Gaussian, as evidenced by the Gaussian curves imposed over each emission line. Also of note is that the FWHM of the 630.0 nm line is larger than the FWHM of the 557.7 nm line. These results make it reasonable to approximate the point spread function at each wavelength as a Gaussian curve, and as such the spectral point spread function of the OSIRIS spectrograph can be defined as

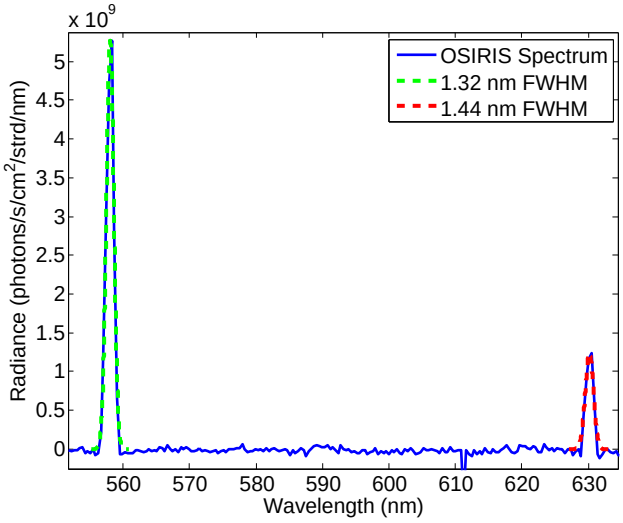

Figure 3.6: Auroral emission lines observed by OSIRIS.

an array of FWHM values with each value describing the Gaussian curve associated with a single OSIRIS wavelength.

3.2 A Time-Dependent OSIRIS Spectral Point Spread Function

The current OSIRIS spectral point spread function used in all atmospheric constituent profile retrievals is shown in Figure 3.7. Measured prior to launch during OSIRIS calibration, it provides, for every OSIRIS wavelength, a single time-independent FWHM value of the Gaussian curve that best represents the spreading of light. The time-independent nature of the current spectral point spread function introduces an obvious issue. Any onboard changes that alter the spreading of light in the spectrograph are not accounted for. The onboard changes could occur for a number of possible reasons: temperature changes causing expansion or contraction of elements within the spectrograph; the accumulation of dust particles; instrument degradation due to radiation exposure; etc. Whatever the reason, the development of a time-dependent spectral point spread function would allow these changes to be accounted for and significantly improve the quality of OSIRIS ozone retrievals, reducing

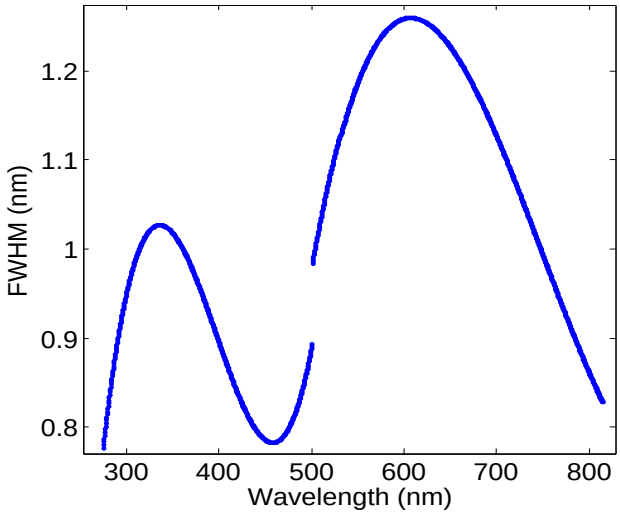

Figure 3.7: The current, time-independent OSIRIS spectral point spread function FWHM values.

the differences seen between OSIRIS and SAGE II profiles as well as making it possible to undertake the analysis necessary for the ACSO Commission. As first discussed in Section 2.6.3, the ozone cross section is only sensitive to the spectral point spread function in the structured regions of the Hartley and Huggins bands. The development of a time-dependent spectral point spread function will therefore be limited to the 310–350 nm wavelength range.

3.2.1 Calculating a Time-Dependent Spectral Point Spread Function

A significant portion of the work of this thesis was spent developing a method to calculate a time-dependent spectral point spread function. The final method consists of three parts: Verifying a suitable reference solar spectrum, removing the signatures of atmospheric interaction from OSIRIS measurements, and comparing the altered OSIRIS measurements to a series of convolved reference solar spectra.

Fraunhofer Features & A Reference Solar Spectrum

The method developed in this thesis for calculating the time-dependent OSIRIS spectral point spread function relies heavily on the Fraunhofer features of the solar spectrum. Fraunhofer features are caused by photons of a particular wavelength which are radiating outward from the sun interacting with the gases in the outer layers of the solar atmosphere. The photons are absorbed or scattered in random directions, lowering the total outward signal of that wavelength. The efficiency of scattering and absorption is wavelength dependent, meaning the signals of some wavelengths can be much lower than others. The end result is a set of sharp peaks and valleys, called Fraunhofer features, superimposed on what would otherwise be the smoothly varying blackbody radiation spectrum of the sun. At the core of the method is a comparison of the Fraunhofer features measured by OSIRIS against Fraunhofer features from a reference, top-of-atmosphere (TOA) solar spectrum. The reference solar spectrum used in this work was produced by *Kurucz et al.* (1984) and was measured using the McMath Fourier Transform Spectrometer at the National Solar Observatory on Kitt Peak in Arizona, a ground based instrument that makes solar observations through Earth's atmosphere. Kurucz later removed the signatures of atmospheric absorption and scattering and adjusted the measured spectrum to agree with that produced by *Thuillier et al.* (2003), a low-resolution solar spectrum measured onboard the Space Shuttle. The result is a high-resolution TOA spectrum that can be convolved with an instrument point spread function to produce the spectrum as seen by that instrument.

Considering that Kurucz manually removed the signatures of atmospheric interaction it is vital to confirm that the reference spectrum does not contain any significant residual signals which could affect the comparisons between the OSIRIS and reference solar spectra. To ensure this, the reference solar spectrum was compared against OSIRIS measurements of moon-reflected sunlight. The light in these OSIRIS measurements has not passed through the Earth's atmosphere, and thus can be considered as an OSIRIS-resolution TOA solar spectrum. After correcting for albedo effects and normalizing, the scans were compared to the Kurucz spectrum as shown in Figure 3.8.

The fact that the two measurements shown in Figure 3.8 are not exactly identical is of

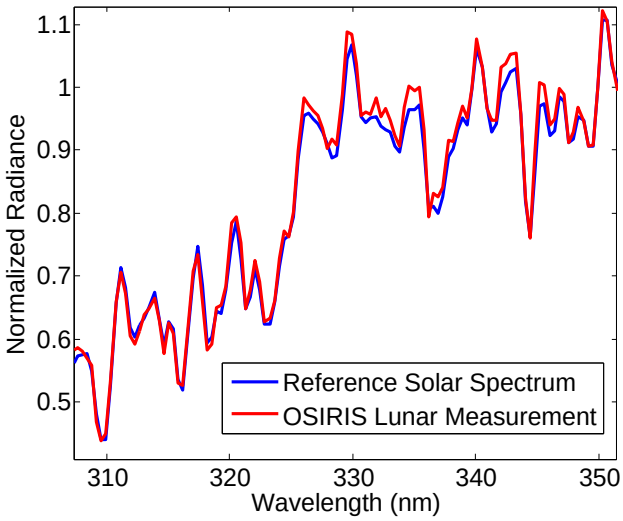

Figure 3.8: Comparison of normalized OSIRIS lunar measurement and reference solar spectrum in ozone absorption wavelengths.

little concern. What is important is that the overall structure of the two measurements, i.e. the peaks and valleys that are wider than 1 nm, are the same. If this were not the case then either the atmospheric interaction signature removal performed on the Kurucz spectrum was not completed correctly or the surface of the moon has an absorption feature which was not accounted for. The fact that the overall structure agrees so well is verification that the Kurucz spectrum is a reliable spectrum to use in the wavelengths of interest to this thesis.

Preparing OSIRIS Scans for Comparison

Before OSIRIS measurements can be compared with the TOA reference solar spectrum of Kurucz, any signatures of atmospheric absorption or scattering in the OSIRIS spectrum must be removed. In the 310–350 nm wavelength band for which a time-dependent spectral point spread function will be developed the two most prominent sources of atmospheric interaction are Rayleigh scattering and absorption of light by ozone. It must be stated at this time that the removal of the ozone absorption signature involves the use of Kurucz reference spectrum at OSIRIS resolution, a dataset retrieved by convolving the high resolution reference spectrum with the time-independent spectral point spread function. As the current goal is to develop a time-dependent spectral point spread function, the use of the time-independent spectral

point spread function seems suspect. However, it was found through work not shown in this thesis that its values are sufficient to allow the signatures of atmospheric interaction to be reduced to a negligible level.

Choice of Altitude To develop a time-dependent spectral point spread function one measurement from every OSIRIS scan will be compared with the reference solar spectrum. As the measurements of each scan are all taken at different tangent altitudes it is important to consistently choose measurements with a standard tangent altitude in order to minimize any scan-to-scan deviation. It was determined that every OSIRIS scan would be represented by the measurement taken closest to 55 km tangent altitude. Such a tangent altitude is low enough to ensure a strong signal-to-noise ratio, while at the same time being high enough to ensure that none of the wavelengths of interest have become optically thick.

Rayleigh Scattering When a photon is elastically scattered by a particle whose size is much smaller than the wavelength of the photon, the event is said to be an instance of Rayleigh scattering. A detailed discussion of the theories and equations governing Rayleigh scattering can be found in *Bates* (1984), but for the purposes of this thesis one need only know that for a given radiance I_0 the radiance of Rayleigh scattered light I is inversely proportional to the fourth power of the photon wavelength λ, or

$$I \propto \frac{1}{\lambda^4} I_0. \tag{3.7}$$

Equation 3.7 makes it possible to remove the signature of Rayleigh scattering from OSIRIS measurements by multiplying the OSIRIS measurement by λ^4. The magnitude of the resulting spectrum is meaningless but its overall structure becomes much closer to that of a TOA spectrum, as shown in the Figure 3.9 which displays the normalized OSIRIS spectrum before and after removal of the Rayleigh scattering signature along with the normalized OSIRIS-resolution TOA reference spectrum. Figure 3.9 makes it clear that Rayleigh scatter is the only significant source of atmospheric interaction at wavelengths inefficiently absorbed by ozone. At wavelengths longer than 335 nm the spectrum with no Rayleigh scatter signature essentially falls on top of the reference TOA spectrum.

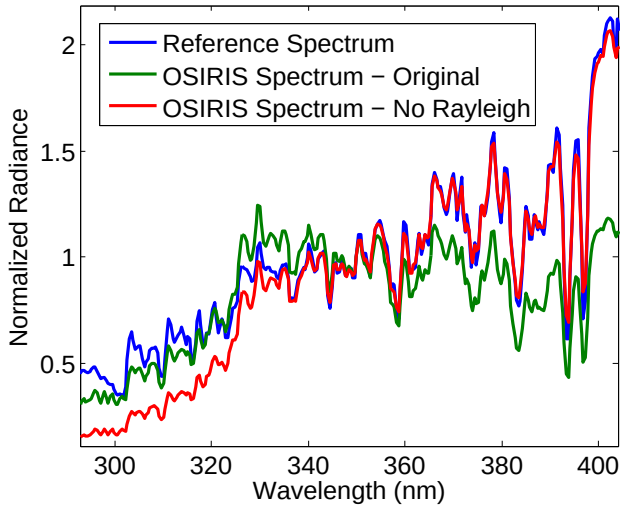

Figure 3.9: The effect of removing the signature of Rayleigh scattering from the OSIRIS spectrum. Spectra normalized at the 350 nm datapoint.

Absorption by Ozone The signature of absorption by ozone is removed from the OSIRIS spectrum by taking advantage of the Beer-Lambert Law, an equation describing the attenuation of light due to absorbing substances, first discussed in Section 2.4.2 and restated here in its exponential form for a single absorbing constituent,

$$I_f = I_0 e^{-\sigma nds}. \tag{3.8}$$

In the current situation the only known values are the ozone cross section σ and the attenuated signal I_f (the Rayleigh corrected OSIRIS spectrum) while it is desired to determine the unattenuated, TOA signal I_0. By temporarily treating the normalized reference Kurucz spectrum as the incident signal I_0 it becomes possible to rearrange Equation 3.8 and solve for the value of nds at each wavelength,

$$nds = -\frac{1}{\sigma} \ln\left(\frac{I_f}{I_0}\right). \tag{3.9}$$

The term nds can be defined as the apparent ozone column, and gives a first order estimate of the total amount of ozone present along the OSIRIS line of sight. Due to the simplistic nature of this approach the value of the apparent ozone column varies with wavelength, but it was found that wavelength bands several nanometers wide could be represented by a single,

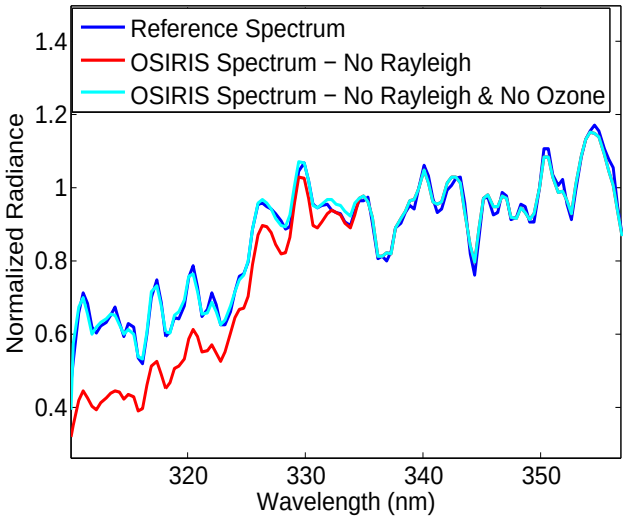

Figure 3.10: The effect of removing the signatures of Rayleigh scattering and absorption by ozone from the OSIRIS spectrum. Data normalized to the 350 nm datapoint.

averaged value of the apparent ozone column, $(nds)_{\text{ave}}$. For each wavelength band the value of $(nds)_{\text{ave}}$ was inserted into Equation 3.8, which could then be rearranged to solve for the unattenuated, TOA signal I_0,

$$I_0 = I_f e^{\sigma(nds)_{\text{ave}}}. \tag{3.10}$$

An example of the normalized TOA spectrum that results from this ozone signature removal process is shown in Figure 3.10. Clearly when the signatures of Rayleigh scattering and absorption by ozone are removed from the OSIRIS signal it becomes, for all intents and purposes, a top-of-atmosphere signal in the 310–350 nm wavelength range.

Convolution of the Reference Spectrum & Comparisons with OSIRIS

With the ability to retrieve a top-of-atmosphere spectrum for any OSIRIS scan in the 310–350 nm wavelength range comes the opportunity to directly compare the Fraunhofer features of the OSIRIS spectrum against the Fraunhofer features of the reference solar spectrum developed by Kurucz. Obviously before any comparisons can take place the reference solar spectrum must be brought to the resolution of the OSIRIS spectrograph. In the previous section, a single OSIRIS resolution reference spectrum was produced via convolution with

the time-independent spectral point spread function, but for the current analysis a series of OSIRIS resolution reference spectra are produced, each convolved with a unique Gaussian curve. The FWHM of the curves ranges from 0.40 nm to 1.50 nm in 0.01 nm increments, resulting in 110 unique OSIRIS resolution reference solar spectra.

The Fraunhofer features of each of these 110 convolved reference spectra can then be compared against the Fraunhofer features of the TOA OSIRIS spectrum. The comparisons are completed by creating 110 "absolute difference spectra" each of which is simply an array containing the point-by-point absolute differences between the TOA OSIRIS spectrum and one of the 110 convolved reference spectrum for three wavelength ranges of the OSIRIS spectrum. These wavelength ranges are between 5 and 10 nm wide and are centred on 313, 320, and 350 nm as shown in Figure 3.11. While all Fraunhofer features shown in Figure 3.11 were considered, the three boxed regions were selected as the features of these regions were found to be stable and displayed particularly good correlation between the TOA OSIRIS spectrum and the convolved reference spectra. Each wavelength range is used to compute the point spread function for its central wavelength, a task completed by calculating the sum of the absolute differences within the wavelength range for each of the 110 absolute difference spectra. The absolute difference spectrum whose sum is lowest for a wavelength range is taken as the best fitting spectrum for that range, and the Gaussian curve used in the convolution that created this best fitting spectrum is taken as the point spread function for the central wavelength of that range. In this way it is possible to determine the point spread function of three OSIRIS wavelengths for any OSIRIS scan.

A piecewise approach is used to create a spectral point spread function over the entire 310–350 nm wavelength range. Wavelengths lower than 313 nm are assigned the point spread function calculated at 313 nm, while linear interpolations are applied for wavelengths in the ranges 313–320 nm and 320–350 nm. Completing this process for every scan in the OSIRIS mission results in a spectral point spread function that is time-dependent.

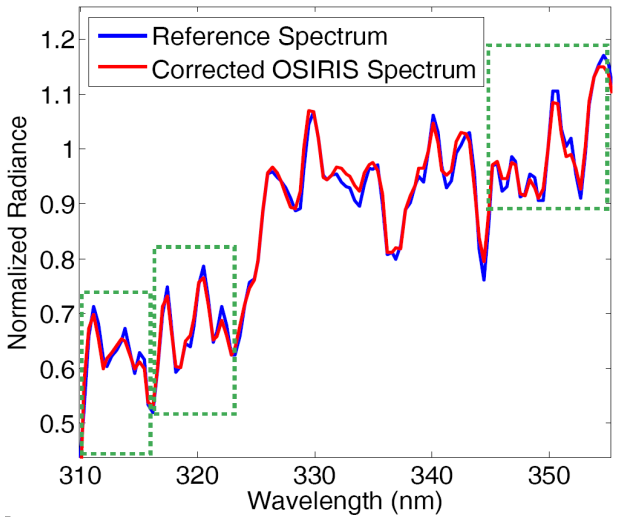

Figure 3.11: The boxed areas show wavelength regions where Fraunhofer features can be successfully compared.

3.3 Summary

By comparing the Fraunhofer features present in OSIRIS measurements against the Fraunhofer features of a reference spectrum convolved with various Gaussian curves it is possible to calculate a unique spectral point spread function in the 310–350 nm range for any scan in the OSIRIS mission history. Such a time-dependent spectral point spread function will improve OSIRIS ozone retrievals by accounting for changes in the final dispersion pattern of light produced by the OSIRIS spectrograph. However, it is necessary to verify this time-dependent spectral point spread function is correct before it can be implemented into the SASKTRAN radiative transfer model.

Chapter 4

Modelling the Time-Dependent Spectral Point Spread Function

With the problem of developing a time-dependent spectral point spread function solved, it is appropriate to shift focus slightly and ask the question: Is it possible to model the spectral point spread function with an equation that uses measured satellite parameters as variables? Successfully doing so would provide excellent verification of the point spread function calculation method developed in Section 3.2. A proper model would also minimize any noise carried through such calculations; it would effectively act as a smoothing tool. The results of this Chapter reveal that the spectral point spread function and OSIRIS optics temperature show a rough anti-correlation, one that is not sufficient for modelling purposes. However, success can be achieved by relating the spectral point spread function to optics temperature and satellite track angle.

4.1 Spectral Point Spread Function & Optics Temperature

An obvious parameter that may be related to spectral point spread function is the optics temperature of the OSIRIS spectrograph. It is a logical expectation that as the OSIRIS spectrograph optics undergo changes in temperature the resulting thermal expansions and contractions would modify the spectral point spread function in some way. Also of note is that the optics temperature measurements display a minimal amount of noise. If a relationship can be found that successfully models the spectral point spread function given the optics temperature, it would have the effect of reducing any random noise carried through the

initial calculation of the spectral point spread function.

4.1.1 The Effect of Orbit on Satellite Temperature

Changes Throughout the Year

The temperature of the Odin spacecraft is governed by its sun-synchronous orbit around the Earth. The 600 km altitude of Odin ensures that there is essentially no convective or conductive heating or cooling of the spacecraft, meaning its temperature is altered only by the flux of radiation it receives and emits. The primary source of radiation incident on the spacecraft is the sun. Solar radiation is absorbed by a set of panels which convert the radiation to usable energy that is consumed by the instruments and dissipated as heat. The design of the satellite is such that the panels also serve as a shade to protect all instruments on the spacecraft from direct exposure to sunlight (*Murtagh et al.*, 2002). Therefore the amount of radiation being collected, and by extension the temperature of the spacecraft, is dependent on the angle made between the plane of the panels and the direction of incoming sunlight.

When the panels are perpendicular to incoming sunlight, the surface area available to absorb solar radiation is at a maximum which leads to maximum power production and satellite temperature. However, this state is achieved only twice annually. As discussed in *Murtagh et al.* (2002), operational necessities dictate that the plane of the panels be parallel to the plane of the orbit. Because of this condition the amount of solar radiation the panels can gather is affected by the axial tilt of the Earth. With the orbit set at a constant inclination of 97.8° the angle between the orbital plane and the incident radiation varies throughout the year, examples of which are shown in Figure 4.1. By calculating the sine of the angle between the orbital plane and the solar radiation vector it is possible to determine the points of maximum and minimum solar panel exposure. Figure 4.2 shows the result of this calculation for an entire year.

The two local maxima in Figure 4.2, occurring at March 2 and October 9, correspond to the times when the orbital plane and thus the solar panels are perpendicular to the incoming sunlight. Solar radiation absorption, power production, and satellite temperature

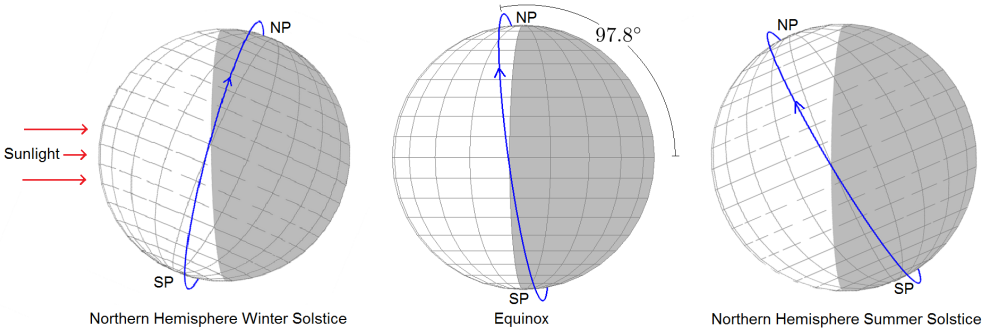

Figure 4.1: The effect of Earth's axial tilt on the angle between the orbital plane and incident sunlight.

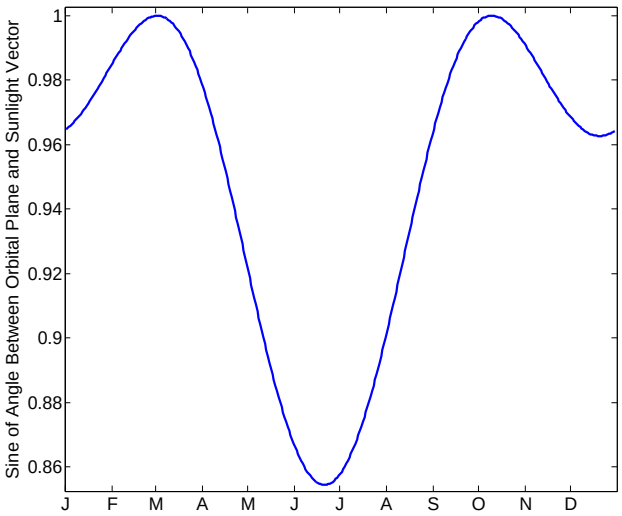

Figure 4.2: Solar panel surface area availability over one year.

are therefore expected to be at a maximum on these dates. The local minima occur at June 21 and December 21, corresponding to the Northern hemisphere summer and winter solstices, respectively. Of important note is the difference in surface area availability at the solstices. The 97.8° inclination of the satellite orbit serves to amplify the effect of Earth's axial tilt during the Northern hemisphere summer while reducing the effect during the Northern hemisphere winter (see Figure 4.1). Also, during the Northern hemisphere summer the Earth's axial tilt and the orbit inclination combine to create a situation where the satellite slips into eclipse behind the Earth for a portion of its orbit. During these eclipse times the temperature of the satellite is noticeably altered.

Eclipse

During each Northern hemisphere summer the Odin satellite falls into the shadow of the Earth for a portion of its orbit. Figure 4.3 shows the eclipse times and positions of the satellite, where satellite track angle is defined as the angle around the satellite track with the ascending node (the northward equatorial crossing) defining 0°. It is expected that the lack of solar radiation will lead to a drop in satellite temperature during these times. Figure 4.4, which displays the temperature of the OSIRIS spectrograph optics averaged over one day and eight degree intervals around the satellite track for all of 2008, verifies this expectation. During times when the satellite experiences eclipse for a portion of its orbit the temperature of the satellite and its instruments drops by several degrees Celsius. The effect is greatest during the summer solstice when the satellite spends the greatest amount of time in eclipse (approximately 21% of its orbit).

The mid-April and mid-August temperature spikes are due to the presence of a heating element designed to counter the decrease in temperature caused by the eclipse. The element is turned on in April or May each year, remains on for the duration of the eclipse period, and is shut off again in August or September. Despite the presence of the heating element the OSIRIS optics clearly still suffer from temperature changes during the eclipse period.

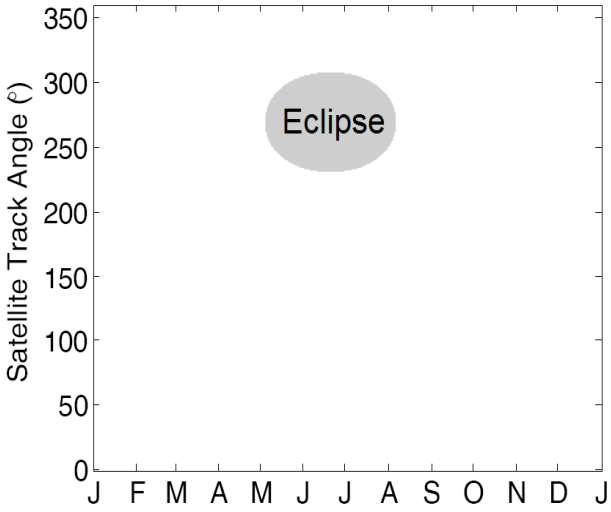

Figure 4.3: Satellite positions and times of eclipse.

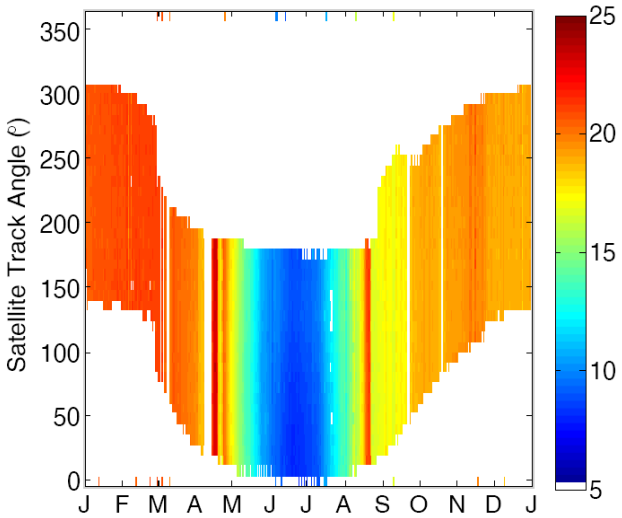

Figure 4.4: Optics temperature in degrees Celsius for 2008.

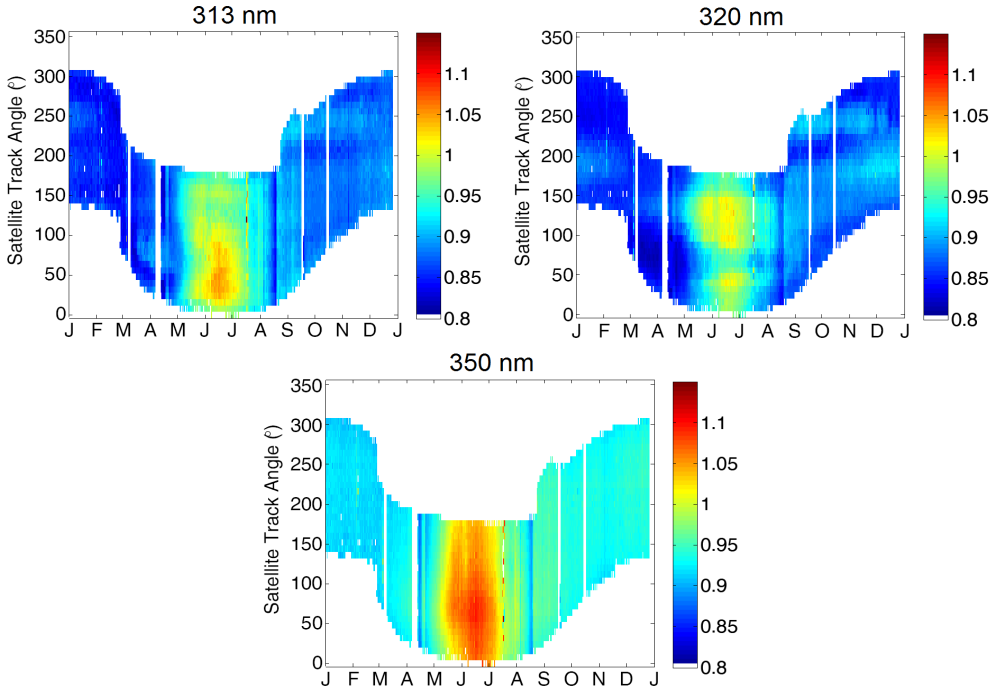

Figure 4.5: Point spread function FWHM at 313, 320, and 350 nm for 2008.

4.1.2 Relating Temperature to Spectral Point Spread Function

Verifying a Potential Relationship

The time-dependent point spread functions shown in Figure 4.5 give hope for a relationship when compared against the 2008 optics temperature shown in Figure 4.4, as the spectral point spread function appears to be anti-correlated to optics temperature. The highest optics temperature values correspond to the lowest point spread function values and vice versa. Both figures also clearly show changes caused by the Northern hemisphere summer eclipse. However, the plots in Figures 4.4 and 4.5 were formed by averaging the data over both time and satellite position. In order to truly determine whether spectral point spread function is related to optics temperature, the two parameters will need to be compared on a scan-by-scan basis.

Figure 4.6 shows the calculated point spread function at 350 nm for every scan from March 2, 2009, with each orbit easily distinguished by a noticeable time lapse between scans. On this day the orbital plane of the satellite was approximately perpendicular to the direction

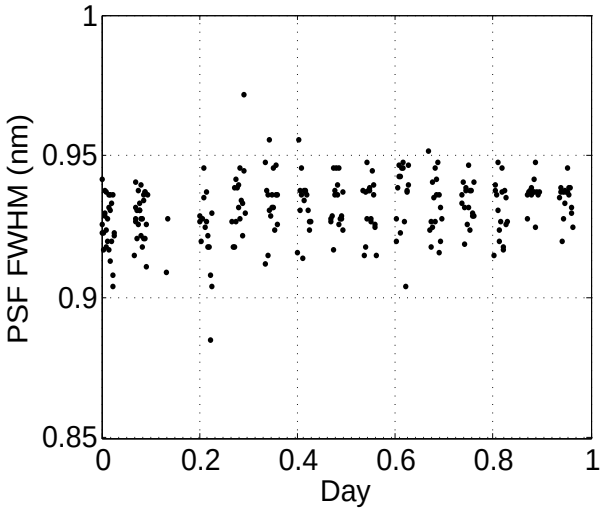

Figure 4.6: The calculated point spread function FWHM values at 350 nm for every scan from March 2, 2009.

of incoming sunlight, meaning a maximum in solar radiation absorption and presumably a minimum in change in point spread function over the course of an orbit. Ignoring obvious outliers, there is a significant amount of noise in the calculated point spread function; the values vary by approximately ± 0.020 nm with no discernible trends over each orbit. As discussed above, finding a relationship that successfully predicts point spread function given the optics temperature could potentially yield a modelled point spread function with significantly less noise. Based on the results of Figure 4.6 it was decided that an acceptable relationship would allow the optics temperature to model the point spread function such that for 95% of scans the absolute difference between modelled and calculated point spread functions would be less than 0.020 nm. For this criteria to hold the difference between modelled and calculated point spread functions must show a mean of zero and a standard deviation of 0.010 nm or less.

Multiple Linear Regression Analysis

The technique chosen to examine the potential relationship between spectral point spread function and optics temperature was multiple linear regression, where the relationship between a single dependent variable and multiple independent variables is modelled with a

least squares approach. Given a data set containing one dependent variable y and b independent variables denoted $x_1 \dots x_b$, with each variable containing N data points, the potential relationship can be modelled as a linear equation of the form,

$$y_n = a_1 x_{1n} + a_2 x_{2n} + \cdots + a_b x_{bn} + \epsilon_n, \tag{4.1}$$

where n is the data point being evaluated, $a_1 \dots a_b$ are coefficients corresponding to each independent variable and ϵ represents the difference between the model and the actual value of y_n. It is important to note that the independent variables themselves need not be linear. The goal of the least squares approach is to determine the coefficients $a_1 \dots a_b$ such that the sum of the squared values of ϵ_n, shown as

$$E = \sum_{n=1}^{N} \epsilon_n^2, \tag{4.2}$$

is minimized. In order to find the appropriate values of $a_1 \dots a_b$, it is helpful to first rearrange Equation 4.1 and combine it with Equation 4.2,

$$E = \sum_{n=1}^{N} \left(y_n - (a_1 x_{1n} + \cdots + a_b x_{bn})\right)^2. \tag{4.3}$$

From calculus it is known that when the value of E is at a minimum its total derivative will have a value of zero. To ensure this situation occurs the partial derivative of E with respect to each of the coefficients in Equation 4.3 must also be zero, or

$$dE = \frac{\partial E}{\partial a_1} = \cdots = \frac{\partial E}{\partial a_b} = 0. \tag{4.4}$$

Applying these conditions yields a series of equations,

$$\frac{\partial E}{\partial a_1} = \sum_{n=1}^{N} 2\left(y_n - (a_1 x_{1n} + \cdots + a_b x_{bn})\right)(-x_{1n}) = 0; \tag{4.5}$$

$$\vdots$$

$$\frac{\partial E}{\partial a_b} = \sum_{n=1}^{N} 2\left(y_n - (a_1 x_{1n} + \cdots + a_b x_{bn})\right)(-x_{bn}) = 0; \tag{4.6}$$

which can be simplified and rearranged into a more convenient form,

$$\sum_{n=1}^{N} y_n x_{1n} = a_1 \sum_{n=1}^{N} x_{1n}^2 + \cdots + a_b \sum_{n=1}^{N} x_{1n} x_{bn} \tag{4.7}$$

$$\vdots$$

$$\sum_{n=1}^{N} y_n x_{bn} = a_1 \sum_{n=1}^{N} x_{1n} x_{bn} + \cdots + a_b \sum_{n=1}^{N} x_{bn}^2. \tag{4.8}$$

In this form it is possible to simplify the equations into a single matrix equation,

$$\begin{bmatrix} \sum_{n=1}^{N} y_n x_{1n} \\ \vdots \\ \sum_{n=1}^{N} y_n x_{bn} \end{bmatrix} = \begin{bmatrix} \sum_{n=1}^{N} x_{1n}^2 & \cdots & \sum_{n=1}^{N} x_{1n} x_{bn} \\ \vdots & \ddots & \vdots \\ \sum_{n=1}^{N} x_{1n} x_{bn} & \cdots & \sum_{n=1}^{N} x_{bn}^2 \end{bmatrix} \begin{bmatrix} a_1 \\ \vdots \\ a_b \end{bmatrix}. \tag{4.9}$$

Finally, by taking the inverse of the square matrix it is possible to solve for the coefficients,

$$\begin{bmatrix} a_1 \\ \vdots \\ a_b \end{bmatrix} = \begin{bmatrix} \sum_{n=1}^{N} x_{1n}^2 & \cdots & \sum_{n=1}^{N} x_{1n} x_{bn} \\ \vdots & \ddots & \vdots \\ \sum_{n=1}^{N} x_{1n} x_{bn} & \cdots & \sum_{n=1}^{N} x_{bn}^2 \end{bmatrix}^{-1} \begin{bmatrix} \sum_{n=1}^{N} y_n x_{1n} \\ \vdots \\ \sum_{n=1}^{N} y_n x_{bn} \end{bmatrix}. \tag{4.10}$$

Relationships During Portions of the Mission

Yearly Relationships Given the large number of scans made by OSIRIS over the course of its mission it was deemed prudent to break the mission into one year sections and examine those sections for any satisfactory relationships between spectral point spread function and temperature. Figure 4.7 shows the orbitally averaged point spread functions plotted against the orbitally averaged optics temperature for years 2002–2010 for the 350 nm wavelength. Orbitally averaged point spread functions and optics temperatures are shown here to avoid over-saturation of data within the plots. To search for possible relationships between the two parameters plots similar to Figure 4.7 but using individual scans rather than orbital averages were created and a series of polynomial curves were fitted to each of the three wavelengths using multiple linear regression analysis. As stated above, the conditions for a satisfactory

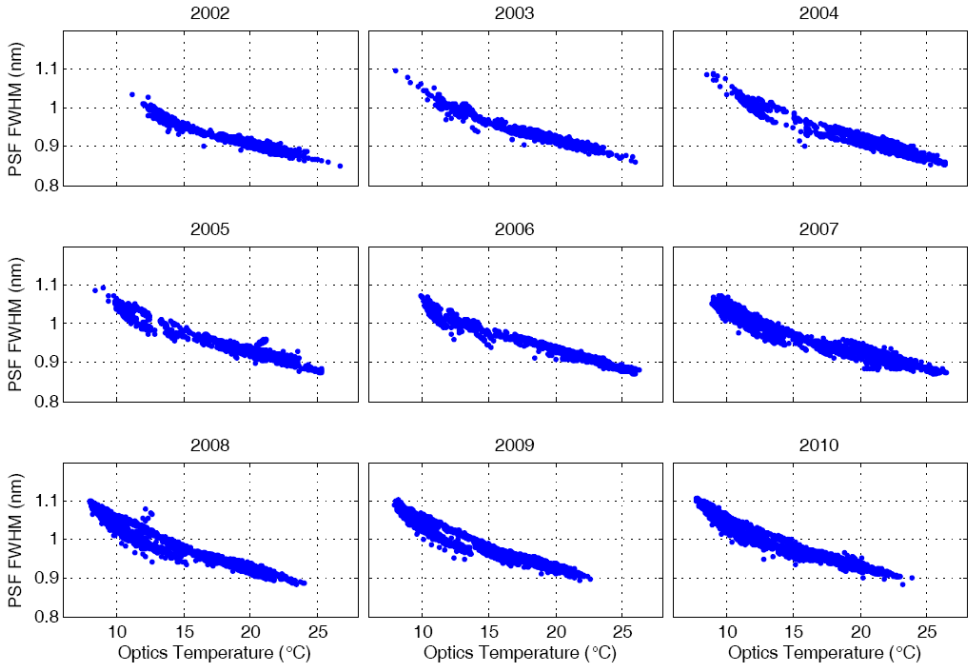

Figure 4.7: Orbitally averaged point spread function FWHM plotted against temperature for 350 nm.

curve were that the difference between the curve and the data have a mean of zero and a standard deviation of 0.010 nm.

As shown in Figure 4.8, only during 2002 are both a straight line fit and a parabolic fit through the data satisfactory for the 350 nm wavelength. At no point throughout the OSIRIS mission do the standard deviations of the 313 and 320 nm wavelengths analyses reach the desired standard deviation. The large rise in standard deviation at 320 nm is due to an increase in point spread function variation throughout the orbit, discussed in greater detail in Section 4.1.2. It can therefore be concluded that examining the data on a yearly basis does not yield a satisfactory relationship between spectral point spread function and optics temperature. A satisfactory relationship between spectral point spread function and optics temperature may still exist though, as in Figure 4.7 the plots of 2004, 2005, 2008, and 2009 reveal what may be two distinct curves, possibly indicating a relationship that varies throughout a single year. It should be noted that while only the straight line and parabolic fits are displayed in Figure 4.8 several higher order polynomials were also fitted with similar

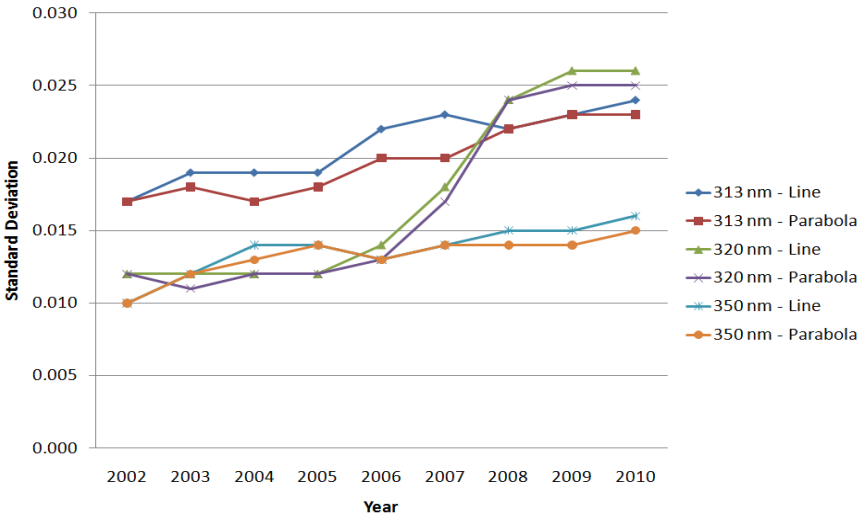

Figure 4.8: Standard deviations of the difference between fitted curves to the yearly data.

findings.

Relationships Over a Portion of a Year If the relationship between spectral point spread function and optics temperature varies over the course of a year, then it is necessary to first break a single year into defined periods. For this investigation four distinct time periods were defined: Prior to eclipse, during eclipse before the summer solstice, during eclipse after the summer solstice, and after eclipse. The eclipse period is defined here as the period when the heating element onboard Odin is active. This definition was chosen as it provides a simple, distinct, and noticeable division. The eclipse period was divided at the summer solstice because on that date that spacecraft spends the maximum amount of time per orbit in eclipse; the before and after periods therefore correspond to the gradual cooling and warming that the satellite experiences over the entire eclipse period. The results of this breakdown for 2009 are shown in Figure 4.9. One of the curves seen in the eclipse data clearly corresponds to data from before the summer solstice while the other curve is composed of data from after the solstice. Possible reasons for this separation are discussed in Section 4.1.2.

It is evident from Figure 4.9 that the data from a single year can be successfully separated

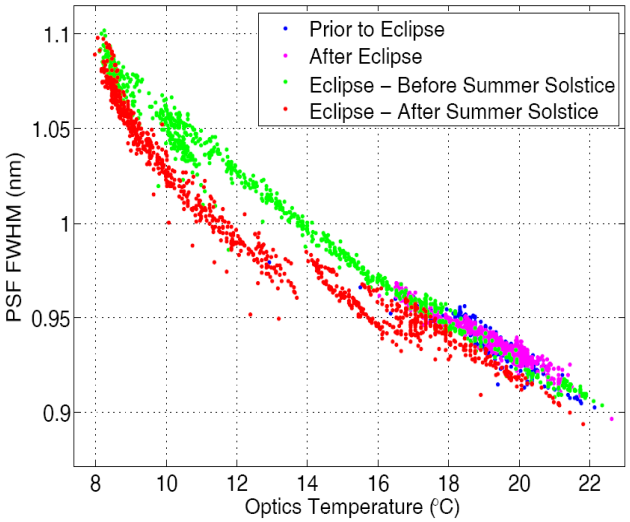

Figure 4.9: The average point spread function FWHM at 350 nm for every orbit of 2009.

into four distinct periods. An attempt was therefore made to find a satisfactory relationship between spectral point spread function to optics temperature for each of these periods on a scan-by-scan basis from years 2002–2011. The method and criteria were the same as described in Section 4.1.2, where the difference between the data and the fitted curve must show a mean of zero and a standard deviation of less than 0.010 nm.

Figure 4.10 displays, for the 350 nm wavelength, the standard deviation of the difference between the data and the best fit first and second order polynomials. The straight line and parabolic fits proved to be the two best overall choices; as before, higher order polynomials were fitted to the 350 nm wavelength as well as the 313 and 320 nm wavelengths and showed results similar to, yet not quite as good, as those in Figure 4.10. It is evident from Figure 4.10 that the goal of a standard deviation of 0.010 nm was not found, indicating that a satisfactory relationship between spectral point spread function and optics temperature is not consistently achievable even when a single year is broken down into discrete periods of time.

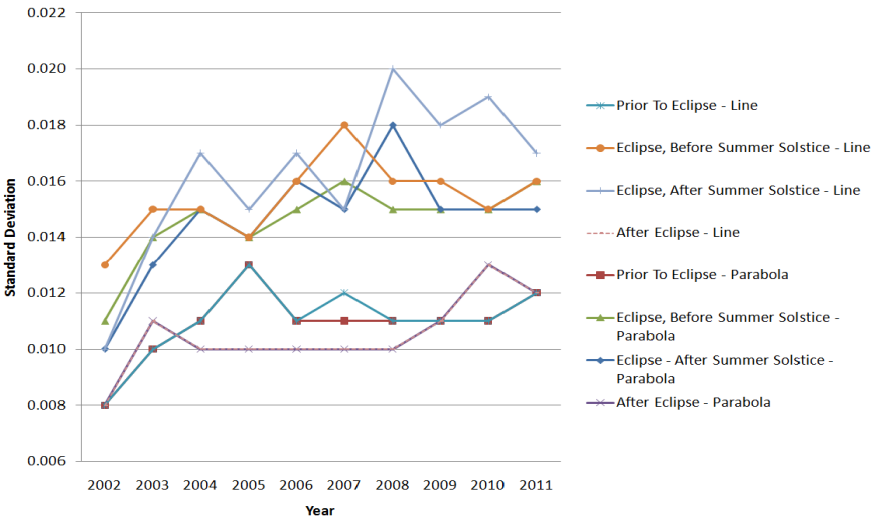

Figure 4.10: Standard deviations of the difference between fitted curves and point spread function at 350 nm.

Possible Explanations

Attempting to relate the spectral point spread function of the OSIRIS spectrograph to its optics temperature has a number of limitations. To begin, the optics temperature is measured with a single thermistor located within the optics box. What is being recorded and used as the temperature of the entire optics box is actually the temperature as measured at a single location, making it impossible to know any information about possible temperature gradients. For example, if a temperature is recorded at one moment in time and a temperature gradient is present (the optics to the left of the thermistor are "hot", while to the right are "cold"), the next time that same temperature is recorded the gradient within the box could be completely different (to the left of the thermistor may now be "cold", while to the right is "hot"). In both cases the recorded temperature will be the same yet the spectral point spread function, which is affected by the thermal expansions and contractions of the entire optics box, could be completely different.

An unaccounted for temperature gradient may be the reason that the spectral point spread function and optics temperature seem to have a different relationship before and after the summer solstice as shown in Figure 4.9. Before the solstice the satellite is going further and further into eclipse with every passing orbit. The satellite therefore cools down

over time (see Figure 4.4) which may create a particular temperature gradient within the optics. After the summer solstice the satellite begins to slowly warm up as the amount time spent in eclipse per orbit decreases, which may create a different temperature gradient. A situation may therefore be occurring where, although the recorded optics temperature appears approximately the same at equal times before and after the summer solstice, the spectral point spread function may be quite different.

To examine the impact the use of only a single thermistor has it would be necessary to have multiple thermistors located at various points throughout the optics box. As this is not possible the impact of using a single thermistor to represent the temperature of the entire optics box is unknown, and must be kept in mind when discussing the impact of optics temperature on spectral point spread function.

Another possible source that introduces error when examining spectral point spread function and optics temperature is the power mode that the Odin spacecraft is in. As stated previously, the typical procedure for minimizing the effects of the eclipse is to switch from one power mode (where the heating element is off) to another (where the heating element is on). However, these are not the only two power modes available to the Odin spacecraft. As discussed in *Murtagh et al.* (2002), the Sub-Millimetre Radiometer (SMR), the device that shares Odin with OSIRIS, has four main modes of observation, each designed to optimize the observation of a certain scientific topic. Each of these modes requires a unique amount of power to operate, meaning that each will alter the temperature of the spacecraft in a unique way. It appears that switching between modes on the spacecraft causes the relationship between spectral point spread function and temperature to change during certain times of the year.

Evidence for this change is given in Figure 4.11, which displays the orbitally averaged point spread function at 350 nm plotted against the orbitally averaged optics temperature for 2006. The data shown in Figure 4.11, particularly in the eclipse period after the summer solstice, can be broken into smaller sections where the point spread function appears to be nearly linearly related to optics temperature. Between 2006 and 2008 there was an increase in the changing of SMR observation modes as it transitioned from splitting time between aeronomy and astronomy measurements to full time aeronomy measurements. During the after-solstice

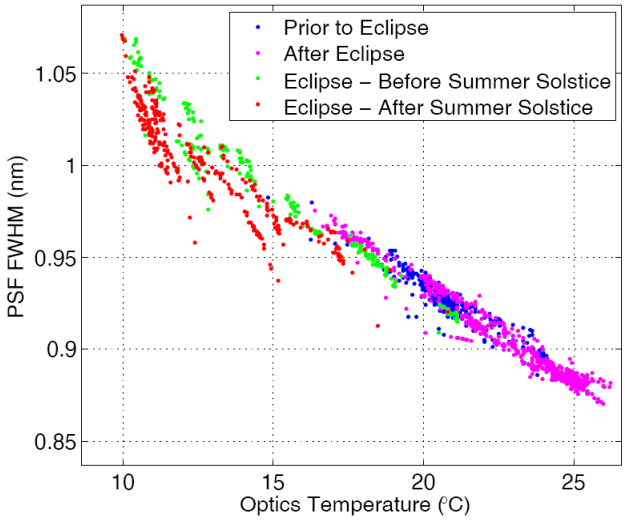

Figure 4.11: The orbitally averaged point spread function FWHM at 350 nm for 2006.

eclipse portion of these years the standard deviation of the difference between the calculated point spread function and the fitted curves shows a noticeable spike (see Figure 4.10). It is possible that during the eclipse period the spectral point spread function is particularly susceptible to sudden changes in temperature caused by the switching of observation modes. If this scenario is true, then the relationship between spectral point spread function and temperature may change slightly every time a power mode switch is made, making the task of finding a single eclipse time relationship between the two impossible.

Further analysis revealed that each noticeable line corresponds to a unique period of time. For each of these periods the point spread function and optics temperature appear linearly related until a sudden rapid change in optics temperature alters that relationship, strengthening the hypothesis that each line resulted from a change in spacecraft observation mode. Unfortunately, information regarding the SMR power modes over time could not be retrieved, limiting the amount of research that could be undertaken on this path.

4.2 Earth's Impact on Satellite Temperature

The work detailed in Section 4.1 led to the conclusion that the optics temperature of the OSIRIS spectrograph and its spectral point spread function are roughly anti-correlated. Un-

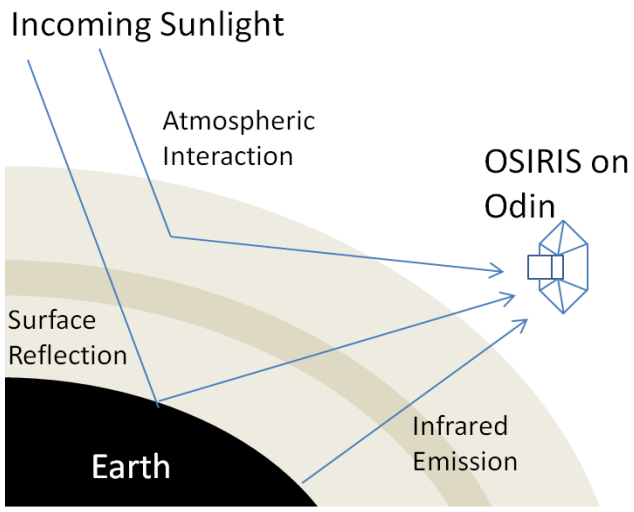

Figure 4.12: Sources of radiation provided by the Earth.

fortunately it was not possible to find a satisfactory relationship between the two variables, even for portions of a single year. Based on these results the decision was made to examine shorter time frames. However, examining time frames shorter than a few months introduces another variable to the situation: terrestrial radiation. The amount of radiation the Earth provides to the Odin satellite fluctuates rapidly, causing its impact to be effectively washed out during long time frame analysis but making it of significant importance for short time frame analysis. Including another source of radiation obviously makes the analysis more complex, but it may reveal new variables which could provide indirect information about temperature gradients within the satellite and allow the successful modelling of the time-dependent spectral point spread function.

4.2.1 Second Order Sources of Radiation

There are three significant ways the Earth provides additional radiation that can be absorbed by the Odin spacecraft, all shown in Figure 4.12: Atmospheric interaction, surface reflection, and infrared emission.

Atmospheric Interaction

Atmospheric interaction is an overarching term that covers all forms of solar radiation interacting with Earth's atmosphere in such a way that results in radiation travelling towards the Odin instrument. At any time approximately 4% of the Earth's atmosphere is visible from Odin's position in space, exposing the spacecraft to additional radiation via atmospheric interaction from the entire sunlit portion of the atmosphere below it. The amount of extra energy provided by atmospheric interaction should therefore be a function of how much of the atmosphere below Odin is bathed in sunlight. Odin's sun-synchronous orbit and 97.8° inclination ensure that the amount of illuminated atmosphere below Odin changes over both the course of the year and the course of an orbit (see Figure 4.1). It is feasible that the change in illuminated atmosphere below Odin over the course of an orbit could yield a change in the radiation flux significant enough to introduce a temperature gradient within Odin and alter the OSIRIS spectrograph spectral point spread function. To investigate this possibility it will be necessary to examine the relationship between satellite position and spectral point spread function.

Surface Reflection

Surface reflection occurs when the solar radiation passing through and interacting with the atmosphere undergoes at least one reflection off of the Earth's surface before it arrives at the Odin instrument. What makes surface reflections unique from other interactions between solar radiation and the atmosphere is the presence of a reflection coefficient, or *albedo*. An albedo of 1 indicates a perfectly reflecting surface, while an albedo of 0 means the surface absorbs any radiation that strikes it. As an equation, it has the form,

$$I_r = aI_0, \tag{4.11}$$

where I_r describes the reflected radiation, a is the albedo and I_0 describes the incident radiation. The albedo of Earth's surface varies widely and depends greatly on the local environment. For example, *Betts and Ball* (1997) found that the thick coniferous tree cover of Canada's boreal forest provides an average summer surface albedo of 0.083, while during

winter a snow covered grass field can yield a mean albedo of 0.75. It is reasonable to expect that the radiation incident on the satellite will increase when orbiting over regions of high albedo such as ice caps and decrease while orbiting over low albedo regions such as forests or oceans. If the change in incident radiation is significant the spectral point spread function may show changes both over the course of an orbit and over a day, with orbital variations being caused by rapid changes in albedo and daily variations brought about when the average albedo gradually changes over the course of several orbits. To determine if the spectral point spread function of OSIRIS is affected by differing levels of surface reflection it will be necessary to examine the point spread function as a function of satellite position, bearing in mind not only the amount of illuminated atmosphere below Odin but also the albedo of the illuminated ground.

Infrared Emission

Like all objects in the universe the Earth emits blackbody radiation described by Planck's law, shown here as a function of absolute temperature T and wavelength λ,

$$B(T,\lambda) = \frac{2hc^2}{\lambda^5}\frac{1}{\exp(\frac{hc}{\lambda k_B T}) - 1} \qquad \left[\frac{\mathrm{W}}{\mathrm{sr}\cdot\mathrm{m}^2\cdot\mathrm{nm}}\right], \tag{4.12}$$

where B is the radiance per unit wavelength, h is Planck's constant, c is the speed of light and k_B is Boltzmann's constant. The temperature of the Earth varies around the globe but has an average temperature of 287 K causing it to radiate primarily in the infrared region of the electromagnetic spectrum. With this in mind it is reasonable to speculate that the Odin spacecraft is exposed to some level of infrared radiation emitted from the Earth. However, the emitted infrared radiation does not simply travel through the atmosphere and into space. Constituents of Earth's atmosphere such as water vapour and carbon dioxide are significant absorbers of infrared radiation and can drastically alter the amount of infrared radiation that escapes to space. The details of such procedures are beyond the scope of this thesis and as such an assumption will temporarily be made that the infrared radiation absorbed by the Odin spacecraft is either minimal or constant enough that it does not affect the spectral point spread function of OSIRIS. If the investigation into the second order sources described above does not yield an improved equation for the OSIRIS spectral point spread function,

then the impact of infrared emission will have to be evaluated in greater detail.

4.2.2 Evidence of Changes Over a Day

Expectations

Potential variations in spectral point spread function over the course of a day were examined first as daily variations should only result from changes in the amount of surface reflection, whereas orbital changes could be the result of changing amounts of surface reflection or atmospheric interaction. Any variations due to surface reflection should be maximized when the solar radiation incident on the ground below Odin is at a maximum, i.e. when the solar zenith angle is at a minimum. The 97.8° inclination of the Odin orbit means that the solar zenith angle for locations below Odin will be at a minimum in the Northern Hemisphere during the Northern Hemisphere summer, as first shown in Figure 4.1. During this time of year the satellite is experiencing eclipse for a portion of its orbit, but over a single day the effects caused by the eclipse should consistently appear in each orbit. Therefore any noticeable changes in spectral point spread function over the course of a day are most likely the result of changes in the amount of surface reflection occurring beneath the Odin satellite.

Evidence In OSIRIS Measurements

Figure 4.13 displays the point spread function of the OSIRIS spectrograph at 350 nm as well as the optics temperature for every scan from June 28, 2008. Each orbit is distinguishable by the noticeable lapse in time between adjacent scans. The date is near the Northern Hemisphere summer solstice and thus the amount of surface reflection occurring beneath the Odin satellite should be at a maximum. It can clearly be seen that both the orbital maximum optics temperature and orbital minimum point spread function vary over the course of the day. The orbital maximum optics temperature shows noticeable peaks at times of 0.35 and 0.95, with a distinct troughs at 0.15 and 0.65. The corresponding troughs and peaks in point spread function can also be clearly seen.

Many plots similar to Figure 4.13 were examined with similar results. Within all of these plots any noticeable change in the orbital minimum spectral point spread function

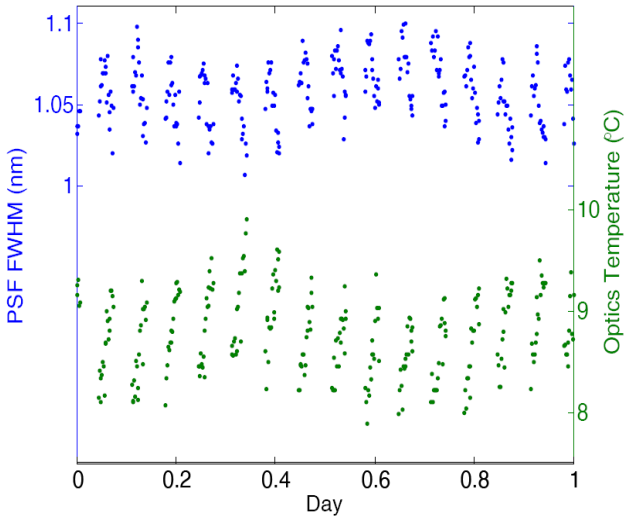

Figure 4.13: The point spread function FWHM at 350 nm and optics temperature for June 28, 2008.

was accompanied by a matching change in the orbital maximum optics temperature. Two conclusions can be drawn from these results. Firstly, as the flux of direct solar radiation on the satellite solar panels should be approximately the same over each orbit, there is clear evidence that a secondary source of radiation, most likely surface reflection, affects the OSIRIS spectral point spread function over the course of a day. Secondly, the results suggest that any change in spectral point spread function over a period greater than one orbit is accompanied by a similar change in optics temperature, meaning that changes over the course of a day were already accounted for in the analysis described in Section 4.1 where optics temperature was the only variable under consideration. Clearly a better understanding of what alters the spectral point spread function will only be found by analyzing spectral point spread function changes that occur over the course of a single orbit.

4.2.3 Evidence of Changes Over an Orbit

Expectations

The 97.8° inclination of Odin's orbit ensures that during every orbit Odin spends approximately half of its time orbiting over sunlit regions of the Earth and the other half orbiting

over areas shrouded in darkness. When Odin transitions from orbiting over darkness to orbiting over illuminated areas the amount of terrestrial radiation it receives greatly increases. It is therefore possible that the increase in radiation may cause short term fluctuations in the temperature of the satellite, leading to temperature gradients within the instruments and changes in spectral point spread function that are not mirrored by changes in optics temperature. Once again, this change should be greatest during the Northern Hemisphere summer months as the amount of solar radiation incident on the Earth below Odin will be at a maximum.

When discussing variations in spectral point spread function over a single orbit the effects of Odin's eclipse behind the Earth during the Northern Hemisphere summer become extremely important. The eclipse has a dramatic effect on the temperature of the spacecraft and as such it is beneficial to look for evidence of satellite position affecting spectral point spread function over a single orbit at two different times, during non-eclipse and during eclipse.

Evidence In OSIRIS Measurements

Non-Eclipse Every orbit consists of approximately 60 scans, each with their own unique spectral point spread function. Figure 4.14 shows the point spread function standard deviation for the scans of every 10th orbit in 2009 for the wavelengths of 313, 320, and 350 nm. As discussed previously, there appears to be a non-zero level of noise within the spectral point spread function values. It was determined in Section 4.1.2 that the error due to this noise would be given as ± 0.020 nm. Therefore if the standard deviation is equal to 0.010 nm then 95% of the point spread functions measured in that orbit are within the ± 0.020 nm of the mean, indicating that the point spread function is essentially constant for that orbit.

During times of non-eclipse the standard deviations of the point spread function at 350 nm has values near or below 0.010 nm, indicating that the point spread function at this wavelength is nearly constant over an orbit. If the position of the satellite does have any effect, it will be minimal. The 313 and 320 nm wavelengths both show point spread function standard deviations greater than 0.010 nm for both eclipse and non-eclipse time periods. Evidently at these wavelengths the point spread function changes over an orbit or the method

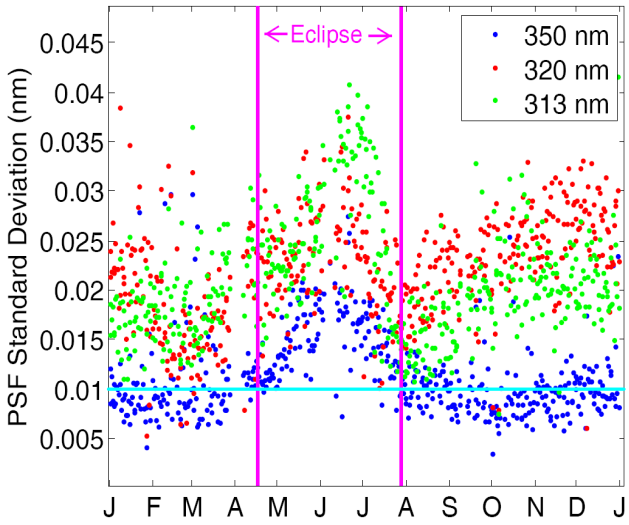

Figure 4.14: The orbital standard deviation of the point spread function FWHM at 313, 320, and 350 nm for every 10th orbit of 2009.

for determining the point spread function inherently has a larger error than at the 350 nm wavelength. It is necessary to look further into the point spread function at these wavelengths during non-eclipse times in order to determine which scenario is more likely.

Figure 4.15 displays the optics temperature and all calculated 313 and 320 nm point spread functions for December 2, 2009, a day where OSIRIS measurements returned typical results but also a day near the time of maximum non-eclipse standard deviation for 320 nm in Figure 4.14. On this day the optics temperature varied by less than 0.3°C over each orbit. Such a variation is much less than what is seen during periods of eclipse, when the optics temperature regularly varies by more than 1°C over an orbit as shown in Figure 4.13. Despite the relatively stable temperature, the point spread function values at 313 and 320 nm display a magnitude of orbital variation similar to that of the 350 nm point spread function during times of eclipse, suggesting other factors may be influencing the values. Also, if one zooms in on the individual orbits of the 320 nm plot as shown in Figure 4.16, a trend in point spread function over the course of a single orbit is immediately apparent. The point spread function begins each orbit by steadily rising until it reaches a peak, then drops steadily for the remainder of the orbit. This trend is not seen in the optics temperature measurements, which confirms what was inferred from the results of Section 4.1.2: the point spread function

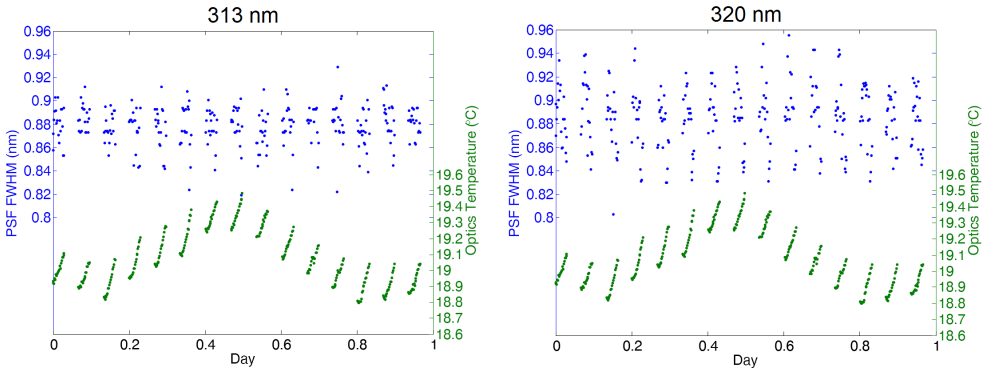

Figure 4.15: All calculated point spread function FWHM values at 313 and 320 nm for December 2, 2009.

is dependent on variables other than just the optics temperature. The fact that there is a distinguishable trend in point spread function over the orbit indicates that satellite position is one of the variables that must be accounted for. Interestingly, a similar trend is not clearly discernible in the 313 nm plot, at least to the human eye. Before making the statement that the 313 nm wavelength is not affected by satellite position, further analysis must be performed.

Eclipse During eclipse the orbital standard deviation of the point spread function for all three wavelengths is greater than 0.010 nm, indicating a change in point spread function over the orbit. Figure 4.17 shows all calculated point spread functions for 313 and 320 nm for June 28, 2008, while the point spread function values for this day at 350 nm are shown in Figure 4.13. All three plots show a trend in the point spread function over a single orbit where the point spread function begins the orbit increasing in value, reaches a peak, and then decreases in value for the rest of the orbit.

As the optics temperature measurements of Figures 4.13 and 4.17 make clear, the thermistor recording the optics temperature is warming as soon as the orbit's measurements begin. However, the spectral point spread function does not immediately begin decreasing, instead following its own pattern that appears to repeat itself every orbit. The most likely cause of this situation is an unmeasured temperature gradient within the OSIRIS spectrograph; it takes a finite amount of time for the additional heat provided by the sun and Earth to equally

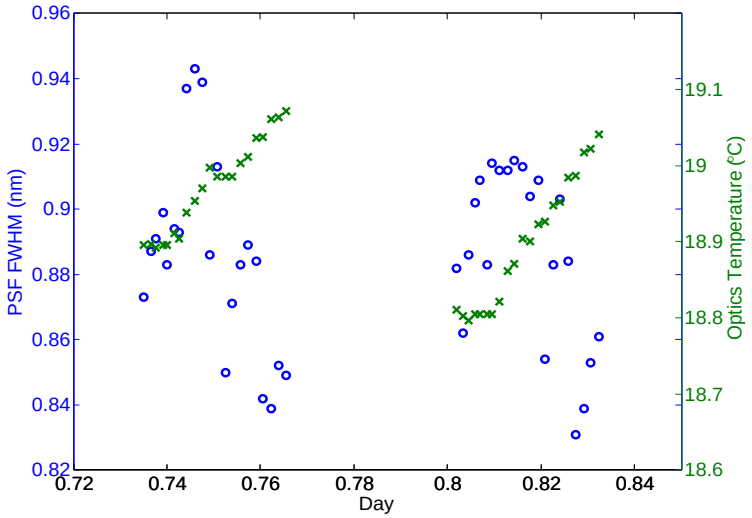

Figure 4.16: A zoomed-in view of two orbits of the 320 nm plot from Figure 4.15, showing changes in point spread function FWHM not mirrored by changes in optics temperature.

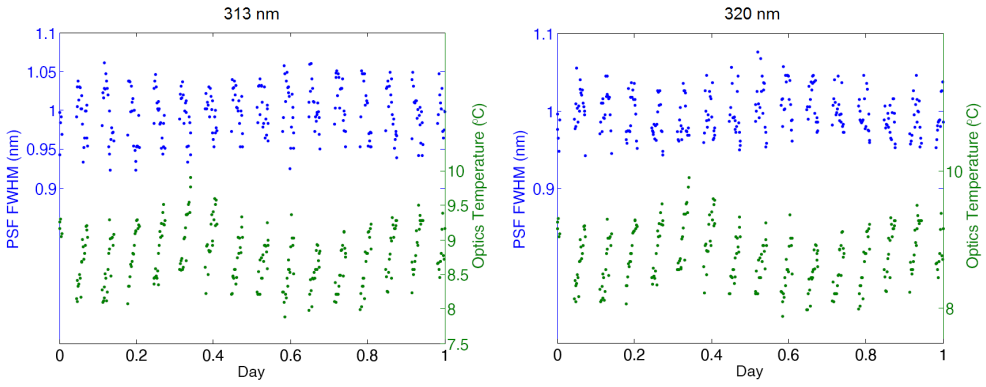

Figure 4.17: All calculated point spread function FWHM values at 313 and 320 nm for June 28, 2008.

distribute throughout the satellite, causing the components of the spectrograph responsible for the point spread function to warm at different rates. These results make it clear that the position of the satellite is an important variable that can provide indirect information regarding temperature gradients when attempting to model the spectral point spread function during times of eclipse.

4.3 Spectral Point Spread Function, Optics Temperature, and Satellite Position

4.3.1 A Suitable Definition of Satellite Position

The results of Section 4.2 justify the attempt to find a relationship between the calculated spectral point spread function and the variables of optics temperature and satellite position. A notable difference between optics temperature and satellite position is that optics temperature is a measured quantity while the position of Odin is dependent on the choice of coordinate system. Choosing an appropriate definition of satellite position is essential if a satisfactory relationship between spectral point spread function, optics temperature, and satellite position is to be found.

Fortunately the position of Odin at any time can be retrieved from computer storage, and code exists to display its position in any one of multiple coordinate systems. One available coordinate system that is particularly suited for easily understanding both the satellite position and the topography of the Earth below it is the orbital plane coordinate system, wherein position is defined by geocentric radius and latitude. The geocentric radius gives the distance from the center of the Earth to Odin and the geocentric latitude, also called the orbit track angle, gives the angular distance from the ascending node in degrees. Odin's orbit is very nearly circular, justifying the assumption that the geocentric radius is a constant. It is also a reasonable assumption to say that Odin's path does not deviate from the set orbital inclination of 97.8°. While in reality the satellite may precess slightly from its set orbital plane, there is no reason to expect the precession to have any noticeable effect as the surface of the Earth beneath the satellite will be almost identical to that directly

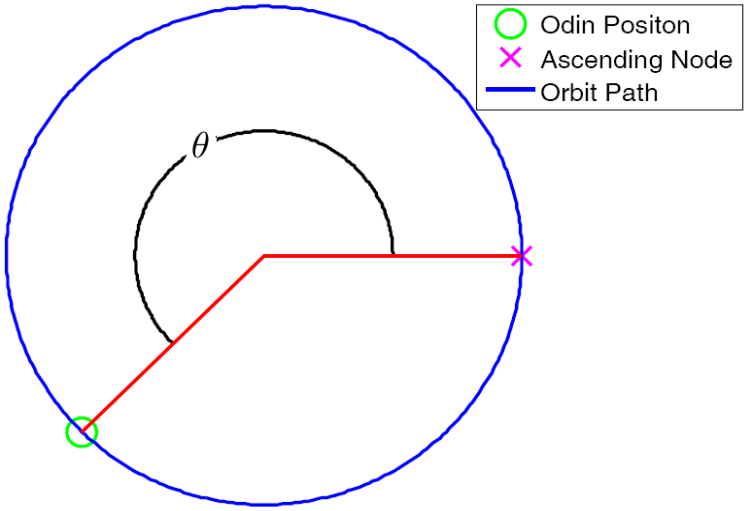

Figure 4.18: Face-on view of the Odin orbit plane showing the orbit track angle θ.

beneath the orbit plane. It is then justifiable to state that the Odin orbit plane is constant throughout an orbit. Therefore, the position of the Odin satellite is fully defined by the orbit track angle, shown in Figure 4.18 as the variable θ.

4.3.2 Finding a Satisfactory Relationship

With the decision made to define the satellite position as the orbit track angle it becomes necessary to try and find a satisfactory relationship between spectral point spread function, optics temperature, and orbit track angle. The conditions and methodology used for this analysis are the same that were used when trying to find a relationship solely between spectral point spread function and optics temperature. Multiple linear regression analysis will be used to determine the best model of the calculated spectral point spread function that can be achieved using optics temperature and satellite track angle as variables. If the scan-by-scan difference between the calculated and modelled spectral point spread functions shows a standard deviation of less than 0.010 nm, then the relationship shall be deemed satisfactory. Once again, the reason for the 0.010 nm standard deviation criteria is to ensure that 95% of all modelled spectral point spread function values fall within $\pm$0.020 nm of the calculated spectral point spread function, as 0.020 nm appears to be the magnitude of the noise observed

in the calculated spectral point spread function.

A New Equation

When attempting to find a relationship between spectral point spread function and optics temperature it was found that the two variables were roughly anti-correlated, but not to a satisfactory level. Therefore, it is reasonable to begin the current analysis by assuming a linear relationship between spectral point spread function and optics temperature and including additional terms to represent the effect of the orbit track angle. The simplest of these equations is given as,

$$\mathrm{PSF}_x(t) = A_1 T(t) + A_2 \sin(\theta(t)) + A_3 \cos(\theta(t)) + A_4, \tag{4.13}$$

where A_{1-4} are coefficients to be determined, T is the optics temperature, θ is the orbit track angle, and t is the time at which these measurements were taken. The variable x denotes the wavelength which the equation corresponds to, either 313, 320, or 350 nm. For all scans within a chosen period (a day, a year, the entire mission, etc.) a single set of coefficients will be found using multiple linear regression analysis, allowing the point spread function of all scans within the chosen period to be modelled by a single equation.

Relationships During Eclipse/Non-Eclipse

It was shown in Section 4.1.2 that over the course of a single year's non-eclipse period the relationship between the point spread function at 350 nm and optics temperature was often very close to satisfactory. Under these conditions the standard deviation of the scan-by-scan difference between calculated and modelled point spread functions routinely approached the target 0.010 nm. It was also only under these conditions that there appeared to be minimal alterations to the point spread function over the course of a single orbit. If the addition of the orbit track angle terms can account for point spread function changes over an orbit, it may be possible to reduce the standard deviation between calculated and modelled point spread functions for all wavelengths and time periods to acceptable levels. With this in mind it was decided an attempt would be made to relate spectral point spread function to

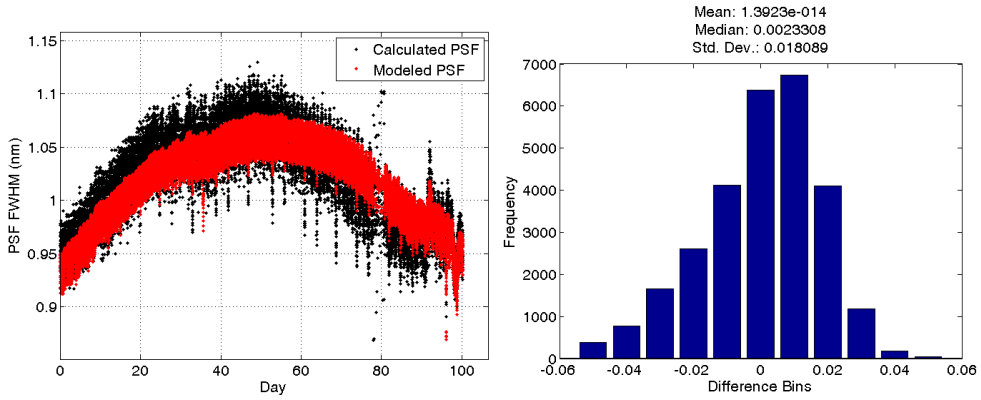

Figure 4.19: Calculated and modelled point spread function FWHMs at 350 nm for the first 100 days of the 2008 eclipse period.

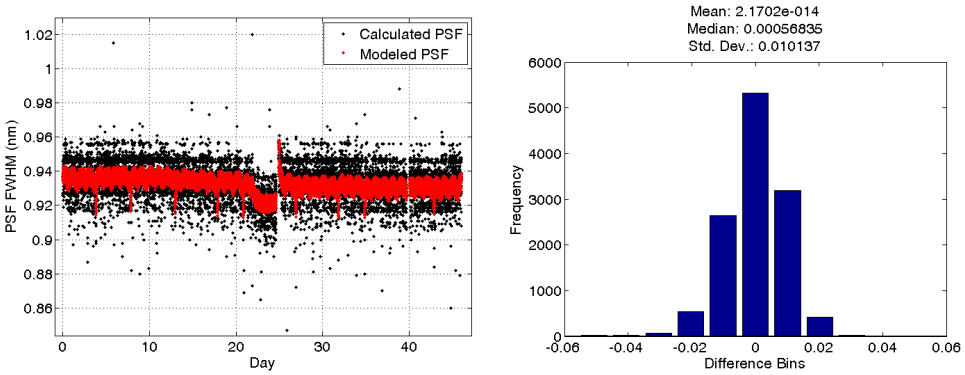

Figure 4.20: Calculated and modelled point spread function FWHMs at 350 nm for the first 50 days of the 2009 non-eclipse period.

optics temperature and orbit track angle over periods defined by the start/end of each eclipse season.

Figures 4.19, 4.20 and 4.21 show, for every scan, the calculated point spread functions as well as the point spread functions modelled using Equation 4.13 with coefficients A_{1-4} determined through multiple linear regression analysis. Figure 4.19 shows this data for the first 100 days of the 2008 eclipse period at 350 nm, Figure 4.20 for the first 50 days of the 2009 non-eclipse period at 350 nm, and Figure 4.21 for the same time frame as Figure 4.20 but at 313 nm. Also shown in Figures 4.19–4.21 are histogram plots indicating how the calculated and modelled point spread functions differ on a scan-by-scan basis. It is important to note

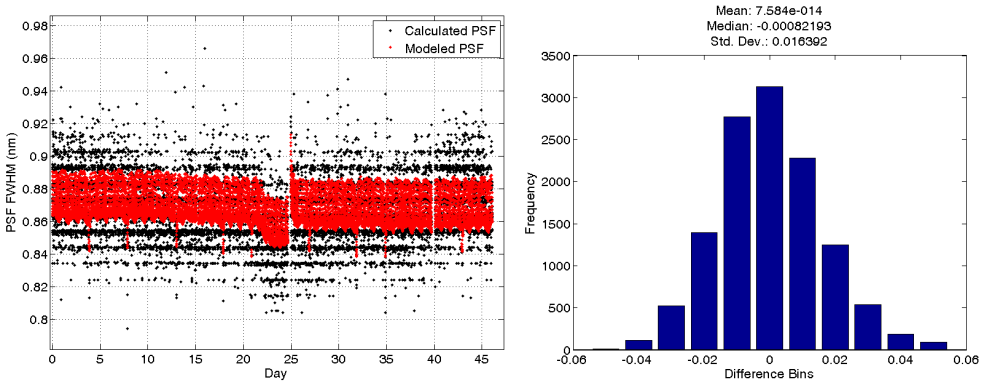

Figure 4.21: Calculated and modelled point spread function FWHMs at 313 nm for the first 50 days of the 2009 non-eclipse period.

that several other years of eclipse and non-eclipse data were also analysed. The results were similar to those shown in Figures 4.19, 4.20 and 4.21, making it redundant to display more than the given examples. It should also be stated that the discontinuity seen at day 25 of Figures 4.20 and 4.21 is likely due to a power mode change in either OSIRIS or the SMR, the instrument that shares Odin with OSIRIS.

Figure 4.19 leaves little doubt that the entire eclipse period of the 350 nm point spread function cannot be modelled with a single equation of the form given in Equation 4.13. The standard deviation of the difference between the modelled and calculated point spread functions is 0.018 nm, much greater than the desired 0.010 nm target. The difference between the modelled and calculated point spread function also clearly changes over time; In the first half of the eclipse period the modelled point spread function is noticeably less than the calculated point spread function, while in the second half of the period the opposite is true.

The results shown in Figure 4.20 are closer to what was desired than those of Figure 4.19. The standard deviation is given as 0.010 nm, just reaching the set goal. The histogram plot shows a much more Gaussian-like structure than that of Figure 4.19, meaning that the model can be seen as a smoothed version of the calculated point spread function. Evidently it is possible to find a satisfactory relationship between point spread function, optics temperature, and orbit track angle during times of non-eclipse at the 350 nm wavelength.

It is clearly not possible to find a similar satisfactory relationship at the 313 nm wavelength

though. The standard deviation given in Figure 4.21 of 0.016 nm is well outside the 0.010 nm goal and the histogram shows a definite skewness, indicating a less than desirable fit. The calculated point spread function at 313 nm evidently behaves differently than the 350 nm point spread function over the same time frame, but at this point the cause of the different behaviour is not the primary concern. The conclusion to be drawn from Figure 4.21 is that the non-eclipse period of the spectral point spread function cannot be modelled by a single equation of the form given in Figure 4.13. As the eclipse periods showed a similar inability to be successfully modelled there are now two possible courses to follow: adjust the length of time over which the point spread function is modelled or alter the equation used for the modelling.

Relationships Over a Day

Given the large number of scans that take place during a single period of eclipse or non-eclipse any short term trends in point spread function were likely washed out. It then makes logical sense to shorten the time that the point spread function is modelled over before changing the equation used to do the modelling. It was therefore decided to use, for each wavelength, a single equation in the form of Equation 4.13 to model the point spread functions of all scans that occurred over the course of 15 orbits, or approximately one day. The period of a day was chosen as it is short enough that any small variations in point spread function can hopefully be modelled, yet not so short that calculating and recording the coefficients for each individual equation becomes computationally cumbersome. The criteria for a successful relationship remains the same: the standard deviation of the difference between the modelled and calculated point spread functions must be less than 0.010 nm.

Figures 4.22 and 4.23 display the calculated and modelled point spread functions at 350 nm for every scan taken on June 17, 2008 and January 7, 2009 respectively. The beginning and end of each orbit is once again marked by a noticeable gap between data points. June 17 is in the heart of the eclipse period while January 7 experiences no eclipse whatsoever. It is clear from these Figures that choosing to model each day with its own unique equation yields much better results than those of the previous section; both days show standard deviations that are below the target of 0.010 nm and histograms that show the desired Gaussian shape.

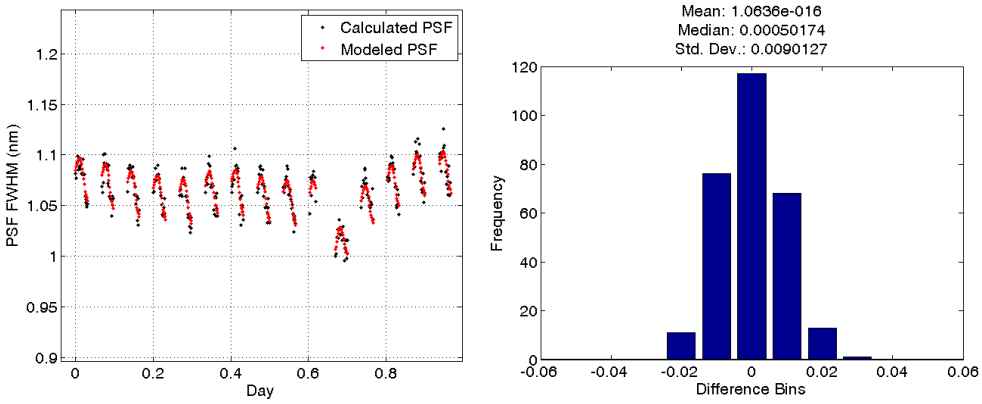

Figure 4.22: Calculated and modelled point spread function FWHM values at 350 nm for June 17, 2008.

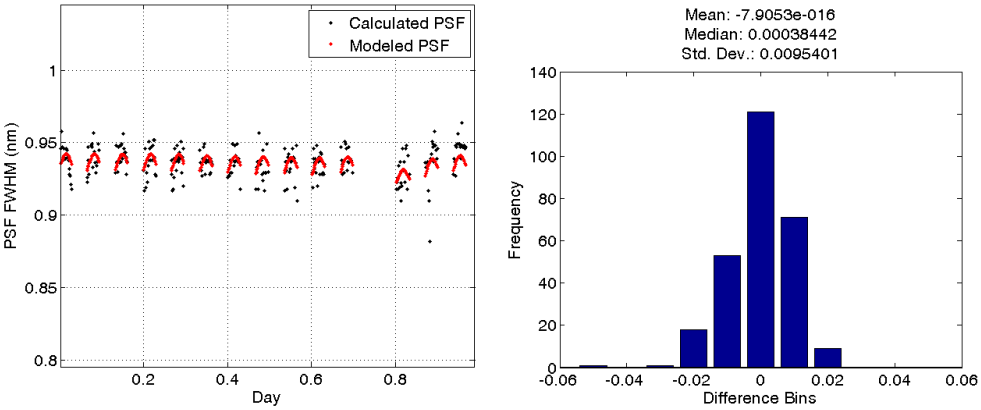

Figure 4.23: Calculated and modelled point spread function FWHM values at 350 nm for January 7, 2009.

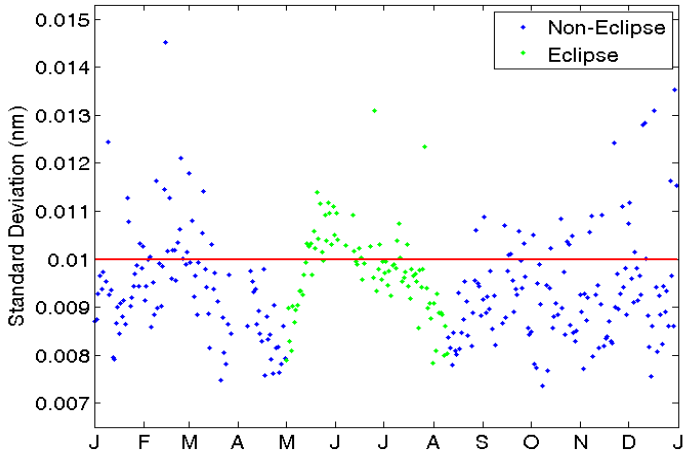

Figure 4.24: The standard deviation of the difference between modelled and calculated point spread function FWHMs at 350 nm for every day of 2009.

To investigate whether the standard deviation during eclipse is routinely lower than the target of 0.010 nm the standard deviation for every day of 2009 was calculated. The results are plotted in Figure 4.24 and show that for the majority of days in 2009 the standard deviation was indeed lower than 0.010 nm, an excellent indication that an equation using optics temperature and orbit track angle as variables can successfully model the point spread function at 350 nm over a period of one day. Applying the same method to other available wavelengths did not yield the same results though. Figure 4.25 shows the standard deviation of the difference for all days in 2009 at the 313 and 320 nm wavelengths. The standard deviation for both wavelengths is clearly larger than the desired 0.010 nm target for all days of the year, and also shows a much more pronounced variation over the year than was observed at the 350 nm wavelength for the same time frame (see Figure 4.24). Analysis of data from other years showed the same results, with the standard deviation rarely reaching the value of 0.010. Evidently the current method works well for the 350 nm wavelength but is insufficient for the 313 and 320 nm wavelengths.

There are multiple potential reasons for the relatively poor performance of the current model at 313 and 320 nm, but determining which is most likely is still not the top priority. At the beginning of this section it was stated that there were two options that could possibly

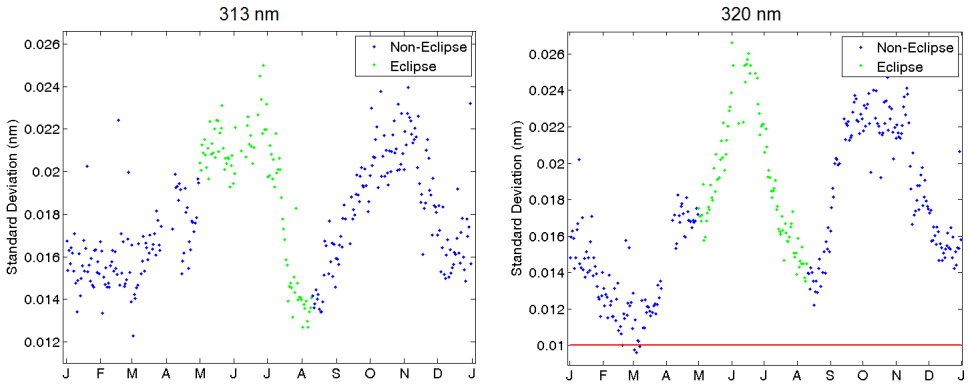

Figure 4.25: The standard deviation of the difference between modelled and calculated point spread function FWHMs at 313 and 320 nm for every day of 2009.

improve the modelling: shortening the period modelled by a single equation or altering the form of the equation. As the modelling period of one day seems to allow successful modelling of any orbital changes in point spread function at the 350 nm wavelength, no further shortening of the modelling period will be undertaken. At this point it is more beneficial to explore alternative forms of the modelling equation.

4.3.3 An Alternative Equation

The first problem to overcome is whether to alter Equation 4.13 by adjusting the optics temperature terms, the orbit track angle terms, or both. To determine this, it is helpful to consider the individual terms of Equation 4.13. Figure 4.26 shows these terms along with the modelled point spread function at 350 nm for the day of June 17, 2008. It is evident in Figure 4.26 that the optics temperature term changes from orbit to orbit, while the sum of the orbit track angle terms appears to be periodic over the course of the day with a period of one orbit.

The modelled and calculated point spread functions for this day are shown in detail in Figure 4.22, where it can be seen that the modelled point spread function falls directly on top of the calculated point spread function for each orbit. This result indicates that the changes in point spread function over multiple orbits, which are only accounted for by the optics temperature term in Equation 4.13, are being well modelled. Also, close examination of

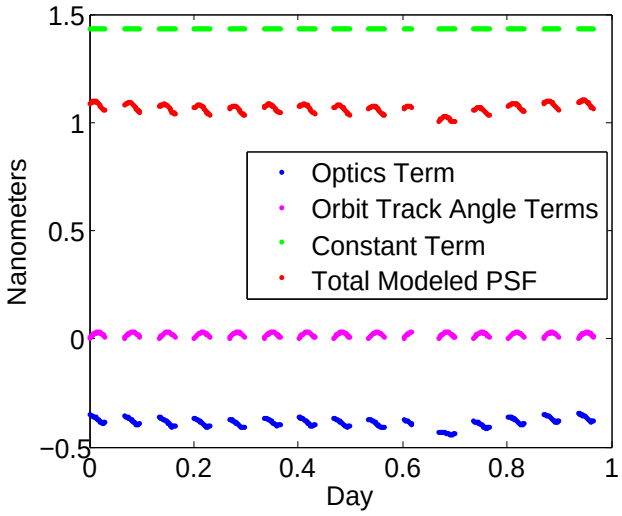

Figure 4.26: The values of the individual terms for Equation 4.13 of June 17, 2008.

Figure 4.22 reveals a trend where in each orbit the peak of the modelled point spread function is lower than the peak of the calculated point spread function. Upon further investigation this trend was consistently observed throughout the OSIRIS mission, leading to the realization that the sum of the orbit track angle terms, which appears to be periodic over the course of a day, may be able to be improved upon. It was therefore decided to leave the optics temperature term intact and explore different options to express the effect of the orbit angle track on spectral point spread function.

Given that the sum of the two orbit track angle terms appears to be periodic over each day, it is possible to consider them as two terms of a Fourier series. In essence a Fourier series is the representation of a periodic signal as the sum of a set of sine and cosine waves. The set can contain any number of sines and cosines with a greater number leading to a more precise representation of the of the periodic signal. Normally, the signal $f(x)$ is known and is modelled using the equation,

$$f(x) = a_0 + \sum_{n=1}^{\infty} \left(a_n \cos(nx) + b_n \sin(nx)\right). \tag{4.14}$$

The goal is then to determine which of the coefficients a_0, a_n and b_n are needed to successfully model the signal. With simplicity in mind, it makes sense to try and minimize the number

of terms added to the model equation. If the two orbit angle terms in Equation 4.13 are considered the first harmonic ($n = 1$) of the Fourier Series, then the simplest addition is to add the second harmonic ($n = 2$) to the equation,

$$\mathrm{PSF}_x(t) = A_1 T(t) + A_2 \sin(\theta(t)) + A_3 \cos(\theta(t)) + A_4 \sin(2\theta(t)) + A_5 \cos(2\theta(t)) + A_6. \quad (4.15)$$

The coefficients of Equation 4.15 were found for each day of the OSIRIS mission using multiple linear regression analysis, creating an entirely new set of equations for modelling the point spread function at the different wavelengths. The results were then analyzed to see if the addition of the second harmonic made a positive impact and to understand if the orbit track angle terms could indeed be treated as a Fourier Series.

Figure 4.27 displays the percentage of days in each year for which the standard deviation of the scan-by-scan difference between the calculated and modelled point spread functions is lower than the indicated values for the wavelength of 350 nm. Evidently treating the orbit track angle as a Fourier Series and including the second harmonic improved the model's fit to the calculated 350 nm point spread function, particularly in the later years of the OSIRIS mission. In 2011 the percentage of days with standard deviations less than the target 0.010 nm went from near 60% with one harmonic to nearly 70% with two harmonics. Observations of scans throughout the mission also confirmed that the orbital peak of modelled point spread function regularly reached the same value as the orbital peak of the calculated point spread function.

As shown in Figure 4.28 the inclusion of the second harmonic led to a significant decrease in the standard deviation of the difference between the modelled and calculated point spread functions at the 313 and 320 nm wavelengths. Although neither wavelength saw a large leap in the percentage of days with standard deviations less than 0.010 nm, both wavelengths saw the percentage of days with standard deviations below 0.015 nm rise as much as 25% while the percentage of days with standard deviations below 0.020 nm rose by as much as 18%. From this result it can be concluded that there are trends in the calculated point spread function that are successfully modelled by the second harmonic. The fact that so few days show standard deviations less than 0.010 nm either means there are more periodic trends

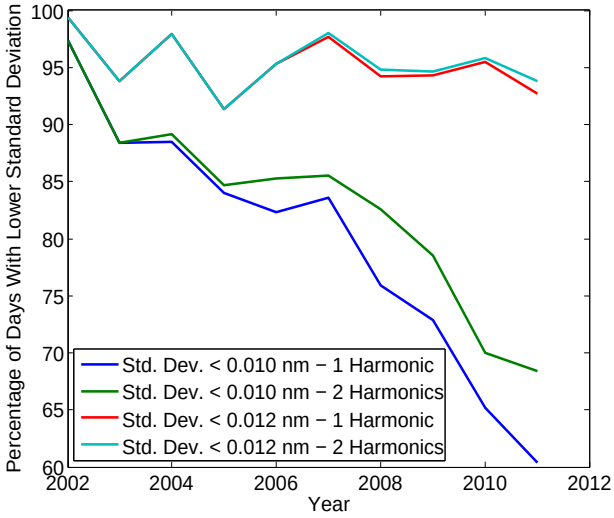

Figure 4.27: The percentage of days each year for which the standard deviation is less than the indicated value for the 350 nm wavelength.

in the calculated point spread function that are not being modelled, or the level of noise at these wavelengths is greater than at the 350 nm wavelength.

To investigate whether this result is due to an increase in noise at these wavelengths or because there are orbital trends that have yet to be modelled, the third harmonic was added to Equation 4.15 and the process described above was repeated. The results are displayed in Figure 4.29, which shows that the addition of the third harmonic slightly improved upon the model that only used two harmonics. The percentage of days with standard deviations below 0.015 and 0.020 nm rose by approximately 5% for both wavelengths, as did the percentage of days with standard deviations below 0.010 nm for the 320 nm wavelength. The percentage of days with standard deviations less than 0.010 nm remained unchanged at 313 nm. The small improvements seem to indicate that the majority of periodic orbital trends in calculated point spread function are accounted for by the first and second harmonics. If other periodic trends are present their effect appears to be minimal, and the difference between modelled and calculated point spread function is likely due to random noise in the calculated point spread function.

It is possible to continue to add harmonics until the majority of days show standard deviations that are less than 0.010 nm. With the use of enough harmonics it would be

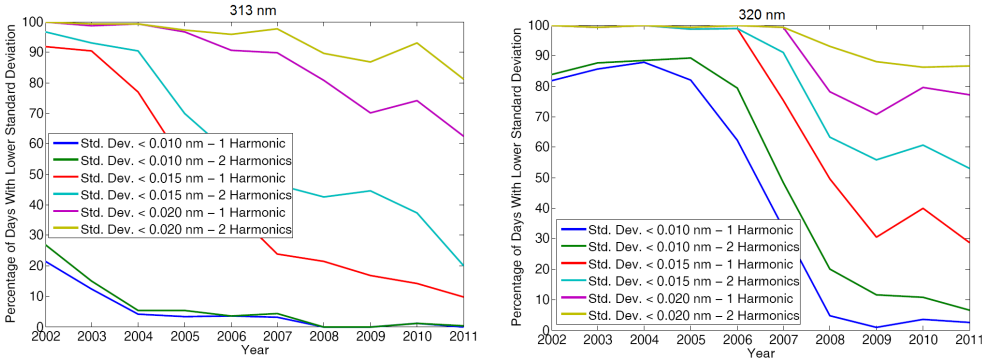

Figure 4.28: The percentage of days each year for which the standard deviation is less than the indicated value for the 313 and 320 nm wavelengths.

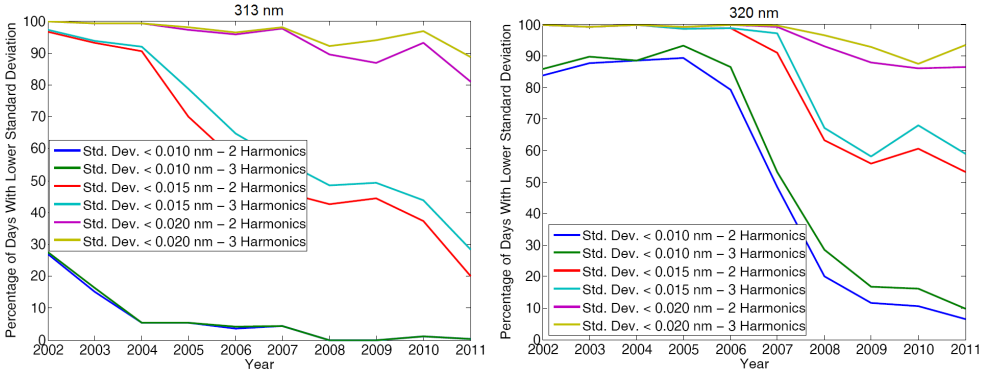

Figure 4.29: The percentage of days each year for which the standard deviation is less than the indicated value for the 313 and 320 nm wavelengths.

possible to create an almost exact replica of the calculated point spread function for any day, but this is not the point of generating the model. The point of the model is to predict the point spread function based on measured data, allowing any noise that is found in the calculated point spread function to be removed. Using the first harmonic allows for orbital trends in the calculated point spread function to be modelled while minimizing the influence of any random noise. As more harmonics are added the resultant model shows less information about the orbital trends and does a better job of fitting to every individual data point, meaning that any noise present in the calculated point spread function becomes increasing present in the modelled point spread function.

With this in mind the decision was made to limit the modelling equation to only the first and second harmonics for all three wavelengths for which point spread functions were calculated. The minimal improvement seen with use of the third harmonic suggests that the amount of noise present in the 313 and 320 nm calculated point spread functions is larger than the amount of noise observed at the 350 nm wavelength. This is an unfortunate result as it means the standard deviation of the difference between the modelled and calculated point spread function will rarely reach the desired goal of 0.010 nm at the 313 and 320 nm wavelengths. However, it is important to state that this result does not indicate a poor model, but rather the opposite. The point spread function modelled using Equation 4.15 has been found to successfully model the calculated point spread function at all investigated wavelengths to the point that it shows the orbital and even sub-orbital variations in point spread function without displaying the noise found in the calculated model. Reducing the difference between the modelled and calculated point spread function would at this point introduce the noise into the model, the exact opposite of what the model was intended to do.

4.3.4 A Final Verification

The first clear evidence of the spectral point spread function varying over time was presented at the beginning of Section 4.1, as Figure 4.5 displayed the changes in the calculated point spread function at wavelengths of 313, 320, and 350 nm over the course of a year. It seems fitting then to examine the calculated and modelled point spread functions over every year as a final verification of the modelling process. Although all years were evaluated, only results

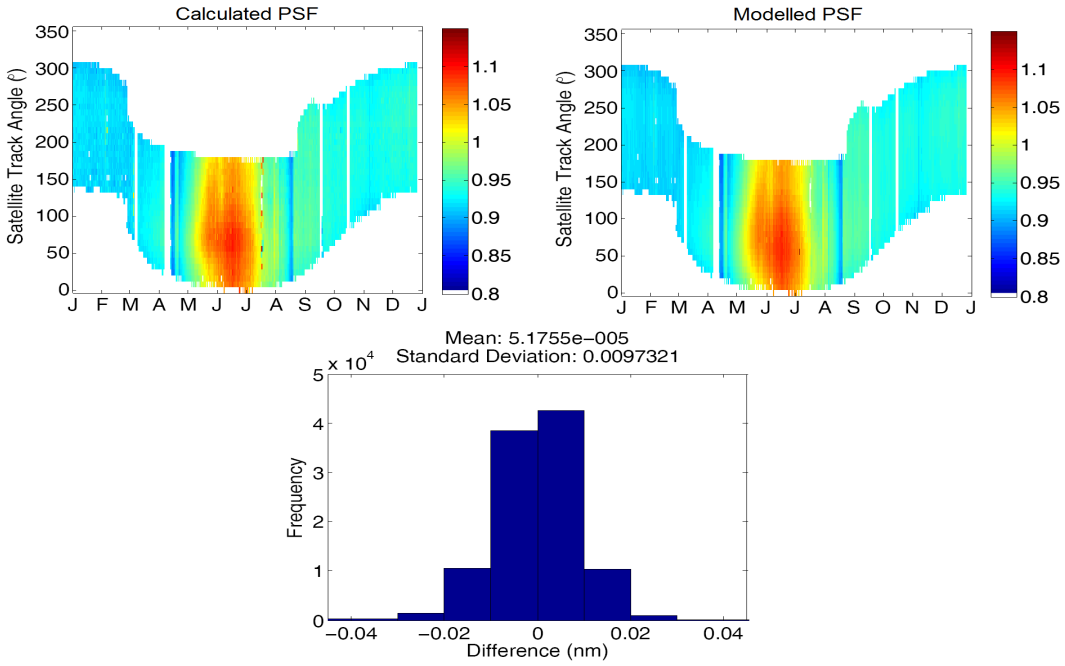

Figure 4.30: The 350 nm calculated and modelled point spread function FWHM values as a function of time and satellite track angle for every scan of 2008. The histogram displays the scan-by-scan behaviour of the difference between the calculated and modelled point FWHM values.

from 2008 are shown as all years showed very similar results. Figure 4.30 shows the calculated and modelled point spread functions for the 350 nm wavelength as a function of time and satellite track angle for all of 2008, while Figures 4.31 and 4.32 show similar results for the 320 and 313 nm wavelengths, respectively. In order to produce these plots all scans from 2008 were organized into bins, one day wide in the time domain and eight degrees wide in the track angle domain. The FWHM values of all scans in each bin were then averaged to create the values shown in the plots. It is apparent from these plots that the calculated and modelled point spread functions are nearly identical for such bin sizes.

Also shown in each of these Figures is a histogram detailing the scan-by-scan difference between the calculated and modelled point spread functions. The standard deviation of the histogram plots are similar to what was observed in previous analysis, with values of approximately 0.010 nm for the 350 nm wavelength and approximately 0.020 nm for the 313 and 320 nm wavelengths. Such similarity, along with the nearly identical calculated and

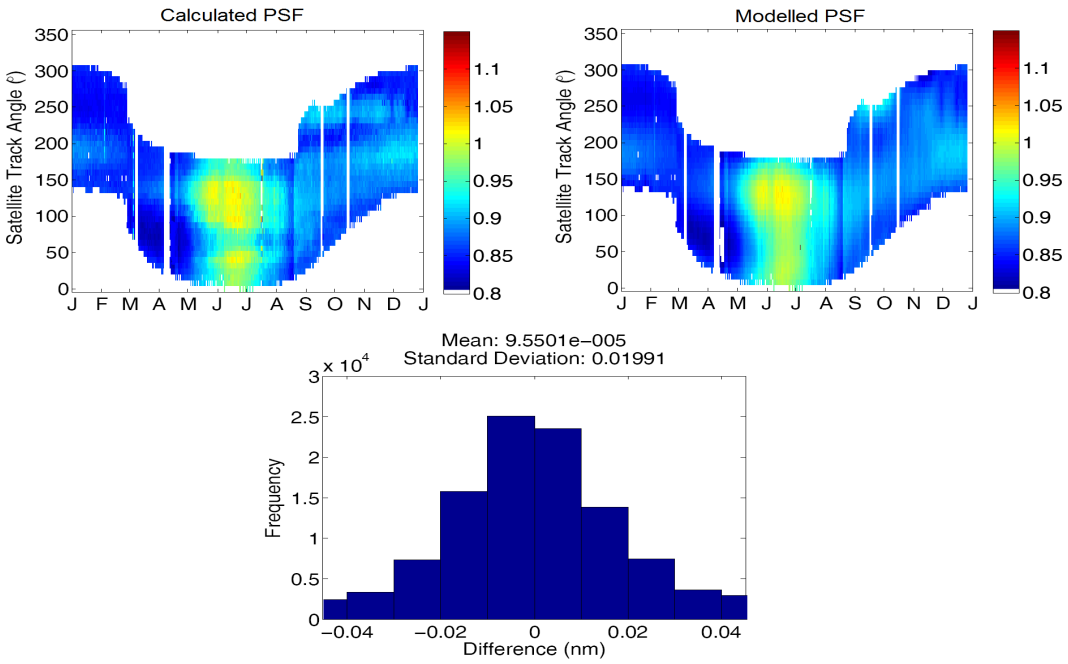

Figure 4.31: The 320 nm calculated and modelled point spread function FWHM values as a function of time and satellite track angle for every scan of 2008. The histogram displays the scan-by-scan behaviour of the difference between the calculated and modelled point FWHM values.

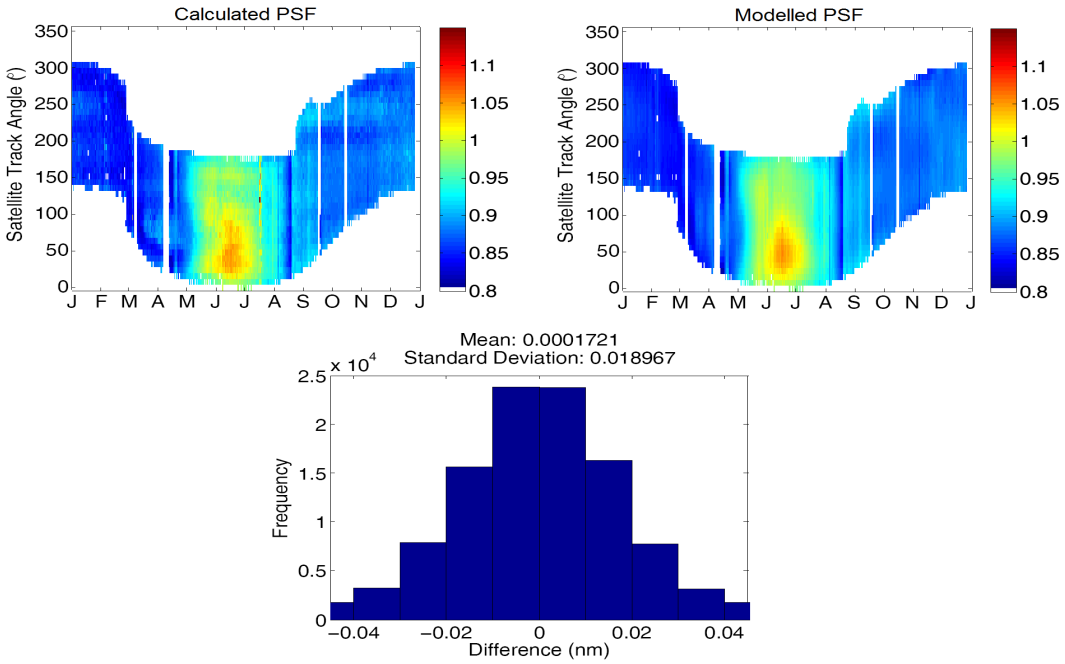

Figure 4.32: The 313 nm calculated and modelled point spread function FWHM values as a function of time and satellite track angle for every scan of 2008. The histogram displays the scan-by-scan behaviour of the difference between the calculated and modelled point FWHM values.

modelled point spread function plots seen for each wavelength, provides the final verification that the calculated point spread function at these three wavelengths can be successfully modelled with Equation 4.15. As a result, the decision was made to implement Equation 4.15 into the algorithms used to model the atmosphere as seen by OSIRIS.

4.3.5 Implementation Into Atmospheric Modelling Algorithms

It is of course still necessary to calculate a point spread function at 350, 320, and 313 nm using the method described in Section 3.2.1 for every scan of the OSIRIS mission before any modelling can be undertaken. An optimized piece of MATLAB code was written that can compute, for a single scan, the point spread function at all three wavelengths in approximately one second. After computation the three point spread functions and other critical scan information are saved in a text file. In a process that took approximately one month this code was used to calculate the point spread functions for every scan in the OSIRIS mission, resulting in a database of point spread function values that can easily be retrieved for modelling purposes. Updating this database is accomplished by simply running the same piece of code, as it is designed to only calculate point spread function values for previously unprocessed scans. With regular updating it will be possible to quickly calculate a time-dependent spectral point spread function for all future OSIRIS scans.

A separate piece of MATLAB code was written to automatically calculate the coefficients necessary for successful modelling of the point spread function at 350, 320, and 313 nm. After opening the database created by the first piece of code, this code locates any days in the OSIRIS mission that have had point spread functions calculated, but not modelled. It then retrieves all necessary optics temperature and satellite track angle data and calculates, using multiple linear regression analysis, the coefficients of Equation 4.15 for all three wavelengths, repeating the process for each day to be modelled. These coefficients are then checked to make sure they produce reasonable results, cleaned if necessary, and saved along with the times for which they are applicable in a text file for further use.

By saving the coefficients in a text file implementation into the atmospheric modelling algorithms is made relatively easy. Code was added that takes the date of the OSIRIS scan being modelled and searches the coefficient file until it finds the coefficients applicable to that

date. These coefficients are then used in Equation 4.15 to calculate the point spread function of the current scan at 350, 320, and 313 nm. Linear interpolations are then performed to create a unique spectral point spread function from 310-350 nm which is used within the model for any necessary calculations, such as being convolved with high resolution ozone cross sections.

4.3.6 Modelling Summary

The partial success in meeting the goal set at the beginning of Section 4.1.2, to have a modelled point spread function whose scan-by-scan difference from the calculated point spread function showed a standard deviation of less than 0.010 nm, only emphasizes the importance of this model. The work in this section revealed that the random noise present in all calculated point spread functions was greater at 313 and 320 nm than at 350 nm, for reasons which are unclear. It is possible that one of the reference Fraunhofer features used to calculate the point spread functions at these wavelengths changed slightly over time or was measured incorrectly in the reference spectrum, leading to differences between the reference spectrum and the spectrum as seen by OSIRIS. It is also possible that an unaccounted for atmospheric interaction affected the Fraunhofer features measured by OSIRIS. Multiple atmospheric interactions are active at the 313 and 320 nm wavelengths. NO_2 and BrO absorb radiation at these wavelengths and were not removed from the OSIRIS signal before calculating point spread functions, while the removal of ozone from the OSIRIS signal may also have left an unwanted trace. The Ring Effect, an atmospheric interaction caused by rotational Raman scattering, is also present at these wavelengths and causes a filling in of Fraunhofer features, something that would have noticeably affected point spread function value.

Whatever the reason, there is noise present in the calculated point spread functions and it is desirable to remove it. By creating a unique equation in the form of Equation 4.15 for each day of the OSIRIS mission, it is possible to remove this noise and successfully model the point spread function at wavelengths of 313, 320, and 350 nm for any scan in the OSIRIS mission history. These modelled point spread functions are then used in linear interpolations to create a modelled time-dependent spectral point spread function in the 310–350 nm wavelength range that can be used when modelling the atmosphere as observed

by OSIRIS.

4.4 Summary

In this Chapter a thorough exploration of the relationship between the calculated spectral point spread function, OSIRIS optics temperature, and satellite track angle was undertaken. The goal was to find a suitable method to model the calculated spectral point spread function using these measured parameters in order to verify the validity of the spectral point spread function and reduce the noise observed in its calculation. It was found that a successful model of the calculated spectral point spread function could be achieved for wavelengths of 313, 320, and 350 nm by developing, for each day of the OSIRIS mission, unique coefficients for Equation 4.15, which uses optics temperature and satellite track position as variables. The success of the modelled spectral point spread function led to the development of optimized computer code designed to quickly calculate the modelling coefficients for all current and future OSIRIS measurements and store them in an easily retrievable fashion. The modelled spectral point spread function was then implemented into the algorithms used to model the atmosphere as seen by OSIRIS, making it possible to evaluate the impact such an addition has on retrieved OSIRIS ozone profiles.

Chapter 5

Impact of the Time-Dependent Spectral Point Spread Function

The addition of the time-dependent spectral point spread function to the algorithms used to model OSIRIS observations will introduce significant changes at two points in the process of OSIRIS ozone retrieval. Firstly, the significant structure seen in the Hartley and Huggins bands of the ozone cross section will cause these bands to show noticeably different values depending on whether they are convolved with the time-independent or time-dependent spectral point spread function. Secondly, the differences introduced into these convolved ozone cross sections will lead to changes in the retrieved ozone profiles. Investigating and understanding the impact that the time-dependent spectral point spread function has on both the convolved cross sections and retrieved ozone profiles is necessary to confirm that it actually improves the models of the atmosphere as seen by OSIRIS.

5.1 Impact on Convolved Ozone Cross Sections

With the methods for developing and modelling the time-dependent spectral point spread function completed, it becomes necessary to evaluate what affect this new spectral point spread function will have when it is convolved with the various ozone cross sections of the ACSO initiative. As discussed previously, these cross sections must be convolved with the OSIRIS spectral point spread function before being implemented in the ozone retrieval algorithms. The use of a time-independent spectral point spread function in this convolution appears to introduce systematic errors into the resultant cross section, errors which reduce the accuracy of ozone profile retrievals and make it difficult to compare the impact of using

different ACSO cross sections within the retrieval algorithms. The newly developed time-dependent spectral point spread function should reduce these systematic errors and produce notably different OSIRIS-resolution convolved cross sections. Verifying that the cross sections convolved with the time-dependent spectral point spread function do indeed differ from those convolved with its time-independent counterpart provides a quick and simple test to verify that implementing the time-dependent spectral point spread function into the retrieval algorithms will likely provide improved ozone profiles.

5.1.1 Choice of ACSO Cross Sections to Evaluate

The ACSO study provided six sets of ozone cross sections for comparison, each recorded by a different research team. While all provided cross sections are of extremely high calibre, over time the data published by *Brion et al.* (1998), hereafter called the DBM cross section, along with the data produced but not yet published by Serdyuchenko, hereafter called the Serdyuchenko cross section, emerged as the frontrunners to be named the standard (Both of these cross sections were introduced in detail in Section 2.6.2). Both of these data sets were measured at the extremely high resolution of 0.010 nm and provide superior wavelength coverage relative to the other available cross sections. When a full report is prepared for the ACSO study regarding the impact of the different cross sections on the OSIRIS ozone profiles it will be necessary to evaluate all provided cross sections, but to simplify the analysis for this thesis only the DBM and Serdyuchenko cross sections will be evaluated at this time.

5.1.2 Analysis of Convolved Cross Sections

Figure 5.1 shows the Hartley and Huggins bands of the high resolution DBM cross section. There is obvious structure to the cross section in these bands, a situation that makes the cross section sensitive to convolution. As previously discussed in Section 2.6.3, convolving the ozone cross section with various Gaussian curves produces different results for the wavelengths of the Hartley and Huggins bands, while identical results are seen at all other OSIRIS wavelengths. Thus the Hartley and Huggins wavelengths are the most likely to be affected by any changes in the spectral point spread function of OSIRIS.

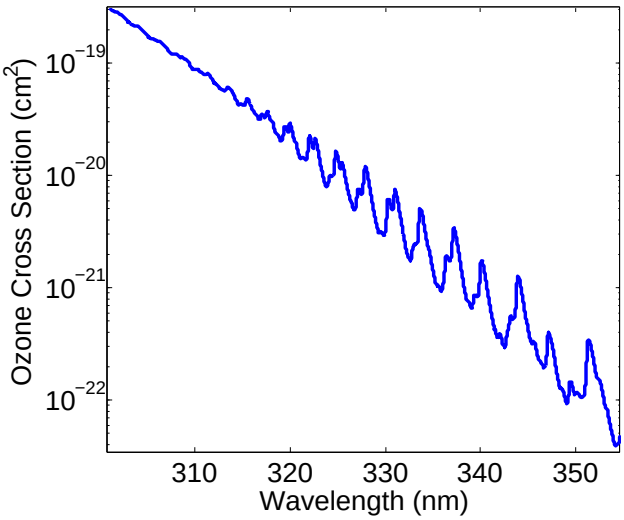

Figure 5.1: The Hartley and Huggins bands of the ozone cross section.

To determine whether the use of the time dependent spectral point spread function had any effect on the convolved cross sections, the DBM and Serdyuchenko cross sections were convolved with both the time-dependent and time-independent spectral point spread functions. It was found that convolving the cross section with the time-dependent spectral point function did indeed produce unique results. Figure 5.2, which shows the absolute percent difference between the time-independent and time-dependent convolved DBM cross sections, verifies this statement by displaying that the use of the time-dependent spectral point spread function can introduce absolute percent differences of over 1.5% for wavelengths in the Hartley and Huggins bands. With these results it is reasonable to speculate that the OSIRIS ozone profiles, which are retrieved in a process that makes use of the convolved ozone cross section, will also be impacted by the use of the time-dependent spectral point spread function.

At this point it is important to establish an approximate sense of how much change in ozone profile value should be expected when the different ozone cross sections are used alongside the time-dependent spectral point spread function in the OSIRIS ozone retrievals. Having an idea of what changes to expect due to differing cross sections will help to isolate profile changes caused by the introduction of the time-dependent spectral point spread function, and also verify that systematic errors introduced by convolving the cross sections with the time-dependent spectral point spread function have been minimized. Recall from Section

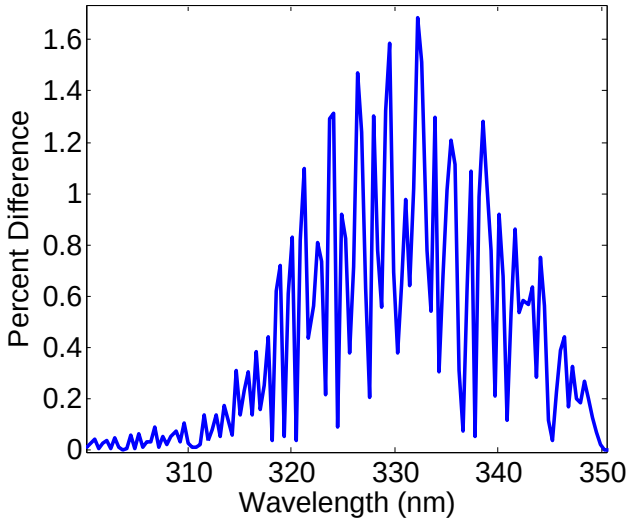

Figure 5.2: The absolute percent difference between two convolved cross sections: DBM convolved with the time-independent spectral point spread function and DBM convolved with the time-dependent spectral point spread function for a scan from June 28, 2003.

2.6.3 that when 196 ozone profiles were retrieved using the time-independent spectral point spread function and one of the DBM, Serdyuchenko, or SCIAMACHY cross sections, significant discrepancies were observed. When compared against the coincident ozone profiles of the SAGE II instrument, the profiles retrieved with the default SCIAMACHY cross section showed a mean percent difference of less than 2%, while the profiles retrieved with the DBM and Serdyuchenko cross sections showed a mean percent difference that peaked at 10%. If these discrepancies are not observed in profiles retrieved with the time-dependent spectral point spread function, it can safely be stated that the systematic errors have been reduced to negligible levels.

To this end, the same sample set of 196 OSIRIS ozone profiles were retrieved using the time-dependent spectral point spread function and each of the three different cross sections. By using the time-dependent spectral point spread function any changes in the retrieved profiles can only be attributed to the use of the different cross sections. The profiles retrieved using the DBM and Serdyuchenko cross sections had their percent differences from the retrieved default profile calculated for each of the 196 profiles, after which the mean and standard deviation of these percent differences were computed. The results are shown as

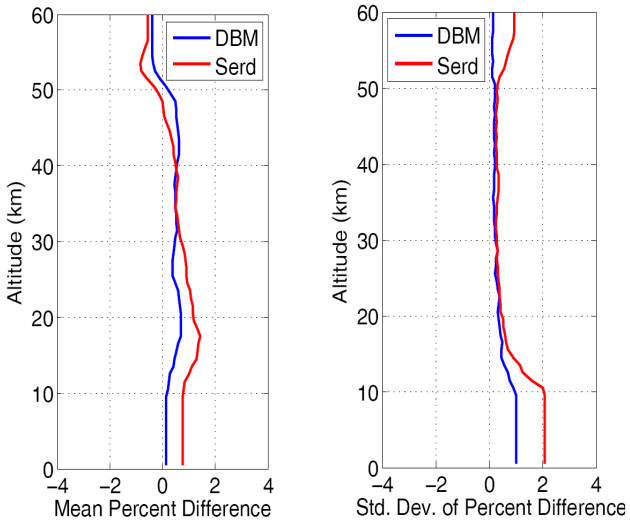

Figure 5.3: The mean and standard deviation of the percent difference profiles found when comparing the DBM and Serdychenko profiles to those of the default.

function of altitude in Figure 5.3, where it can clearly be seen that introducing either the DBM or Serdyuchenko cross section into the retrieval algorithm consistently increases the retrieved ozone number density by 0.5-1.0% in the 20-50 km altitude range, a result that is consistent with the findings from other research groups of the ACSO Commission which were presented early in 2013. It can therefore be stated with confidence that the systematic errors introduced into models of the OSIRIS-observed atmosphere by convolving these cross sections with the time-independent spectral point spread function have been minimized. Also, because the use of either cross section should alter the retrieved profiles by no more than 1% from what would be calculated with the default cross section in the 20 to 50 km altitude range, any percent changes greater than 1% can be attributed to the use of the time-dependent spectral point spread function within the retrievals regardless of which cross section is used.

5.2 Impact on OSIRIS Ozone Retrievals

5.2.1 Scans Comparable With SAGE II Data

When analyzing the impact that the time-dependent spectral point spread function has on OSIRIS ozone retrievals it is not enough to merely compare the profiles retrieved with the time-independent and time-dependent spectral point spread functions; it is necessary to have an unchanging third source of information to determine whether the changes improve or worsen the retrieved profile. To this end, ozone profiles retrieved from NASA's SAGE II instrument, active from 1984 to 2006 (*McCormick*, 1987), were retrieved and interpolated to the OSIRIS altitude grid (an array of tangent altitudes that ranges from 0.5 km to 99.5 km in 1.0 km increments) for comparison against OSIRIS profiles. As the SAGE II ozone profiles are considered the gold standard of ozone profiles any changes in OSIRIS ozone profiles shall be deemed positive if the difference between OSIRIS and SAGE II profiles is reduced, and negative should the opposite occur.

Comparison between OSIRIS and SAGE II ozone profiles can only occur if the measurements of the respective instruments occurred at approximately the same time and location. The coincidence criteria for this were that the measurements occurred within 24 hours, 1 degree latitude, and 1000 km of one another. 1591 instances of measurements that fit this criteria were found, and fortunately the instances were spread nearly uniformly over both time and location.

5.2.2 Ozone Profiles Retrieved With The Time-Independent Spectral Point Spread Function

Before exploring the impact of the time-dependent spectral point spread function it is important to re-establish the current standard of OSIRIS ozone profiles which are retrieved using the time-independent spectral point spread function, a standard first discussed in Section 2.5.5. Figure 5.4 displays four examples of current OSIRIS and SAGE II ozone profiles with the number density of ozone plotted as a function of altitude. Two of the profiles are from periods of eclipse while two are from non-eclipse periods, with the eclipse period being de-

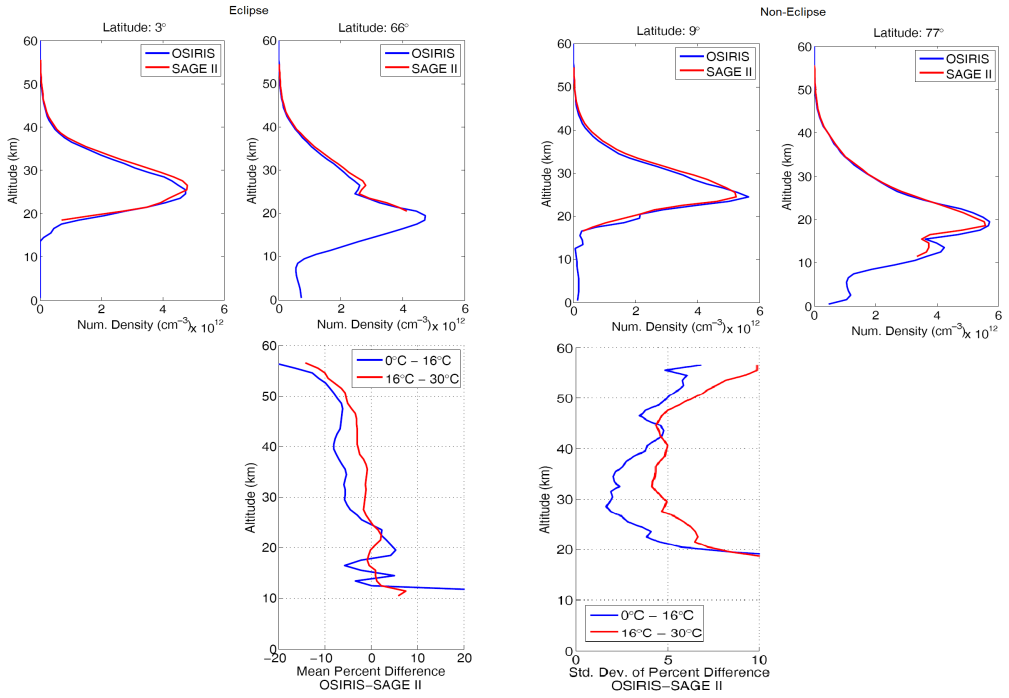

Figure 5.4: Four sample ozone profiles along with the mean and standard deviation of the percent difference between SAGE II and OSIRIS ozone profiles for eclipse and non-eclipse. OSIRIS profiles calculated with the time-independent spectral point spread function.

fined here as the times when the optics temperature is less than 16°C. At first glance the profiles in each of the four plots appear quite well correlated. Also displayed in Figure 5.4 is the mean and standard deviation of the percent difference between all current OSIRIS and SAGE II ozone profiles during times of eclipse and non-eclipse. It is clear from the mean percent difference that while the current ozone profiles of OSIRIS compare quite well with the SAGE II profiles during times of non-eclipse, they deviate significantly during times of eclipse. Evidently there are systematic errors being introduced into the retrieval algorithm during eclipse times, a situation that the use of a time-dependent spectral point spread function will hopefully be able to remedy.

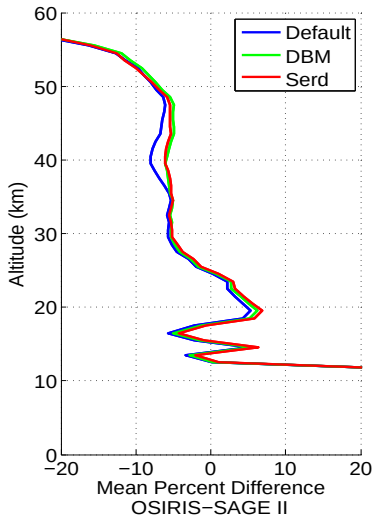

Figure 5.5: The mean percent difference between SAGE II and OSIRIS ozone profiles during OSIRIS eclipse times. DBM and Serdyuchenko profiles computed using the time-dependent spectral point spread function.

5.2.3 Impact During Eclipse

Figure 5.5 displays, as a function of altitude, the mean percent difference between SAGE II and OSIRIS ozone profiles for all coincident eclipse measurements. Three mean percent different curves are displayed, each corresponding to the use of a different cross section in the retrievals. The default curve represents ozone profiles retrieved using the default SCIAMACHY cross section convolved with the time-independent spectral point spread function, while the other curves represent ozone profiles retrieved using the time-dependent spectral point spread function and either the DBM or Serdyuchenko cross section.

Many conclusions can be drawn from Figure 5.5. It is apparent that the use of the DBM and Serdyuchenko cross sections within the retrievals results in ozone profiles that are remarkably similar; the maximum difference of the two mean percent value curves is less than 0.6%, a result which is consistent with the findings of Section 5.1.2. Therefore, the significant changes seen in Figure 5.5 should only be the result of implementing the time-dependent spectral point spread function into the retrieval algorithms.

The most significant change displayed in Figure 5.5 occurs between the altitudes of 35–48 km. At these altitudes the mean percent difference between SAGE II and OSIRIS ozone

profiles is noticeably improved when OSIRIS ozone profiles are retrieved using the time-dependent spectral point spread function. The greatest improvement is seen at 40 km altitude where the mean percent difference decreases by 2%. While encouraging, these improvements nonetheless fall short of validating the hope that the use of the time-dependent spectral point spread function within ozone retrievals would reduce the eclipse time mean percent difference to negligible levels. The fact that there is essentially no change in mean percent difference below 35 km altitude is also discouraging, and indicates that either the large mean percent difference is caused by something other than changes in the spectral point spread function, or that there is a flaw in the time-dependent spectral point spread function.

5.2.4 Impact During Non-Eclipse

Investigating whether the time-dependent spectral point spread function has any impact on ozone retrievals during times of non-eclipse may help unravel whether or not there is a flaw in the time-dependent spectral point spread function. As shown in Figure 5.4, during these times the mean percent difference between SAGE II and OSIRIS ozone profiles, with the OSIRIS profiles being retrieved with the time-independent spectral point spread function, is no greater than 3% from 18–48 km altitude. Nonetheless, it is still possible that implementing the time-dependent spectral point spread function could improve upon these values.

In a similar manner to Figure 5.5, Figure 5.6 displays the mean percent difference between SAGE II and OSIRIS ozone profiles for all coincident non-eclipse measurements. Once again, the default curve represents ozone profiles retrieved using the default SCIAMACHY cross section convolved with the time-independent spectral point spread function, while the other curves represent ozone profiles retrieved using the time-dependent spectral point spread function and either the DBM or Serdyuchenko cross section.

A significant improvement in the mean percent difference is observed in the 35-48 km altitude range, with the mean percent difference values approaching zero. These results are mildly surprising; it was expected that because the mean percent difference between the OSIRIS and SAGE II profiles was much smaller during times of non-eclipse, any impact due to including the time-dependent spectral point spread function would be corresponding smaller. Instead, the time-dependent spectral point spread function profiles of non-eclipse times show

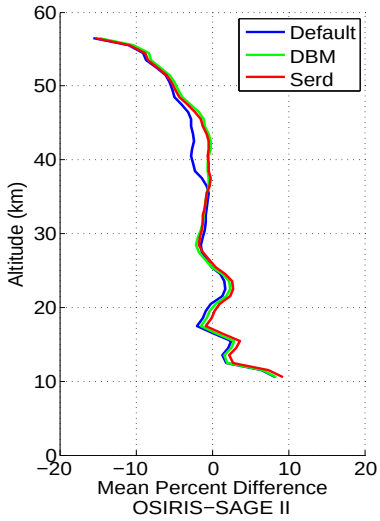

Figure 5.6: The mean percent difference between SAGE II and OSIRIS ozone profiles during OSIRIS non-eclipse times. DBM and Serdyuchenko profiles computed using the time-dependent spectral point spread function.

a mean improvement of almost 2% at 40 km altitude, similar to what was observed for ozone profiles of eclipse times. On one hand, this is a welcome result as reducing the mean percent difference between OSIRIS and SAGE II ozone profiles indicates an improvement to the OSIRIS ozone profiles. However, the unexpected magnitude of the improvement warrants an investigation into its cause. Also, no significant changes were seen below 35 km, leaving the problem of why the OSIRIS eclipse-time ozone profiles deviate so much from their coincident SAGE II profiles yet to be solved.

5.2.5 Changes in Spectral Point Spread Function

The fact that the non-eclipse and eclipse time OSIRIS ozone profiles show nearly the same amount of improvement when the time-dependent spectral point spread function is implemented necessitates examining the values of the spectral point spread function during these two time periods. Specifically, it is necessary to examine the changes between the time-dependent and time-independent spectral point spread functions in order to get a sense of when the maximum impact should be occurring.

The mean FWHM values of the spectral point spread function for coincident OSIRIS and

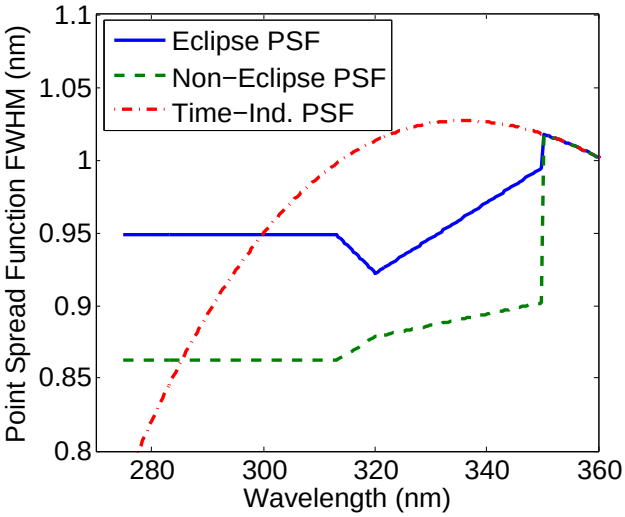

Figure 5.7: The mean values of the spectral point spread function during times of eclipse and non-eclipse for coincident OSIRIS and SAGE II measurements.

SAGE II measurements are shown as a function of wavelength in Figure 5.7 for both eclipse and non-eclipse periods, along with the time-independent spectral point spread function. It is obvious from Figure 5.7 the mean spectral point spread function during eclipse is closer to the time-independent spectral point spread function than it's non-eclipse counterpart. By this observation the introduction of the time-dependent spectral point spread function should lead to greater changes in the ozone profiles during times of non-eclipse. However, it must be remembered that during periods of eclipse the spectral point spread function shows increased variation over the course of a single orbit, often varying by over 5% (see Figure 4.13 for an example). It is possible that the improvements to the retrieved ozone profiles during eclipse times are caused by the combined effect of bringing the spectral point spread function to its proper value and accommodating for the increased orbital variation. To suggest that the total impact of this combined effect could be similar in magnitude to the impact the time-dependent spectral point spread function has during times of non-eclipse is not unreasonable. Verifying this statement would require a scan-by-scan analysis of the spectral point spread functions and their resulting ozone profiles, a time-intensive process that was deemed unnecessary given the positive results of implementing the time-dependent spectral point spread function into the ozone retrievals and the still present problem of the

OSIRIS ozone profiles deviating from those of SAGE II during times of eclipse.

5.2.6 Altitude Shifting

As the Odin satellite orbits the Earth it constantly nods up and down, allowing the OSIRIS instrument to take measurements at tangent altitudes that typically range from 10 to 70 km. Up until this point it has been assumed that the recorded tangent altitude of each measurement was correct. However, the work of this thesis has shown that the optical components of the OSIRIS spectrograph are impacted by temperature gradients within the satellite. It is therefore plausible that the components of the satellite responsible for controlling its orientation are also sensitive to changes in satellite temperature, possibly causing a discrepancy between the OSIRIS line of sight and the line of sight calculated from the satellite's position in space. If the OSIRIS instrument is not actually looking where it is calculated to be looking, then the retrieval of ozone profiles will suffer. For example, consider the situation of retrieving the ozone number density for the 40.0 km tangent altitude. If the OSIRIS line of sight was calculated to have a tangent altitude of 40.0 km but in actuality the line of sight's tangent altitude was 40.5 km, then the ozone number density retrieved for 40.0 km will have been completed with data from 40.5 km, effectively shifting the retrieved ozone number density downward in altitude by 0.5 km.

To determine if such a situation exists a series of tests were undertaken wherein the OSIRIS ozone profiles retrieved with the Serdyuchenko cross section were assumed to be shifted in altitude by a set amount. These ozone profiles were then interpolated to the altitudes of the OSIRIS altitude grid in order to be compared with the SAGE II profiles. An example of these assumed altitude shifts is seen in Figure 5.8, which shows a single retrieved ozone profile in the 22–30 km altitude range shifted by various amounts. The blue line is the unshifted ozone profile, with number densities calculated for altitudes on the OSIRIS altitude grid. The other four lines are simply the blue profile shifted in altitude by the indicated amount. They assume the actual OSIRIS tangent point is offset from the calculated value by the shifted amount and must be interpolated to the OSIRIS altitude grid before they can be compared to the SAGE II profiles.

If an altitude shift is present in OSIRIS measurements during times of eclipse then one

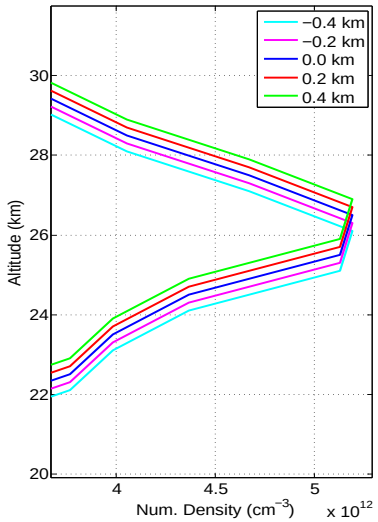

Figure 5.8: A single retrieved ozone profile displaying examples of assumed altitude shifts.

of the altitude shifted profiles should consistently compare better with the SAGE II profiles than the unshifted profiles. In order to establish that there is no altitude shift during times of non-eclipse, the mean percent difference between all non-eclipse OSIRIS and SAGE II profiles was computed for OSIRIS altitude shifts of -0.4, -0.2, 0.0, 0.2, and 0.4 km. The results are shown as a function of altitude in Figure 5.9, and it is clear that the unshifted OSIRIS profiles show the best agreement with the SAGE II profiles at nearly all altitudes. With these results it can safely be stated that there is no evidence of altitude shifting in the OSIRIS profiles during times of non-eclipse.

The process of calculating the mean percent difference between SAGE II and altitude shifted OSIRIS profiles was then repeated using only profiles from times of eclipse. The results for all altitudes are shown in Figure 5.10, where it is clear that altitude shifted OSIRIS ozone profiles provide significant improvements. In the 18-48 km altitude range the absolute mean percent difference can be reduced from 5-6% to less than 2% by shifting the altitude of the OSIRIS measurements by 0.4 km. Thus there is sufficient evidence to suggest that during times of eclipse the decreased satellite temperature causes structural changes which impact the orientation of the satellite, causing the OSIRIS line of sight and tangent point to actually be approximately 0.4 km above what is expected.

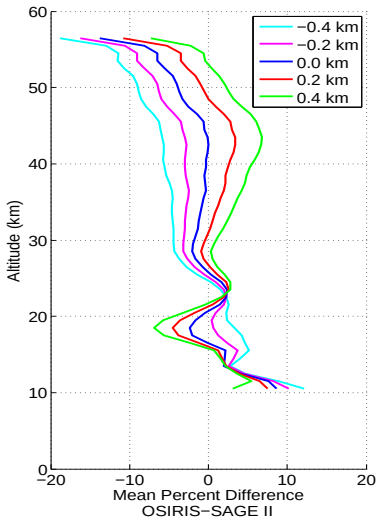

Figure 5.9: The mean percent difference for all non-eclipse coincident OSIRIS and SAGE II ozone profiles. OSIRIS profiles were shifted in altitude by the indicated amount.

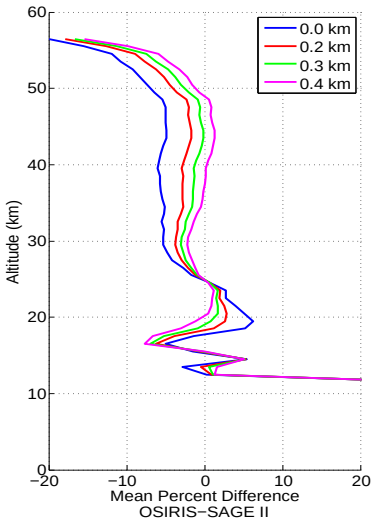

Figure 5.10: The mean percent difference for all eclipse coincident OSIRIS and SAGE II ozone profiles. OSIRIS profiles were shifted in altitude by the indicated amount.

5.2.7 Summary

It was initially speculated that the large discrepancy seen between OSIRIS and SAGE II ozone profiles during times of eclipse was solely a result of systematic errors introduced by use of the time-independent spectral point spread function within ozone profile retrievals. However, the introduction of the time-dependent spectral point spread function into the retrieval algorithms did not completely resolve the discrepancy. Instead, implementing the time-dependent spectral point spread function improved the correlation between OSIRIS and SAGE II ozone profiles during times of both eclipse and non-eclipse, significantly reducing the mean percent difference between the profiles at altitudes between 35–48 km altitude. The maximum improvement for both time periods occurred at 40 km altitude, where the percent difference was reduced by approximately 2%. The end result was that the coincident OSIRIS and SAGE II ozone profiles showed a percent difference of less than 2% from 18 to 48 km altitude during non-eclipse and a percent difference of 5-6% for these altitudes during times of eclipse.

A tangent point altitude shift caused by temperature gradients within the Odin satellite was found as a possible explanation for the remaining discrepancy observed during eclipse. Analysis revealed that during times of eclipse the line of sight of the OSIRIS instrument may have been shifted upward in altitude by between 0.3 and 0.4 km from what was intended, causing the entire retrieved ozone profile to be shifted downward in altitude by the same amount. Accounting for this altitude shift allowed the mean percent difference between SAGE II and OSIRIS eclipse profiles to be reduced to values below 3% from 18-48 km altitude.

It can be concluded from these results that the retrieval of OSIRIS ozone profiles is improved by implementing the time-dependent spectral point spread function and by accounting for any suspected altitude shifts. Before these enhancements were applied the mean percent difference between OSIRIS and SAGE II ozone profiles was as high as 3% during non-eclipse and 8% during eclipse for the 18-48 km altitude range. Performing the retrievals with these enhancements results in significantly improved ozone profiles, as the mean percent difference drops to less than 2% for both eclipse and non-eclipse profiles over the same altitude range.

Most importantly for this thesis, these results make it clear that implementing the time-dependent spectral point spread function into the retrieval algorithms improves the quality of the retrieved OSIRIS ozone profiles.

Chapter 6

Conclusions

6.1 Summary

The OSIRIS instrument currently orbiting Earth onboard the Odin satellite records measurements of limb-scattered light in the 280-810 nm wavelength range for use in the generation of high quality vertical number density profiles of atmospheric constituents such as ozone. These vertical profiles are retrieved from OSIRIS measurements using the SASKTRAN radiative transfer model and SaskMART iterative retrieval technique. The work of this thesis improves upon the quality of the retrieved constituent profiles by developing a time-dependent spectral point spread function, a tool that makes it possible for the algorithms used to model the atmosphere as observed by OSIRIS to accommodate for the time-varying dispersion of light seen in the final image produced by the OSIRIS spectrograph.

The Odin satellite follows a sun-synchronous orbit at an inclination of 97.8°, an orbit that causes Odin to slip into eclipse behind the Earth for a portion of its orbit during the months of the Northern Hemisphere summer. During these months the satellite experiences a drop in temperature which leads to alignment changes in the components of the OSIRIS spectrograph, altering the path of light through the spectrograph and distorting the dispersion of light in its final image. When modelling the OSIRIS-observed atmosphere this final dispersion of light is represented by the OSIRIS spectral point spread function, an array of Gaussian curve Full Width at Half Maximum (FWHM) values that describe, for every OSIRIS wavelength, the approximate dispersion pattern imaged onto the OSIRIS spectrograph CCD. Currently these atmospheric modelling algorithms employ a spectral point spread function that is time-independent, making the assumption that the dispersion of light at each wavelength is constant for every measurement of the OSIRIS mission. Consequen-

tially, compensation cannot be made for any changes in the dispersion pattern brought upon by temperature changes within the OSIRIS instrument, a situation that introduces systematic errors into constituent profile retrieval. These errors become non-negligible when retrieving profiles of stratospheric ozone, a process that makes use of the 310-350 nm wavelength range of the OSIRIS spectrum. The focus of this thesis is on eliminating these systematic errors and improving the profiles of retrieved ozone by developing a time-dependent spectral point spread function for OSIRIS wavelengths that range from 310 to 350 nm.

The first step in the method developed to calculate a time-dependent spectral point spread function is to remove the signatures of atmospheric interaction from the 310-350 nm wavelength range of an OSIRIS measurement. Atmospheric interaction in this wavelength range is dominated by two phenomena: Rayleigh scattering and absorption of light by ozone. Taking advantage of the fact that the efficiency of Rayleigh scattering is proportional to the inverse fourth power of wavelength, a normalized OSIRIS spectrum free of the signature of Rayleigh scattering can be produced by multiplying the OSIRIS spectrum by the fourth power of wavelength and normalizing the result. The signature of ozone absorption is then removed from the normalized Rayleigh-free spectrum by twice employing the Beer-Lambert law which describes the attenuation of radiation as it passes through an absorbing gas. The law is first used to calculate a first-order approximation of the amount of ozone present along the OSIRIS line of sight, which is then applied in the second use of the Beer-Lambert law to calculate a normalized top-of-atmosphere (TOA) OSIRIS measurement free from the signatures of atmospheric interaction in the 310-350 nm range.

With a TOA OSIRIS spectrum available, the next step is to compare it to a series of reference spectra. These reference spectra are created by convolving a high resolution TOA reference spectrum with a series of Gaussian curves that cover the range of Gaussian curves expected of the OSIRIS spectral point spread function. These convolved reference spectra are normalized and then compared against the TOA OSIRIS spectrum, a process completed by finding the point-by-point absolute difference between the OSIRIS spectrum and each of the convolved spectra for three wavelength regions centred on 313, 320, and 350 nm. For each of these three wavelength ranges, the sum of the absolute differences is computed for each of the convolved spectra, and the convolved spectrum whose sum is lowest is taken as the spectrum

that best fits the OSIRIS spectrum in that wavelength range. The Gaussian curve associated with the best fitting convolved spectrum is taken as the point spread function at the central wavelength of the range. In this way it is possible to determine point spread function values at 313, 320, and 350 nm for a single OSIRIS measurement. Linear interpolations are used to create a spectral point spread function from 310-350 nm unique to the OSIRIS measurement under consideration. This procedure was completed for measurements from all scans in the OSIRIS mission history, yielding a time-dependent spectral point spread function for wavelengths from 310 to 350 nm.

In order to reduce the noise in the calculated spectral point spread function as well as to shed light on the possible cause of its fluctuations over time, the spectral point spread function is modelled with an equation that uses measured satellite parameters as variables. The final form of the equation which successfully models and reduces the noise observed in the calculated point spread function is repeated here,

$$\mathrm{PSF}_x(t) = A_1 T(t) + A_2 \sin(\theta(t)) + A_3 \cos(\theta(t)) + A_4 \sin(2\theta(t)) + A_5 \cos(2\theta(t)) + A_6, \quad (4.15)$$

where t is some time in the OSIRIS mission, PSF_x is the point spread function at either the 313, 320, or 350 nm wavelength, T is the OSIRIS optics temperature and θ is the satellite track angle which defines the satellite's position in space. The coefficients A_{1-6} are calculated using multiple linear regression analysis, with three unique sets of coefficients (one set each for the 313, 320, and 350 nm wavelengths) being calculated for every day of the OSIRIS mission. The fact that this equation makes use of the OSIRIS optics temperature and satellite track angle as variables strongly suggests that changes in these two parameters are what lead to the observed fluctuations in the spectral point spread function.

After verification that Equation 4.15 produced a successful model of the spectral point spread function, it was implemented into the OSIRIS ozone retrieval algorithms. The impact of its addition was examined by comparing OSIRIS ozone profiles retrieved with both the time-dependent and time-independent spectral point spread functions against profiles retrieved from the SAGE II instrument. In both times of eclipse and non-eclipse the profiles retrieved with the time-dependent spectral point spread function showed consistently bet-

ter agreement with the profiles of SAGE II. After correcting for an altitude shift that most likely occurs due to the eclipse induced temperature drop, the OSIRIS profiles retrieved with the time-dependent spectral point spread function showed excellent agreement with the SAGE II profiles for the entire overlap period of the two missions. From these results it was confirmed that the time-dependent spectral point spread function was a successful addition to algorithms used to model the atmosphere as observed by OSIRIS and led to significant improvements in the retrieved OSIRIS ozone profiles.

6.2 Conclusions

The inspiration for this thesis work was a suspected fluctuation in the OSIRIS spectral point spread function over time, a fluctuation that was unaccounted for in the algorithms used to model the OSIRIS-observed atmosphere and capable of introducing systematic errors into the retrieval of ozone number density profiles. The improvements in OSIRIS ozone profiles due to the addition of a time-dependent point spread function not only confirms that such a fluctuation exists, but allows for several conclusions to be made regarding its behaviour.

It was initially speculated that the primary cause of the spectral point spread function fluctuations was temperature changes in the satellite causing thermal expansions and contractions which altered the alignment of the OSIRIS spectrograph optics. Analysis revealed that the calculated spectral point spread function and OSIRIS optics temperature were roughly anti-correlated, with orbitally averaged changes in spectral point spread function being mirrored by an orbitally averaged change in optics temperature. While it was not possible to find a relationship between optics temperature and spectral point spread function for single OSIRIS scans, this rough anti-correlation nonetheless confirms the suspicions that the temperature of the OSIRIS optics is the dominant driver behind changes to the spectral point spread function.

The primary variable that affects Odin's temperature, and therefore the OSIRIS spectral point spread function, is the sun. During times of non-eclipse the satellite is constantly bathed in sunlight and the temperature remains relatively stable throughout an orbit. However, during times of eclipse orbital variations in the spectral point spread function were

observed that were not mirrored by changes in optics temperature measurements, suggesting the presence of short term temperature gradients within the satellite. It was found that these orbital variations in spectral point spread function were related to the satellite's position over the Earth, making it possible to form equations that define the spectral point spread function of any single OSIRIS scan by its optics temperature and orbital position. These results lead to the conclusion that the temperature drop caused by Odin slipping into eclipse for a portion of the orbit and the subsequent warming that occurs when it re-emerges cause the suspected temperature gradients which lead to orbital fluctuations in the spectral point spread function.

Also of note is the impact of terrestrial radiation on the spectral point spread function. It was found that the spectral point spread function often varied over the course of many orbits throughout a day, a situation that cannot be attributed to solar radiation as the total amount of solar radiation Odin receives per orbit should be nearly constant over a day, even in times of eclipse. The Earth is the only other significant source of radiation available to Odin, and the amount of radiation it provides the satellite is dependent on two variables: the amount of atmosphere below Odin which is illuminated and the albedo of the illuminated ground. While both of these variables change slowly enough so as to not introduce significant temperature gradients into the satellite, they are necessary to complete the picture of the conditions that cause the spectral point spread function to vary over time: during times of non-eclipse the total flux of solar and terrestrial radiation varies slowly depending on the conditions below Odin, causing changes in the spectral point spread function to occur over many orbits. In times of eclipse these slow changes are supplemented by the continuous cycle of cooling and warming that introduces short term temperature gradients into the OSIRIS optics and causes rapid changes in the spectral point spread function.

Prior to the work of this thesis OSIRIS ozone retrievals showed good agreement with the retrieved profiles of the SAGE II instrument during times of non-eclipse, with the mean percent difference of profiles retrieved from the two instruments being less than 3% from 18 to 48 km altitude. However, during times of eclipse the mean percent difference increased to over 5% for the majority of altitudes in the same range, peaking at 40 km altitude with a mean percent difference of approximately 8%. Initial speculation was that the increase in

eclipse time mean percent difference was due to systematic errors in the atmosphere modelling algorithms caused by the use of a time-independent spectral point spread function that could not account for optical changes in the OSIRIS spectrograph. Analysis revealed the increase was likely due to two phenomena: The expected systematic errors stemming from the use of the time-independent spectral point spread function as well as an unexpected tangent altitude shifting caused by temperature changes within the Odin satellite.

Implementing the time-dependent spectral point spread function into the OSIRIS ozone retrievals had a positive impact on the eclipse time OSIRIS-SAGE II ozone profile mean percent difference in the 35-48 km altitude range, reducing the mean percent difference from 5-8% to 5-6% as shown in the left panel of Figure 6.1. The right panel of Figure 6.1 displays non-eclipse time data, where significant improvements were also observed. During non-eclipse times the mean percent difference in the 35-48 km altitude range falls from 1-3% to less than 2%. As SAGE II profiles are considered the gold standard of ozone retrievals, the reduction in the mean percent difference between OSIRIS and SAGE II profiles suggests a significant improvement in the retrieved OSIRIS ozone profiles. Despite the fact that the SAGE II mission ended in 2006, there is sufficient evidence in this analysis to conclude that the addition of the time-dependent spectral point spread function to the OSIRIS ozone retrieval algorithms improves the retrieved profiles by 1-2% in the 35-48 km range for all times of the OSIRIS mission.

Analysis revealed that the remaining eclipse time mean percent difference of 5-6% was likely caused by a tangent altitude shift in OSIRIS measurements. It is suspected that the instruments onboard Odin used to orient the OSIRIS line of sight suffer from temperature changes in a manner similar to those of the OSIRIS spectrograph optics, undergoing small changes in alignment that impact where the instrument is actually looking. It was found that shifting the altitude of eclipse time OSIRIS ozone profiles up by either 0.3 or 0.4 km produced profiles that compared much more favourably with the SAGE II profiles. Applying either of these altitude shifts produced a mean percent difference that was less than 2% from 18 to 48 km altitude (the 0.4 km altitude shifted mean percent difference is shown in the left panel of Figure 6.1), strongly suggesting the presence of an eclipse time altitude shift. A mean percent difference of less than 2% from 18 to 48 km is the same mean percent difference

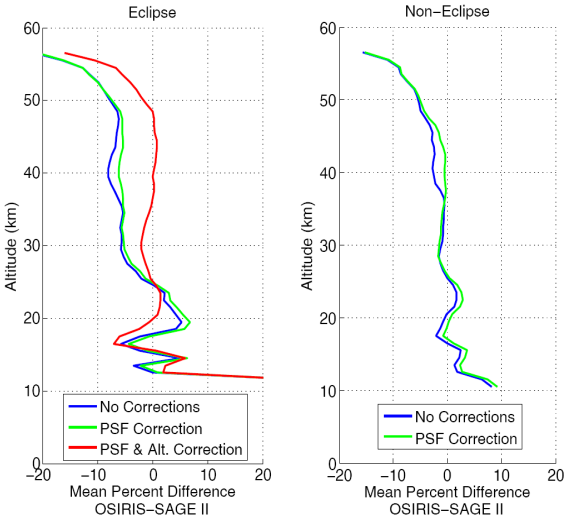

Figure 6.1: The initial and improved mean percent differences between OSIRIS and SAGE II ozone profiles during eclipse and non-eclipse. All profiles retrieved with the Serdyuchenko ozone cross section.

observed in times of non-eclipse, leading to the conclusion that accounting for this suspected altitude shift along with introducing the time-dependent spectral point spread function into the retrieval algorithms reduces the systematic errors of eclipse time OSIRIS ozone profile retrievals to negligible levels.

6.3 Future Work

The development of a time-dependent spectral point spread function for the 310-350 nm wavelength range of the OSIRIS spectrograph has cleared the way for multiple paths of future research. Perhaps the most obvious next step is to develop a time-dependent spectral point spread function for the remaining OSIRIS wavelengths. While it is likely that ozone profiles will always be the most affected by the time-dependent spectral point spread function due to the ozone cross section's extreme structure from 310 to 350 nm, other atmospheric constituents such as NO_2, BrO, and aerosols exhibit structure in their cross sections which may still be sensitive to convolution with different spectral point spread functions. In any case, having a time-dependent spectral point spread function for the entire OSIRIS spectrograph would improve knowledge of its day-to-day operation and could be used as a possible

diagnostic tool for issues that may occur as OSIRIS continues its mission. The development of such a spectral point spread function could be done in a manner similar to that described in this thesis; the methods for removing the atmospheric signature from the OSIRIS signal would naturally vary with wavelength, but all other steps of the procedure described in Section 3.2.1 could be implemented with only minor alterations.

The unexpected presence of what appears to be a temperature dependent altitude shift in OSIRIS measurements is also a matter that warrants further investigation. It must first be confirmed that such an altitude shift does indeed exist, a process that would require comparing the retrieved OSIRIS profiles of multiple atmospheric constituents against profiles retrieved from the coincident measurements of instruments such as SAGE II. If an altitude shift is confirmed then it would be of great benefit to relate the amount of shift to a measured OSIRIS parameter such as temperature or orbital position. The resulting time-dependent relationship could predict the amount of shift for any OSIRIS measurement, which when implemented into the algorithms used to model the atmosphere as seen by OSIRIS would hopefully eliminate the last systematic errors introduced by temperature changes within the OSIRIS instrument.

A final task that will certainly be completed in near future is an evaluation of the impact of using different ozone cross sections within the retrievals. As discussed in various sections throughout this thesis, an international group of atmospheric ozone experts has established an Absorption Cross Sections of Ozone (ACSO) Commission with the goal of standardizing the ozone cross section used by researchers in atmospheric ozone retrieval. The OSIRIS team is part of this Commission and as such must evaluate what impact implementing different ozone cross sections into the SASKTRAN model has on the retrieved ozone profiles.

Prior to this thesis, accurately evaluating the impact of the different ozone cross sections was found to be impossible due to the systematic errors introduced by the use of a time-independent spectral point spread function within the retrievals. The time-dependent spectral point spread function makes it possible to reduce these systematic errors to negligible levels, allowing the evaluation of ozone profiles retrieved with the various cross sections. A sample of this work was completed in Section 5.1.2 and provides a glimpse at what results to possibly expect. Ozone profiles were retrieved with the time-dependent spectral point

spread function and the SCIAMACHY (*Bogumil et al.*, 2003), DBM (*Brion et al.*, 1998), and Serdyuchenko ozone cross sections for a sample set of 196 OSIRIS scans. Compared against the SCIAMACHY cross section (which is used in the default OSIRIS ozone retrievals), the ozone profiles retrieved with the DBM and Serdyuchenko cross sections consistently showed an increase of 0.5-1.0% from 20-50 km altitude. A similar but much larger analysis must be undertaken where each of the ACSO ozone cross sections is implemented into the retrieval process and used to retrieve a large sample of ozone profiles from various latitudes, times of year, and scattered sunlight geometries. The profile differences introduced by the various cross sections will then be documented and presented in a full report to the ACSO Commission.

Bibliography

Adams, C., A. Bourassa, A. Bathgate, C. McLinden, N. Lloyd, C. Roth, E. Llewellyn, J. Zawodny, D. Flittner, G. Manney, W. Daffer, and D. Degenstein (2013), Characterization of Odin-OSIRIS ozone profiles with the SAGE II dataset, *Atmos. Meas. Tech. Discuss.*, *6*, 1033–1065, doi:10.5194/amtd-6-1033-2013.

Babcock, H. (1923), A study of the green auroral line by the interference method, *Astrophys. Jour.*, *57*, 209–221, doi:10.1086/142747.

Ballaré, C., M. Rousseaux, P. Searles, J. Zaller, C. Giordano, T. Robson, M. Caldwell, O. Sala, and A. Scopel (2001), Impacts of solar ultraviolet-B radiation on terrestial ecosystems of tierra del fuego (southern Argentina) An overview of recent progress, *J. Photochem. & Photobio.*, *62*(1), 67–77, doi:10.1016/S1011-1344(01)00152-X.

Bass, A., and R. Paur (1985), The ultraviolet cross-sections of Ozone: I. Measurements, in *Atmospheric ozone*, pp. 606–610, Springer, doi: 10.1007/978-94-009-5313-0-120.

Bates, D. (1984), Rayleigh scattering in air, *Planet. Space Sci.*, *32*(6), 785–790, doi: 10.1016/0032-0633(84)90102-8.

Berkner, L., and L. Marshall (1965), NAS symposium on the evolution of the earth's atmosphere: History of major atmospheric components, *Proceedings of the National Academy of Sciences of the United States of America*, *53*(6), 1215–1226.

Bernath, P., C. McElroy, M. Abrams, C. Boone, M. Butler, C. Camy-Peyret, C. Carleer, C. Clerbaux, P.-F. Coheur, R. Colin, P. DeCola, M. DeMazière, J. Drummond, D. Dufour, W. Evans, H. Fast, D. Fussen, K. Gibert, D. Jennings, E. Llewellyn, R. Lowe, E. Mahieu, J. McConnell, M. McHugh, S. McLeod, R. Michaud, C. Midwinter, R. Nasser, F. Nichitiu, C. Nowlan, C. Rinsland, Y. Rochon, N. Rowlands, K. Semeniuk, P. Simon, R. Skelton,

J. Sloan, M.-A. Soucy, K. Strong, P. Tremblay, D. Turnbull, K. Walker, I. Walkty, D. Wardle, V. Wehrle, R. Zander, and J. Zou (2005), Atmospheric Chemistry Experiment (ACE): Mission overview, *Geophys. Res. Lett.*, *32*(15), L15S01, doi:10.1029/2005GL022386.

Betts, A., and J. Ball (1997), Albedo over the boreal forest, *J. Geophys. Res.*, *102*(D24), 28,901–28,909, doi:10.1029/96JD03876.

Bhartia, P., R. McPeters, C. Mateer, L. Flynn, and C. Wellemeyer (1996), Algorithm for the estimation of vertical ozone profiles from the backscattered ultraviolet technique, *J. Geophys. Res.*, *101*(D13), 18,793–18,806, doi:10.1029/96JD01165.

Bogumil, K., J. Orphal, T. Homann, S. Voigt, P. Spietz, O. Fleischmann, A. Vogel, M. Hartmann, H. Kromminga, H. Bovensmann, J. Frerick, and J. Burrows (2003), Measurements of molecular absorption spectra with the SCIAMACHY pre-flight model: instrument characterization and reference data for atmospheric remote-sensing in the 230–2380 nm region, *J. Photochemistry and Biology*, *157*(2), 167–184, doi:10.1016/S1010-6030(03)00062-5.

Bourassa, A., D. Degenstein, R. Gattinger, and E. Llewellyn (2007), Stratospheric aerosol retrieval with OSIRIS limb scatter measurements, *J. Geophys. Res.*, *112*(D10), doi:10.1029/2006JD008079.

Bourassa, A., A. Robock, W. Randel, T. Deshler, L. Reiger, N. Lloyd, E. Llewellyn, and D. Degenstein (2012), Large volcanic aerosol load in the stratosphere linked to Asian monsoon transport, *Science*, *337*(6090), 78–81, doi:10.1126/science.1219371.

Bovensmann, H., J. Burrows, M. Buchwitz, J. Frerick, S. Noël, V. Rozanov, K. Chance, and A. Goede (1999), SCIAMACHY: Mission objectives and measurement modes, *J. Atmos. Sci.*, *56*(2), 127–150, doi:10.1175/1520-0469(1999)056¡0127:SMOAMM¿2.0.CO;2.

Brion, J., A. Chakir, D. Daumont, J. Malicet, and C. Parisse (1993), High-resolution laboratory absorption cross section of O_3. Temperature effect, *Chem. Phys. Lett.*, *213*(5), 610–612, doi:10.1016/0009-2614(93)89169-I.

Brion, J., A. Chakir, J. Charbonnier, D. Daumont, C. Parisse, and J. Malicet (1998), Absorption spectra measurements for the ozone molecule in the 350–830 nm region, *J. Atmos. Chem.*, *30*(2), 291–299, doi:10.1023/A:1006036924364.

Chahine, M. (1972), A general relaxation method for inverse solution of the full radiative transfer equation, *J. Atmos. Sci.*, *29*(4), 741–747, doi:10.1175/1520-0469(1972)029¡0741:AGRMFI¿2.0.CO;2.

Chandrasekhar, S. (1960), *Radiative Transfer*, Courier Dover Publications.

Chapman, S. (1930), *A theory of upper-atmospheric ozone*, Edward Stanford.

Collins, D., W. Blättner, M. Wells, and H. Horak (1972), Backward Monte Carlo calculations of the polarization characteristics of the radiation emerging from spherical-shell atmospheres, *App. Optics*, *11*(11), 2684–2696, doi:10.1364/AO.11.002684.

Cunnold, D., F. Alyea, N. Phillips, and R. Prinn (1975), A three-dimensional dynamical-chemical model of atmospheric ozone, *J. Atmos. Sci.*, *32*, 170–194, doi:10.1175/1520-0469(1975)032¡0170:ATDDCM¿2.0.CO;2.

Daumont, D., J. Brion, J. Charbonnier, and J. Malicet (1992), Ozone UV spectroscopy I: Absorption cross-sections at room temperature, *J. Atmos. Chem.*, *15*(2), 145–155, doi:10.1007/BF00053756.

Degenstein, D., E. Llewellyn, and N. Lloyd (2003), Volume emission rate tomography from a satellite platform, *Appl. Opt.*, *42*(8), 1441–1450, doi:10.1364/AO.42.001441.

Degenstein, D., E. Llewellyn, and N. Lloyd (2004), Tomographic retrieval of the oxygen infrared atmospheric band with the OSIRIS imager, *Can. J. Phys.*, *82*(7), 501–515, doi:10.1139/p04-024.

Degenstein, D., A. Bourassa, C. Roth, and E. Llewellyn (2009), Limb scatter ozone retrieval from 10 to 60 km using a multiplicative algebraic reconstruction technique, *Atmos. Chem. Phys.*, *9*(17), 6521–6529, doi:10.5194/acp-9-6521-2009.

Dessler, A. (2000), *The chemistry and physics of stratospheric ozone*, *International Geophysics Series*, vol. 74, Academic Press.

Flittner, D., P. Bhartia, and B. Herman (2000), O_3 profiles retrieved from limb scatter measurements: Theory, *Geophys. Res. Lett.*, *27*(17), 2601–2604, doi:10.1029/1999GL011343.

Heath, D., A. Krueger, H. Roeder, and B. Henderson (1975), The Solar Backscatter Ultraviolet and Total Ozone Mapping Spectrometer (SBUV/TOMS) for Nimbus G, *Opt. Eng.*, *14*(4), 144,323–144,323, doi:10.1117/12.7971839.

Kasap, S. (2001), *Optoelectronics and Photonics*, Prentice Hall.

Kurucz, R., I. Furenlid, J. Brault, and L. Testerman (1984), Solar Flux Atlas from 296 to 1300 nm, *National Solar Observatory Atlas, Sunspot, New Mexico: National Solar Observatory, 1984*, *1*.

Llewellyn, E. J., N. D. Lloyd, D. A. Degenstein, R. L. Gattinger, S. V. Petelina, A. E. Bourassa, J. T. Wiensz, E. V. Ivanov, I. C. McDade, B. H. Solheim, J. C. McConnell, C. S. Haley, C. von Savigny, C. E. Sioris, C. A. McLinden, E. Griffioen, J. Kaminski, W. F. Evans, E. Puckrin, K. Strong, V. Wehrle, R. H. Hum, D. J. W. Kendall, J. Matsushita, D. P. Murtagh, S. Brohede, J. Stegman, G. Witt, G. Barnes, W. F. Payne, L. Piché, K. Smith, G. Warshaw, D.-L. Deslauniers, P. Marchand, E. H. Richardson, R. A. King, I. Wevers, W. McCreath, E. Kyrölä, L. Oikarinen, G. W. Leppelmeier, H. Auvinen, G. Mégie, A. Hauchecorne, F. Lefèvre, J. de La Nöe, P. Ricaud, U. Frisk, F. Sjoberg, F. von Schéele, and L. Nordh (2004), The OSIRIS instrument on the Odin spacecraft, *Can. J. Phys.*, *82*(6), 411–422, doi:10.1139/p04-005.

Malicet, J., D. Daumont, J. Charbonnier, C. Parisse, A. Chakir, and J. Brion (1995), Ozone UV spectroscopy. II. Absorption cross-sections and temperature dependence, *J. Atmos. Chem.*, *21*(3), 263–273, doi:10.1007/BF00696758.

McCormick, M. (1987), SAGE II: An overview, *Adv. Space Res.*, *7*(3), 219–226, doi:10.1016/0273-1177(87)90151-7.

McCormick, M., P. Hamill, T. Pepin, W. Chu, T. Swissler, and L. McMaster (1979), Satellite studies of the stratospheric aerosol, *Bull. Am. Meteorol. Soc.*, *60*, 1038–1047, doi: 10.1175/1520-0477(1979)060¡1038:SSOTSA¿2.0.CO;2.

Murtagh, D., U. Frisk, F. Merino, M. Ridal, A. Jonsson, J. Stegman, G. Witt, P. Eriksson, C. Jiménez, G. Megie, J. de La Nöe, P. Ricaud, P. Baron, J. R. Pardo, A. Hauchcorne, E. J. Llewellyn, D. A. Degenstein, R. L. Gattinger, N. D. Lloyd, W. F. J. Evans, I. C. McDade, C. S. Haley, C. Sioris, C. von Savigny, B. H. Solheim, J. C. McConnell, K. Strong, E. H. Richardson, G. W. Leppelmeier, E. Kyrölä, H. Auvinen, and L. Oikarinen (2002), Review: An overview of the Odin atmospheric mission, *Can. J. Phys.*, *80*(4), 309–319.

Orphal, J. (2003), A critical review of the absorption cross-sections of O_3 and NO_2 in the ultraviolet and visible, *Journ. Photochem. and Photobio.*, *157*(2), 185–209, doi: 10.1016/S1010-6030(03)00061-3.

Roth, C., D. Degenstein, A. Bourassa, and E. Llewellyn (2007), The retrieval of vertical profiles of the ozone number density using chappuis band absorption information and a multiplicative algebraic reconstruction technique, *Can. J. Phys.*, *85*(11), 1225–1243, doi: 10.1139/p07-130.

Thomason, L., and G. Taha (2003), SAGE III aerosol extinction measurements: Initial results, *Geophys. Res. Lett.*, *30*(12), 1631, doi:10.1029/2003GL017317.

Thuillier, G., M. Hersé, D. Labs, T. Foujols, W. Peetermans, D. Gillotay, P. Simon, and H. Mandel (2003), The solar spectral irradiance from 200 to 2400 nm as measured by the SOLSPEC spectrometer from the ATLAS and EURECA missions, *Solar Phys.*, *214*(1), doi:10.1023/A:1024048429145.

Warshaw, G., D.-L. Deslauniers, and D. Degenstein (1996), Optical design and performance of the Odin UV/visible spectrograph and infrared imager instrument, in *10th Annual AIAA/USU Small Satellite Conference, Logan, Utah.*

Whitten, R., and S. Prasad (Eds.) (1985), *Ozone in the free atmosphere*, New York: Van Nostrand Reinhold.